UNIVERSITÀ DI TRENTO
Department of Industrial Engineering
XXXIV cycle

Doctoral School in Materials, Mechatronics and System Engineering

3D printing of bone scaffolds using powders derived from biogenic sources

Francesca Cestari

January 2023

3D printing of bone scaffolds using powders derived from biogenic sources

Francesca Cestari

Email: francesca.cestari@unitn.it

Approved by:

Prof. Vincenzo M. Sglavo, Advisor
Dept. of Industrial Engineering
University of Trento, Italy

Ph.D. Commission:

Prof. Gian Domenico Sorarù
Dept. of Industrial Engineering
University of Trento, Italy

Prof. Simone Sprio
ISTEC-CNR
Faenza

Prof. Francesco Baino
Dept. of Applied Science and Technology
Politecnico di Torino

University of Trento

Department of Industrial Engineering

January 2023

University of Trento - Department of Industrial Engineering

Doctoral Thesis

Francesca Cestari – January 2023

Published in Trento (Italy)

by University of Trento ISBN: - - - - - - - - -

Abstract

This doctoral work was developed in the frame of bone tissue engineering, dealing with the fabrication of scaffolds for the regeneration of bones. At this purpose, calcium phosphates derived from natural sources are very interesting because they are more similar to the bone mineral and possess better bioactivity. Indeed, the bone mineral is different from synthetic hydroxyapatite as it is non-stoichiometric, nanosized, it presents a high degree of disorder and contains many additional ions and impurities such as CO_3^{2-}, Mg^{2+}, Sr^{2+}, Na^{+}, etc. These characteristics can be easily obtained by synthesizing hydroxyapatite from natural sources, such as corals, starfishes, seashells, animal bones, bird eggshells etc.

The natural sources used in the present work are three types of biogenic calcium carbonate, i.e. calcium carbonate that is produced by living organisms in the form of aragonite or calcite. Among the different sources, three biogenic calcium carbonates were chosen: cuttlefish (*Sepia Officinalis*) bones, mussel (*Mytilus Galloprovincialis*) shells and chicken eggshells. Besides their abundance and availability, they were selected because of their different composition: aragonite in cuttlebones, calcite in eggshells and a mixture of aragonite and calcite in mussel shells.

After the first chapter, which is a theoretical introduction, this thesis is divided into other five chapters. Chapter 2 contains a careful characterization of the three biogenic raw materials while Chapter 3 deals with the synthesis of hydroxyapatite starting from these natural sources. The process developed here takes place entirely at nearly room temperature, which allows the organic part of the biological materials to be preserved. This synthesis process is basically a wet mechanosynthesis followed by a mild heat treatment (up to 150°C). The study focuses on the influence of several process parameters on the synthesis efficiency: temperature, milling time, pH and raw material. The temperature used to dry the slurry after the wet ball-milling was found to be the most important parameter, the higher the temperature the faster the conversion of $CaCO_3$ into hydroxyapatite. Moreover, aragonite

was found to transform more easily into hydroxyapatite with respect to calcite, and also to follow a different reaction path.

The synthesis process described in Chapter 3 allowed to produce different bio-derived powders that were found to be non-stoichiometric, nanosized, carbonated hydroxyapatites, containing also additional ions, especially Mg^{2+} in the eggshell-derived material and Sr^{2+} in the cuttlebone-derived one. These powders were then used as a starting point for the studies presented in the next three chapters.

Chapter 4 shows a very preliminary evaluation of the interaction with human cells *in vitro*. First, the as-synthesized powders were consolidated by uniaxial pressing and sintering at temperatures between 900°C and 1100°C and their crystallographic composition was analyzed. Then, after having established the non-cytotoxicity of the sintered pellets, osteoblasts from human osteosarcoma cell line were seeded on the pellets and their behavior after 1, 3 and 5 days of culture was observed by confocal microscopy. In general, all materials promoted good cell adhesion and proliferation, especially the eggshell-derived one.

At this point, the bio-derived materials were found to induce a good cellular response but, in order to foster the regeneration of bones, a scaffold must also contain a large amount of interconnected porosity. Among the numerous methods to fabricate porous structures, additive manufacturing is surely very attractive due many advantages, such as the possibility of customizing the shape based on tomography images from the patients, the fact that no mold is needed and the freedom of fully designing the porosity. Indeed, not only the size and the amount of porosity are important, but also the shape of the pores and their position and orientation have a deep effect on the interaction with the cells. Therefore, Chapter 5 and Chapter 6 deal with the fabrication of scaffolds by 3D printing, following two different approaches.

In the study presented in Chapter 5, the powders synthesized from cuttlebones, mussel shells and eggshells were used in combination with a thermoplastic polymer (PCL, polycaprolactone) to obtain bioactive composites. Composite materials made of 85 wt% PCL and 15 wt% bio-derived hydroxyapatite were used to fabricate porous scaffolds by extrusion 3D printing. The biological *in vitro* tests showed that the composite scaffolds possess better bioactivity than the pure PCL ones, especially those containing mussel shell- and cuttlebone-derived

powders, which promoted the best cell adhesion, proliferation and metabolic activity of human osteosarcoma cells after 7 days of culture. In addition, the elastic compressive modulus, which was found to be between 177-316 MPa, thus in the range of that of trabecular bone, was found to increase of about ~50% with the addition of the bio-derived nanopowders.

Finally, in Chapter 6, the cuttlebone-derived powder was used to fabricate porous bioceramic scaffolds by binder jetting 3D printing. Due to serious technical issues related to the printing of a nanosized powder, 10 wt% of bio-derived powder was mixed with a glass-ceramic powder with bigger particle size. Moreover, the organic part of the cuttlebone had to be previously eliminated by a heat treatment at 800°C. Thanks to the great freedom of design that is allowed by the binder jetting process, scaffolds with two different pore geometries were fabricated: with pores of uniform size and with a size-gradient. Indeed, natural bone possesses a gradient in porosity from the core to the surface, from porous trabecular bone to dense cortical bone. The sintered scaffolds showed a total porosity of ~60% for the pure glass-ceramic and ~70% for the glass-ceramic with 10 wt% of cuttlebone-derived nanoparticles, which most probably slowed down the densification by limiting the contact between the glassy particles. All the bioceramic scaffolds promoted good adhesion and proliferation of human bone marrow-derived mesenchymal stem cells *in vitro*, without any significant difference between the different samples. However, the scaffolds with the cuttlebone-derived powder and with gradient porosity showed the greatest decrease of metabolic activity after 10 days of culture, which could be accounted as a sign of differentiation of stem cells.

Contents

List of figures

List of tables

List of abbreviations

Abbreviation	Meaning
ECM	Extra cellular matrix
BTE	Bone tissue engineering
HA	Hydroxyapatite
β-TCP	β-tricalcium phosphate
PCL	Polycaprolactone
CaPs	Calcium phosphates
CDHA	Calcium deficient hydroxyapatite
BCP	Biphasic calcium phosphate
ACP	Amorphous calcium phosphate
AM	Additive manufacturing
CAD	Computer aided design
FDM	Fused deposition modelling
SLA	Stereolithography
SLS	Selective laser sintering
SLM	Selective laser melting
DIW	Direct ink writing
P-3DP	Powder 3D printing
PSD	Powder size distribution
SSA	Specific surface area
ACC	Amorphous calcium carbonate
CB	Cuttlefish bone

MS	Mussel shell
ES	Eggshell
sHA	Synthetic hydroxyapatite
CB-HA	Hydroxyapatite derived from cuttlebones
ES-HA	Hydroxyapatite derived from eggshells
MS-HA	Hydroxyapatite derived from mussel shells
LDH	Lactate dehydrogenase
PBS	Phosphate-buffered saline

Chapter 1

Introduction

1.1 Regeneration and tissue engineering

Regeneration is defined as the reconstruction of a body part after its loss or damage. For example, our blood regenerates if we lose some of it for a wound and, in our everyday life, hair and skin keep renewing themselves. Some animals show an exceptional regeneration ability being able to reconstruct large parts of their body after their removal. For example, newts can regrow an entire limb, including muscle and bone, through the formation of a proliferative tissue called *blastema,* while invertebrates of the *Planariidae* family and *Hydra* can even rebuild the entire body starting from small body pieces. Other extraordinary examples of regeneration in the animal world are zebra fishes and axolotls [1].

Figure 1-1. Left: illustration of an axolotl, an aquatic Mexican salamander that can regenerate its limbs. Right: Prometheus Bound, painted by Peter Paul Rubens, completed by 1618, currently in the collection of the Philadelphia Museum of Art.

The phenomenon of regeneration is present also in myth. When Zeus revoked the men's privilege of using fire, Prometheus stole the fire from

the Olympus and gave it back to men. His punishment consisted in being chained to a high rock, where an eagle came every night to eat his liver, which regenerated every day, so that the punishment would continue forever [2]. It is not clear whether ancient Greeks had some medical knowledge about tissue regeneration or not, but, as a matter of fact, the human liver exhibits an almost unlimited capacity to regenerate [3].

But how is regeneration possible? In order to regrow new tissues a cellular source is needed. This source is generally either stem cells or progenitor cells, or, alternatively, it requires dedifferentiation or transdifferentiation of cells. Moreover, regeneration seems to be connected to genetic programs related to the embryonic development, which might explain why fetuses show superior regeneration abilities and, in general, why the regeneration capacity decreases with ageing [1].

Unlike axolotls, humans can regrow a lost body part only to a limited extent. When the missing part is too big, *i.e.* when the defect size is greater than a certain critical size, the body cannot restore the original tissue, which is replaced with scar tissue, loosing functionality. For human bone the critical defect size is typically around 2 cm, depending on the anatomical site [4]. That's why, in many cases, we need to help the tissue to regrow.

One of the first examples of aided bone regeneration can again be found in the Greek myth. When the young Achilles lost an ankle bone due to a burn, his father Peleus, or, in other legends, the centaur Chiron, who was an expert in medicine, exhumed the skeleton of the agile giant Damysus, took a piece of the giant's ankle bone and put it in the child's foot. With the additional help of some drugs, the giant's bone was perfectly incorporated and Achilles acquired his legendary fleetness, becoming the hero we all know [5]. Since giants are not humans, this can be taken as an example of xenograft, which is the implantation of a tissue coming from a donor belonging to another species. Besides myth, bone grafting was known since ancient times and, for example in Armenia, around 2000 BC, an ancient surgeon inserted an animal bone graft in a 7 mm-skull defect [6].

Apart from xenografts, alternative options are allografts, where the tissue donor is another human, and autografts, when the donor is the patient himself. Autografts are currently the "gold standard", but collecting the bone material from the donor site can be painful and can

cause injuries. On the other hand, allografts and xenografts carry the risks of being rejected and transmitting diseases, especially for the latter, since they come from animals [7]. Moreover, the supply of bone material to be implanted is often limited or insufficient.

Tissue engineering was developed to overcome these difficulties and it involves the use of one or more of the following elements:

- **Scaffolds**, that are artificial three-dimensional structures used to sustain tissue ingrowth [8];
- **Cells**, which serve as cellular source for regrowth; examples are mesenchymal stem cells, bone marrow stromal cells, osteoblasts and embryonic or adult stem cells [9];
- **Growth factors**, which are polypeptides synthesized by the bone tissue in very low concentrations that act as local regulators, stimulating or inhibiting the growth [10].

In this frame, the present work deals with bone scaffolds derived from natural sources, therefore cells and growth factors will not be further discussed.

1.2 The bone structure

Natural bone is a highly complex composite material organized in a porous hierarchical structure that performs many important functions. It provides structural support and protection to organs, it acts as a mineral reservoir to maintain mineral homeostasis and it is a source of mesenchymal and hematopoietic stem cells [11]. Bone cells and blood vessels are embedded in a matrix of organic, mainly collagen I, and inorganic, the bone mineral. The bone tissue is therefore a polymer-ceramic composite material, consisting of about 33-43 vol% minerals, 32-44 vol% organic and 15-25 vol% water [12].

The hierarchical structure of bone is depicted in Figure 1-2. Two types of bone can be distinguished based on their macrostructure: cortical (or compact) bone and cancellous (or spongy or trabecular) bone. The porosity of cancellous bone is in the range of 75-95% and its density is around 0.2-0.8 g/cm^3 [12]. The struts of cancellous bone are called trabeculae, they are typically 50-300 μm thick and their orientation depends on the load directions [13]. It usually constitutes the inner part of bones, while the outer shell is made of cortical bone, with porosity 5-

10% and density about 2 g/cm^3 [12]. The mechanical properties of trabecular bone are highly dependent on its porosity, the compressive modulus being in the range 50-660 MPa [9,14,15] and the yield stress between 1-10 MPa [15]. Cortical bone, instead, has a compressive modulus of 7-30 GPa [9,12] and a yield stress of 50-230 MPa [16].

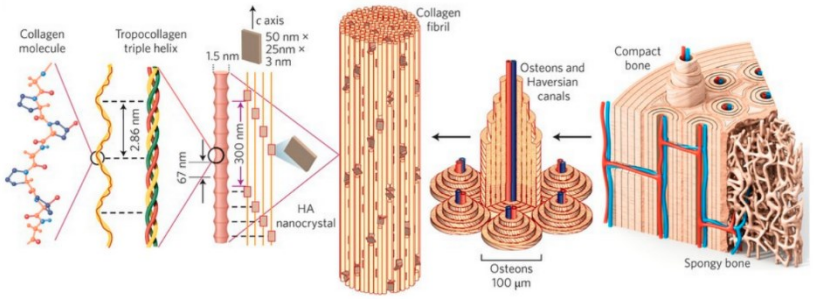

Figure 1-2. The hierarchical structure of bone. Reproduced from [13].

At the microstructural level, cortical bone and trabeculae are made of sheets of mineralized collagen fibers aligned in the same direction. These sheets, called lamellae, are 3–7 µm thick and are usually stacked on each other. In the trabeculae of cancellous bone, lamellae are aligned almost in the same direction, in the range ± 30° [17]. In cortical bone, instead, lamellae wrap up in concentric layers around a central canal forming an osteon, that is made of 3–8 lamellae stacked with orientation ± 45° [9,18]. The osteon, with a diameter of approx. 200 µm, surrounds the Haversian canal, which runs parallel to the long axis of the bone and contains blood vessels and nerves. There are also canals transversely aligned to the osteons, called Volkmann's canals, which connect the main vascular channels to each other. The bone cells, osteocytes, are confined in cavities called lacunae and communicate with each other through small channels called canaliculi [12].

Lamellae are composed of mineralized collagen fibrils. A fibril is about 100 µm thick and it is an assemble of tropocollagen type I molecules, which are 300 nm long and 1.5 nm thick and are composed of three collagen molecules arranged in a triple helix. Apatite crystals of about 50 x 25 x 3 nm^3 occur in the longitudinal spaces between tropocollagen molecules. Moreover, since adjacent molecules are longitudinally shifted of 67 nm, apatite crystals are also forming are 67 nm pattern, as shown

in Figure 1-2 [13,18,19]. The mineral fraction and the orientation of the lamellae are, of course, important factors that influence the mechanical properties of bone, such as its modulus, its toughness and its anisotropy.

In conclusion, the hierarchical structure of bone is highly complex, moving from the nanostructure, to the microstructure up to the macrostructure. Moreover, living bone is a dynamic material that undergoes continuous remodeling to meet the loading requirement, repair micro-damages and maintain mineral homeostasis. Hormones, growth factors and mechanical stresses lead to bone resorption by osteoclasts and subsequent new bone formation by osteoblasts [20]. In this way bone adapts to its needs, for example changing the thickness and the orientation of trabeculae or the mineralization degree.

1.3 Bone scaffolds

Scaffolds are three-dimensional constructs meant to temporarily substitute the tissue ECM (extra cellular matrix), host tissue cells and promote cells attachment, proliferation and tissue ingrowth. In order to do so, an ideal scaffold for bone regeneration should meet many different requirements in terms of architecture, mechanical properties, chemical properties, biological interaction, etc.. The desired features of an ideal scaffold for bone tissue engineering (BTE) are the following:

- **Porosity**. Interconnected pores with dimensions in the range 200-500 μm are necessary to allow the penetration of cells and give space for vascularization [8]. Micropores with diameters lower than 10 μm are also desired, since they were found to improve the cell-scaffold interaction [21].
- **Biocompatibility**. The scaffold should be not toxic and do not induce immune reactions.
- **Bioactivity**. The material should be able to interact with and bind with the host tissue [21]. Bioactive materials can be **osteoinductive**, that is being able to stimulate the differentiation of mesenchymal stem cells into osteoblasts, or **osteoconductive**, meaning that they enable the deposition of mineralized tissue on their surface. **Osseointegration**, which is critical in load bearing applications, means that there is a stable bond between the implant and the surrounding tissue [4].

- **Bioresorbability/biodegradability**. In order to be replaced by natural bone, the scaffold should eventually be resorbed by the body, with a degradation/resorption rate that matches the growth rate of the new tissue. For load bearing applications, the scaffold should maintain its physical properties for at least 6 months, then start losing them and be completely metabolized within 12-18 months [22].
- **Mechanical properties** must be high enough for bearing the specific loads and preferably match as close as possible those of the hosting tissue in order to avoid the phenomenon of stress shielding. In fact, if the mechanical properties of the implant largely exceed those of the hosting bone, the implant will bear the majority of the loads and the bone will start remodeling reducing its density [4].

A wide range of materials has been considered for bone tissue engineering purposes, including metals, natural and synthetic polymers, bioceramics, bioglasses and composites. An overview of the main materials used to fabricate scaffolds for bone regeneration is given in Table 1-1.

To summarize, metals have high mechanical properties (stiffness, strength, toughness) and excellent biocompatibility, but they are usually heavy and non-biodegradable and they can provoke stress shielding. Bioceramics show the best bioactivity, being osteoconductive, osteoinductive and favoring osseointegration, but they are hard and brittle, which is an issue in load bearing applications. Natural and synthetic polymers have the advantages of being processed easily and possessing a wide range of compositions and properties. However, they generally have low mechanical properties and poor bioactivity, being osteoconductive but not osteoinductive [4,21,23].

Composite materials are widely used to overcome these limitations. In particular, polymers are often used in combination with bioceramic fillers in order to enhance the bioactivity of the polymer, improve its mechanical properties and avoid the brittleness typical of ceramics [24–26]. For example, hydroxyapatite (HA) and β-tricalcium phosphate (β-TCP) have been used as fillers to improve the bioactivity of PLA (polylactic acid) [27–29] and PCL (polycaprolactone) [24,25,30–32].

Table 1-1. Overview of materials used in bone tissue engineering. Adapted from [4,21,23].

Material type	**Examples**	**Main advantages**	**Main disadvantages**
Non-biodegradable metals	Ti alloys Co-Cr Zirconium Stainless steel	High mechanical properties High biocompatibility	Risk of stress shielding Non-biodegradable
Biodegradable metals	Mg alloys	High mechanical properties High biocompatibility	Risk of stress shielding
Bioceramics	Hydroxyapatite (HA) β-tricalcium phosphate (β-TCP)	High bioactivity	Brittleness
Bioglasses	45S5 Bioglass®	High bioactivity	Brittleness Rapid degradation rate
Synthetic polymers	Poly(ε- caprolactone) (PCL) Poly(l- lactic acid) (PLLA) Poly(glycolic acid) (PGA) Poly(ethylene glycol) (PEG) Poly(lactic- co-glycolic acid) (PLGA)	Ease of modification Wide range of compositions and properties	Some produce undesirable degradation products Low mechanical properties Limited bioactivity

Material type	Examples	Main advantages	Main disadvantages
Natural polymers	Collagen Alginate Silk Chitosan Hyaluronic acid	Some contain cell-adhesion sites Biodegradability	Low mechanical properties Batch-to-batch variability May contain pathological impurities

1.4 Bioceramics: calcium orthophosphates

From different combinations of CaO and P_2O_5 a great variety of calcium phosphates can be obtained, classified depending on the phosphate anion: ortho- (PO_4^{3-}), meta (PO_3^-) and pyro- ($P_2O_7^{4-}$) [33].

Calcium orthophosphates (CaPs) are of great scientific interest due to their abundance in nature and their presence in living organisms. They consist of calcium (oxidation state +2), phosphorus (oxidation state +5) and oxygen (reduction state -2). They can also include hydrogen, as acidic anions like HPO_4^{2-} or $H_2PO_4^-$, and they can incorporate water molecules [33]. Table 1-2 lists different calcium orthophosphates and their major properties.

The molar ratio between calcium and phosphorus (Ca/P ratio) is a useful parameter to describe the stoichiometry of calcium orthophosphates and it is the most common parameter in the field. Another possibility is to use the following general formula:

$$(CaO)_x \cdot (P_2O_5)_y \cdot (H_2O)_z. \quad (1)$$

These approaches can both be used to draw pseudo-binary equilibrium phase diagrams, which can be employed to predict which phase would form after a synthesis route. Phase diagrams usually refer to a certain partial pressure of water present, as in Figure 1-3 and Figure 1-4, which show a part of the equilibrium phase diagram of the system CaO-P_2O_5 with 0 Hg and 500 Hg of water partial pressure, respectively.

Table 1-2. Calcium orthophosphates and their major properties [33–35]. "n.p." indicates that the compound cannot be precipitated from aqueous solutions.

Compound	Formula	Ca/P molar ratio	Solubility at 25°C (g/l)	pH stability range	Density (g/cm^3)
Monocalcium phosphate monohydrate (MCPM)	$Ca(H_2PO_4)_2*H_2O$	0.5	~18	0.0-2.0	2.23
Monocalcium phophate anhydrous (MCPA)	$Ca(H_2PO_4)_2$	0.5	~18	stable above 100°C	2.58
Dicalcium phosphate dihydrate (DCPD) or brushite	$CaHPO_4 \cdot 2H_2O$	1	~0.088	2.0-6.0	2.32
Dicalcium phosphate anhydrous (DCPA) or monetite	$CaHPO_4$	1	~0.048	stable above 100°C	2.89
Octacalcium phosphate (OCP)	$Ca_8(HPO_4)_2(PO_4)_4 \cdot 5H_2O$	1.33	~0.0081	5.5-7.0	2.61
α-Tricalcium phosphate (α-TCP)	α-$Ca_3(PO_4)_2$	1.5	~0.0025	n.p.	2.86
β-Tricalcium phosphate (β-TCP)	β -$Ca_3(PO_4)_2$	1.5	~0.0005	n.p.	3.07
Calcium deficient hydroxyapatite (CDHA)	$Ca_{10-x}(HPO_4)_x(PO_4)_{6-x}(OH)_{2-x}$ $(0 < x < 1)$	1.5-1.67	~0.0094	6.5-9.5	-

Compound	Formula	Ca/P molar ratio	Solubility at 25°C (g/l)	pH stability range	Density (g/cm³)
Hydroxyapatite (HA)	$Ca_{10}(PO_4)_6(OH)_2$	1.67	~0.0003	9.5-12	3.16
Fluorapatite (FA)	$Ca_{10}(PO_4)_6F_2$	1.67	~0.0002	7-12	3.20
Oxyapatite (OA)	$Ca_{10}(PO_4)_6O$	1.67	~0.087	n.p.	~3.2
Tetracalcium phosphate (TTCP)	$Ca_4(PO_4)_2O$	2.0	~0.0007	n.p.	3.05

The phase diagram without the presence of water (Figure 1-3) shows the stoichiometric compounds TTCP and TCP at Ca/P ratios equal to 2.0 and 1.5, respectively. TTCP ($Ca_4(PO_4)_2O$), tetracalcium phosphate, is also known as the mineral hilgenstockite and it is not stable in aqueous environments as it slowly hydrolyzes to HA and CaOH. It is not present in biological calcifications and it is used in medicine as a component in self-setting bone cements [33].

TCP ($Ca_3(PO_4)_2$), tricalcium phosphate, has three polymorphs. β-TCP has a rhombohedral structure and it is stable up to 1125°C, monoclinic α-TCP is stable between 1125°C and 1470°C and α'-TCP has a trigonal structure and it is stable at higher temperatures. When quenched, α'-TCP always transforms into α-TCP, while α-TCP can be maintained at room temperature as a metastable phase [36]. α-TCP is five times more soluble than β-TCP (see Table 1-2), which makes the resorption rate of α-TCP too high to be used as a scaffold material, so it is used mainly as a component of bone cements [33].

β-TCP is the stable phase at room temperature and, in its Mg-containing form whitlockite (β-$(Ca,Mg)_3(PO_4)_2$, it is present in the human body in some pathological calcifications like urinary stones [34]. Its crystal structure is rhombohedral, space group R3c, with a = 10.432 Å and c = 37.40 Å [37]. It is used in bone cements and it is employed as bone substitute, especially in combination with HA to form BCP (biphasic calcium phosphate) [34].

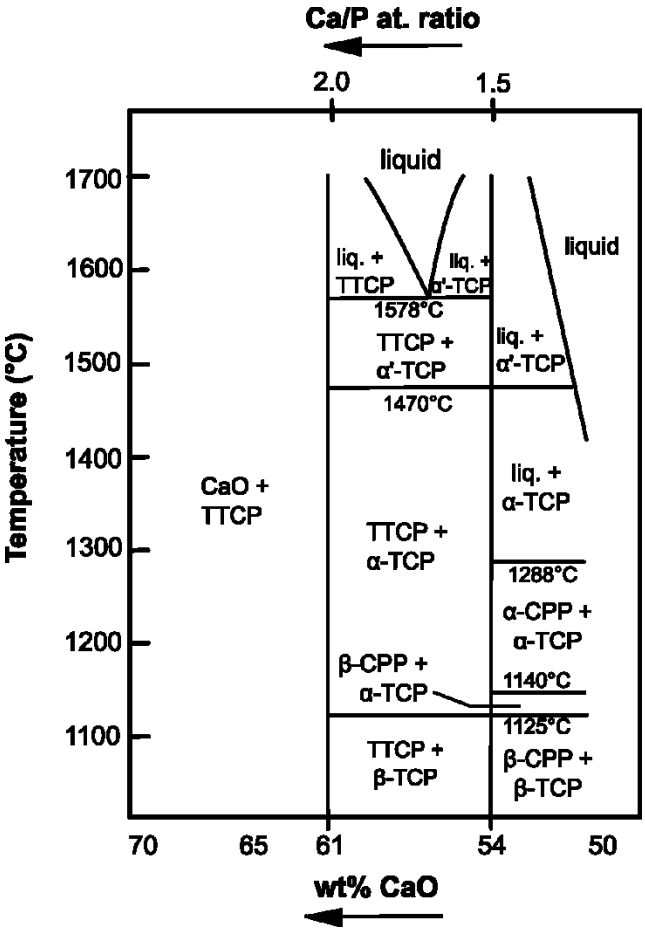

Figure 1-3 Equilibrium phase diagram of the system CaO-P_2O_5 with 0 Hg of water partial pressure. Redrawn from [38,39].

In the absence of water and at low concentrations of CaO, the phase diagram shows also the presence of calcium pyrophosphate, CPP (formula $Ca_2P_2O_7$). CPP has also two polymorphs, as it undergoes a phase transformation between the tetragonal β-CPP and the monoclinic α-CPP at about 1140°C (Figure 1-3). CPP has a Ca/P ratio equal to 1.0 and it is attracting attention because its biological response is similar to that of HA [40]. In its hydrated form, $Ca_2P_2O_7 \cdot 2H_2O$, CPP is present in the human

body in synovium in joints, as a result of an inflammatory arthritis called gout [41].

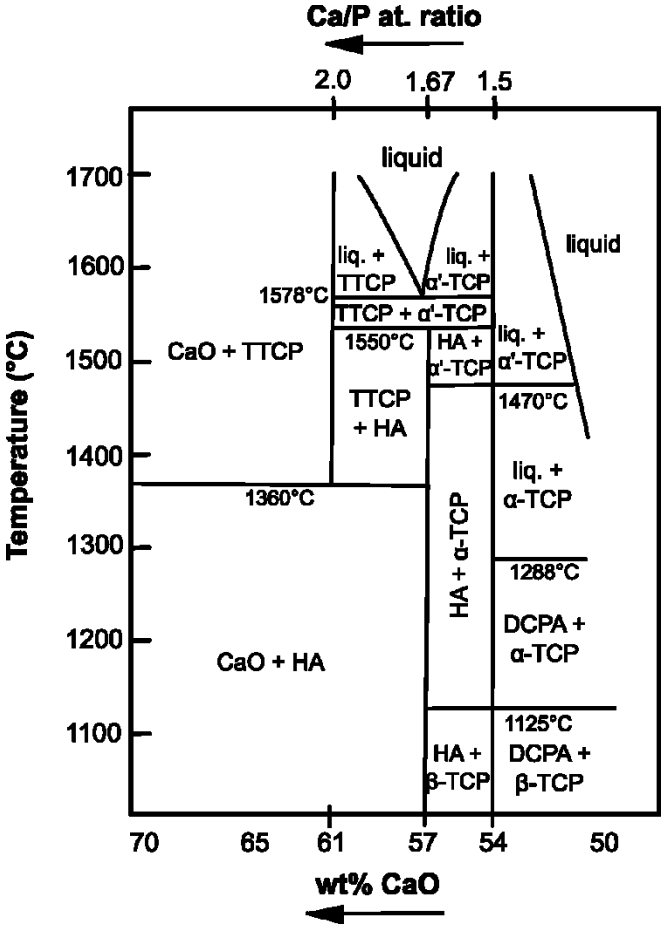

Figure 1-4 Equilibrium phase diagram of the system CaO-P_2O_5 with 500 Hg of water partial pressure. Redrawn from [38,39].

When water is present (Figure 1-4), DCPA is found instead of CPP. DCPA (monetite) is the anhydrous form of DCPD (brushite), both having Ca/P ratio equal to 1.0. DCPD is found in several pathological calcifications, while DCPA is never found in the human body. They are both used in

calcium phosphate cements and as additives in toothpastes. DCPD is also used as flame retardant, fertilizer, calcium supplement in food and bakery improver in the food industry [33].

Pure stoichiometric hydroxyapatite (HA or Hap, chemical formula $Ca_5(PO_4)_3(OH)$, often written $Ca_{10}(PO_4)_6(OH)_2$ to indicate that the unit cell comprises two chemical units) has a Ca/P ratio equal to 1.67 and it forms only in the presence of water (see Figure 1-4). The crystal structure of HA is hexagonal, space group $P6_3/m$ and cell parameters a = b = 9.437 Å and c = 6.878 Å. The unit cell presents $(PO_4)^{3-}$ tetrahedra, Ca^{2+} cations and OH^- anions arranged along the c-axis [37], which justifies an oriented growth along the c-axis [42].

Although pure HA is never found in the human body, its similarity with the bone mineral has made HA widely studied and used in the biomedical field. HA has excellent biocompatibility and osteoconductive properties and, therefore, it is applied as bone filler, bone tissue engineering scaffold, bioactive coating, drug/protein/gene delivery system, etc.. However, HA is the most stable and less soluble calcium orthophosphate after FA, which means that it is hard to be resorbed by the body. Another issue is its brittleness, which makes it not suitable for load bearing applications [42].

Calcium deficient hydroxyapatite (CDHA) forms by precipitation from aqueous solutions with Ca/P ratios in the range of 1.5-1.67. In the structure of CDHA some PO_4^{2+} ions are substituted by HPO_4^+ ions, so that the general formula can be expressed as

$$Ca_{10-x}(HPO_4)_x(PO_4)_{6-x}OH_{2-x} \qquad (2)$$

where $0 < x < 1$, thus ranging from Ca/P = 1.67 (HA, x = 0) to Ca/P = 1.5 (β-TCP, x = 1). The structure of CDHA can be considered as that of stoichiometric HA with vacancies in the crystal lattice and more disorder. When CDHA is heated at 1000-1200°C for 1-4 h, it transforms into HA and β-TCP [43], their relative quantities depending on the Ca/P ratio, as for the phase diagram in Figure 1-4. This biphasic material is also known as BCP (biphasic calcium phosphate), its solubility being in between those of HA and β-TCP and, since it contains β-TCP, it is more biodegradable than HA. For these reasons BCP is an attractive choice to be used as bone substitute.

Ca-deficient HA is thought to crystalize starting from amorphous calcium phosphate (ACP), that is the most unstable and disordered of calcium phosphates [44]. According to the Ostwald's step rule [45], the first compound that precipitates is not the most stable but rather a metastable phase that is kinetically favored and that transforms step-by-step into the most thermodynamically stable phase, through a series of high-energy states. Therefore, ACP is not stable as it rapidly converts into OCP and then into apatite, but it can be stabilized by the additions of cations, like Mg^{2+}, molecules (e.g. ATP, casein phosphopeptide and proteoglycans) and synthetic polymers, like poly(ethylene glycol) [46].

ACP is believed to be the precursor of crystalline apatite also in many biomineralization processes and it forms when phosphate and calcium ions are mixed in a supersaturated solution [46]. Even if ACP is an amorphous material, in 1974 Betts and Posner [47] proposed that it possesses a short-range order, suggesting the existence of ordered structures of about 9.5 Å, with formula $Ca_9(PO_4)_6$ [48], that are called Posner's cluster. The Ca/P ratio of ACP depends on the pH [45] and it varies from 1.18 to 2.50 [46]. Due to his role in biomineralization, ACP is considered a promising material to be applied in bone tissue engineering and in dentistry [49].

1.5 The bone apatite

The mineral phase of human bones and teeth has been idealized as hydroxyapatite, but it is actually very different from pure stoichiometric HA. Biological apatites show a wide range of composition, varying not only with the biological tissue (bone, dentine, enamel) but also within the same category. In his book chapter "Phosphate minerals in human tissues", LeGeros [41] identified the following characteristics for biological apatites:

1. Non-stoichiometry: Ca/P ratio of biological apatites ranges from 1.54 to 1.73;
2. Presence of impurities such as Na^{+}, Mg^{2+}, F^{-}, HPO_4^{2-}, CO_3^{2-} etc. that can be in the lattice and/or on the surface;
3. Co-existence of possible precursors like ACP and OCP.

A comparison between the average composition of human bone, dentine and enamel is reported in Table 1-3.

Table 1-3 Composition of human enamel, dentine and bone. Data expressed in %wt of dried tissue [41].

Composition	Enamel	Dentine	Bone
Calcium, Ca^{2+}	36.5	27.5	24.5
Phosphorus, P	17.7	13.0	11.5
Sodium, Na^{+}	0.3	0.6	0.7
Potassium, K^{+}	0.08	0.05	0.02
Magnesium, Mg^{2+}	0.34	0.81	0.55
Carbonate, CO_3^{2-}	3.5	5.0	6.0
Fluoride, F^{-}	0.01	0.02	0.02
Chloride, Cl^{-}	0.30	0.01	0.10
Pyrophosphate, $P_2O_7^{4-}$	0.02	0.08	0.05
Total organic	1.0	20.0	25.0

In bone apatites, impurities can substitute Ca^{2+}, PO_4^{3-} or OH^{-} in the apatite crystal, as schematically described in Figure 1-5. These impurities affect the morphology, the lattice parameters and the crystallinity of the bone mineral.

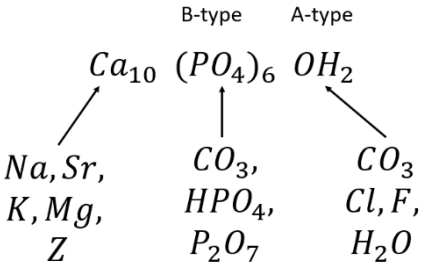

Figure 1-5 Schematic representation of impurities substitution in biological apatites. Z indicates trace elements (Pb, Ba, Zn, Fe and other cationic elements). B-type and A-type refer to the type of carbonate substitution. Modified from [41].

Calcium can be substituted by other cations, which are mainly Na^+, Sr^{2+}, K^+, and Mg^{2+}, but there are also other elements that are present only in traces, such as Pb, Ba, Zn, Fe etc.. Magnesium is known to inhibit the crystallization of apatite, favoring instead the formation of β-TCP, and to stabilize the amorphous phase (ACP).

All biological apatites contain significant amounts of CO_3^{2-} (~3.5-6 wt%), so that they are usually designated as carbonated hydroxyapatites. The carbonate ion can substitute either the PO_4^{3-} site, resulting in a so-called B-type carbonation, or the OH^- site, giving a A-type carbonation. Carbonate substitutions of type A or type B are visible through different bands in FT-IR spectra [50]. The incorporation of carbonate ions causes a reduction in the size of the crystallites, thus a reduction in the crystallinity, while increasing the solubility and decreasing the thermal stability [41].

It should be quite clear now that the bone mineral is not hydroxyapatite, but rather a particular kind of non-stoichiometric, carbonated and highly substituted apatite, that shows a high degree of crystal disorder. For this reason, the synthetic production of carbonated and ion-doped apatites is of great interest for bone tissue engineering [51–56]. Indeed, the incorporation of such ions in the apatite lattice was found to have beneficial effects on the bioactivity of the implant. For instance, Sr^{2+} is thought to contribute in the modulation of key molecules and in the regulation of genes that control bone resorption and promote osteoblastic cell proliferation [32,57,58]. Similarly, Mg^{2+} was found to stimulate bone formation and to promote bone cells adhesion and stability [59,60], possibly by affecting some ECM proteins and transcription factors [61].

However, the incorporation of many different ions in the lattice of HA is not costless or effortless. This is why natural sources of calcium minerals such as corals, eggshells, seashells and animal bones are very attractive for the production of bone-like apatite, which is the topic of the next paragraph.

1.6 Synthesis of HA from natural sources

Natural biological sources such as bone ash, eggshells and seashells are efficient, available and inexpensive materials to synthesize ion-doped HA, for they naturally contain those impurity ions (CO_3^{2-}, Na^+, Mg^{2+} etc.)

that play a crucial role in the life cycle of bone. In fact, the incorporation of one or more of these ions in synthetic HA is usually much more expensive than the production of pure HA and, besides, achieving a good match with the natural bone composition (Table 1-3) is highly challenging. On the other hand, the simple calcination of bovine bone into ash, for example, gives an apatite that contains many additional ions. According to Akram et al. [62], natural sources for extracting HA can be classified into bones, plants and biogenic sources (Figure 1-6).

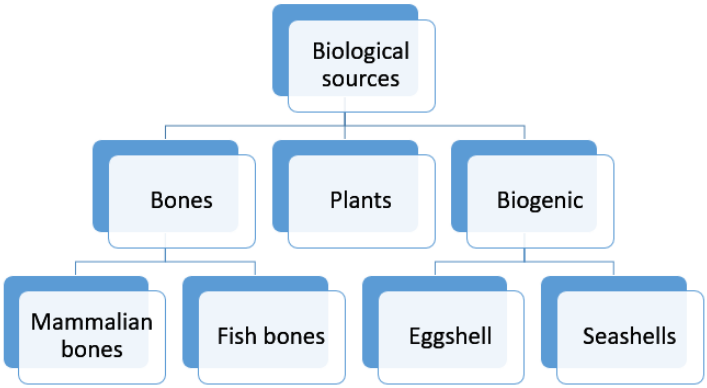

Figure 1-6 Classification of natural sources for the extraction of HA. From [62].

The biggest difference between these natural sources is that the original biological mineral is either apatite, as in the case of mammalian and fish bones, or calcium carbonate, as for plants, eggshells and seashells. It naturally follows that HA can be directly extracted from bones, while a phosphate provider is needed when dealing with $CaCO_3$ sources.

The extraction of HA from mammalian bones usually involves washing, boiling in distilled water, treating with NaOH or sodium ipochlorite to remove dirt and proteins and calcining between 600°C and 1400°C to completely remove the organic and destroy pathogens [62]. The resulting apatite contains many beneficial ions, but the original low-crystallinity and nanometric size can be lost due to the thermal treatment at high temperature. The most common mammalian bone used for tissue engineering purposes is bovine bone, which is even commercialized under the name of Nukbone® (Biocriss, Mexico) and whose bioactivity was found to be superior than that of pure HA [63].

The extraction of HA from fish bones is not different from that from mammalian bones, also requiring a calcination step [64]. Many different species of fishes were employed, as for example sword fish, tuna [65], cod fish [66] and tilapia fish scales [67].

While fish bones and scales are sources of apatite, other marine organisms are, instead, sources of $CaCO_3$. Calcium carbonate is found in marine organisms either in the form of calcite or of aragonite, which are two polymorphs of $CaCO_3$, and it can be used as biomaterial as-is or after its conversion into HA [68]. Indeed, hydroxyapatite was extracted from many marine sources including plants, such as red algae and corals, and animals, like sea urchins, seashells, marine sponges, starfishes, cuttlefishes, lobsters, crabs, sea cucumbers, snails and shrimps [69]. The term "biogenic", which is often referred to these calcium carbonates, indicates that they have a biological origin. Similarly, bird eggshells are also sources of biogenic calcium carbonate (calcite), which can as well be converted into HA and be used as biomaterial [70].

The most common route to synthesize HA from biogenic calcium carbonate is hydrothermal synthesis. This method basically consists of putting biogenic $CaCO_3$, a phosphate provider and water in a sealed vessel and heating it up to obtain vapor at high pressures. This method was first developed by Roy et al. [71] in 1974, who extracted HA from coral (aragonite) and whitlockite from starfish spines (calcite), using di-ammonium phosphate as phosphate provider. The expected reaction for the formation of HA is:

$$10CaCO_3 + 6(NH_4)_2HPO_4 + 2H_2O \rightarrow Ca_{10}(PO_4)_6(OH)_2 + 6(NH_4)_2CO_3 + 4H_2CO_3 \quad (3)$$

It is important to specify that, in the case of Roy et al. but also in other studies [72–74], the objective was to convert aragonite into HA while preserving the original structure of the natural materials, since they are often naturally porous and can therefore be used directly as scaffolds. The method developed by Roy et al. was used to extract HA from several marine organisms, for example corals [75], cuttlefish bones [76–80], mussel shells [81], oyster shells [82] and sea urchins [83]. In some cases [84–87], the hydrothermal process is preceded by a calcination/pyrolysis step, in order to transform $CaCO_3$ in CaO and to

burn off the organics. In other studies, the authors used a phosphate provider different from $(NH_4)_2HPO_4$, for example MCPA [88], DCPA [89,90], sodium phosphate [91] and phosphoric acid [92].

Another method to extract HA from biogenic sources is precipitation. The reactants, which are usually calcined calcium carbonate and phosphate salt, are completely dissolved in a pH-controlled aqueous solution and left soaking for many hours (from 24 h to 30 days), until HA precipitates. This method was used to extract HA from eggshells [93–96], oyster shells [97] and sea snails shells [98]. In other works [99–102], precipitation was promoted by exposing the solution to microwave irradiation.

Finally, mechanosynthesis (or mechanochemistry) is one of the most straightforward method to synthesize HA. The mechanochemical reaction is defined as a ''chemical reaction that is induced by mechanical energy'' [103] and it is carried out simply by milling the reactants with high energy. The milling process can be performed in dry conditions (dry milling) or using a liquid media like water, isopropanol or ethanol (wet milling), which is preferable to not reach too high temperatures.

Wet ball milling was already employed to synthesize calcium phosphates from eggshells [104–110], cuttlefish bones [111–113], oyster shells [114] and clam shells [115]. Although, theoretically, only mechanical energy is needed for carrying out a mechanochemical reaction, many of these studies reported a more complex procedure, involving either an initial calcination step [105,109,111,113,115], a final heating step [111,114–116] or a final sintering [104,105,112]. Ferro and Guedes [117], instead, used only high energy ball milling to synthesize HA from cuttlefish bones and chicken eggshells. They found that the reaction path is different for the two biological materials and that the aragonite from cuttlefish bones requires less energy than the calcite from eggshells.

Many variables may affect the mechanosynthesis process, for example milling time, milling speed, ball-to-powder mass ratio, material of milling balls and vial, filling extent of the vial, type of liquid media (if present) and milling atmosphere. The ball-to-powder weight ratio quantifies the amount of balls with respect to the amount of powder and can vary between 1:1 to ~200:1, being 10:1 the most commonly used in small mills [103]. Moreover, since the stability of calcium orthophosphates is

influenced by the pH (see Table 1-2), the pH of the liquid media is also an important parameter for the mechanosynthesis of HA.

1.7 Biogenic calcium carbonates

Calcium carbonate, $CaCO_3$, is a mineral that is abundant in nature and it is found not only in rocks but also in many biological organisms. Calcium carbonate is polymorphous and occurs in three anhydrous crystalline forms: calcite, aragonite and vaterite. Moreover, there are two crystalline forms that exist only at high temperature (calcite II and III) and two hydrated modifications, which are calcium carbonate monohydrate and calcium carbonate hexahydrate [118,119]. Amorphous calcium carbonate (ACC), is also found in biological systems, and it is thought to be the precursors of the crystalline forms in the biomineralization processes [120].

Table 1-4 Crystal structure of the three anhydrous polymorphs of calcium carbonate.

Polymorph	**Symmetry**	**a (Å)**	**b (Å)**	**c (Å)**	**Crystal morphology** [118]
Calcite [121]	Trigonal	4.976	4.976	16.992	Rhombohedral
Aragonite [122]	Orthorhombic	4.962	7.969	5.743	Needle-like
Vaterite [123]	Hexagonal	4.130	4.130	8.475	Spheroidal

Calcite has a trigonal crystal symmetry and it is the most stable form of calcium carbonate at room temperature and atmospheric pressure while aragonite is considered to be less stable and it has an orthorhombic crystalline structure [118,124]. Both calcite and aragonite are very commonly found in biogenic formations. Vaterite, instead, is quite rare and it is less stable than the other two polymorphs, as it transforms to calcite or aragonite when exposed to water [125].

Marine organisms often contain calcite or aragonite minerals. Due to the fact that their structure is usually highly porous, they attracted some attention from scientists in the field of BTE [68]. These organisms can selectively form either calcite or aragonite, and sometimes even both, depending on the different location in their body. The mechanism that

allows them to induce the formation of one polymorph rather than the other one is thought to be related to the macromolecules of the substrate, for example β-chitin and silk fibroin may induce the formation of aragonite instead of calcite [126]. The $CaCO_3$ polymorphs of some marine organisms are listed in Table 1-5.

Table 1-5 Calcium carbonate polymorphs of some marine organisms. Modified from [69].

Marine organism	Calcium carbonate polymorph
Red algae	Calcite
Corals	Aragonite
Snails, limpets	Aragonite
Clams, mussels	Aragonite/Calcite
Lobster, crab, shrimp	Aragonite
Cuttlefish	Aragonite
Starfish	Calcite
Sea urchins	Calcite
Sea cucumbers	Calcite

Cuttlefish bone or cuttlebone is the internal shell of cuttlefish (*Sepia Officinalis),* a marine mollusk of the order *Sepiida.* Cuttlefishes are a type of cephalopods (like octopuses and squids), which account for around 2.5% of the global seafood production, being Japan the principal consumer of cephalopods in the world [127,128]. Since 1961, cephalopods have increased in relative terms by 416% to reach an all-time maximum of around 4 million tons in 2013, before dropping to around 3 million tons in 2019 [128]. Scientists think that the main reasons could be two. First, intensive fishing in the last decades has decimated the fish population that are the cephalopods' natural predators, like sharks, big bony fishes and marine mammals. Second, the temperature increase of the ocean due to global warming could have accelerated the life cycle of cephalopods [129].

The cuttlebone has the functions of being the rigid structural component of the cuttlefish body and to serve as a buoyancy tank for the cuttlefish, providing an efficient means to maintain its vertical position in the sea. A gas and liquid mixture is used to regulate the pressure inside the

cuttlebone via an osmotic process, allowing the cuttlefish to maintain its neutral buoyancy [130].

Cuttlefish bones are composed of two main parts, the dorsal shield and the lamellar matrix, as shown in Figure 1-7a. The first is a dense, hard and rigid structure which acts as protection for internal organs and constitutes the skeletal structure. The second is an extremely porous structure (up to 90% porosity) that is responsible for the pressure regulation. It is composed by numerous lamellae that forms many chambers called *septa* that are supported by numerous pillars [131]. The mineral that forms the cuttlebone is aragonite, which is embedded in an organic matrix of β-chitin, that was estimated to be around 3-4.5 wt% in the internal lamellar matrix and 30-40 wt% in the dorsal shield [131].

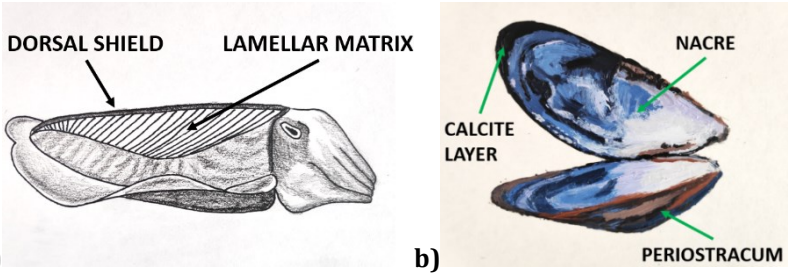

Figure 1-7 Illustrations of a cuttlefish (a) and of a mussel shell (b).

Mussels belong to the *Mytilus* genus and, like all bivalves, are composed of two almost identical shells. In 2016 the global production of mussels was of about 2 million tons, mainly cultured in China, E.U. (Spain and France above all), Chile and New Zealand [132]. The shells are a defensive system for the mussels, with the function of protecting the mollusk from external attacks. Mussel shells are composed of 95-99% calcium carbonate and 1-5% organics [133]. In their cross-section, three different layers can be observed: (i) the *periostracum*, which is the outermost thin organic layer (about 40 μm), with the function of protection against chemical etching and abrasion, mainly composed of proteins, proteoglycans and polysaccharides [134,135]; (ii) a middle layer of about 400 μm, composed of calcite crystals; (iii) the inner surface of the shell, a thin layer of about 10 μm made of aragonite crystals, which shows a typical iridescent color and it is generally called nacre.

The sea is not the only place where biogenic calcium carbonate is found, since all avian eggshells are composed by biogenic calcite. Eggshell is one of the most common food waste and its world production is estimated to be around 50'000 tons per year [136]. Eggshells are essential for all the bird species because, thanks to their unique sophisticated structure, they perform several important functions. The eggshell must protect the embryo from the external physical and microbial environment, while, at the same time, it must be easily broken by the baby bird when it's time for it to hatch out. Moreover, the eggshell allows the passage of water and gases through pores during the extra-uterine life of the embryo and it also provides calcium for the embryo development [137].

The main component of eggshell is calcite, which accounts of about 94–97% of the total weight, while the other constituents are $Ca_3(PO_4)_2$ (1%), $MgCO_3$ (1%), and organic material (4%) [136]. The structure of the shell can be divided in six different layers, from the inside to the outside: two uncalcified membranes, both made up of a network of fibers and composed by fibrillary proteins and collagen types I, V and X; an inner calcified layer made of irregular cones called *mamillae*; the thickest part of the shell, called palisade layer; a thin vertical crystal layer with crystals aligned perpendicularly to the surface; and an outer thin organic layer called cuticle. Also the calcified zones contain a little part of organics, mainly glycoproteins and proteoglycans [137,138].

In the present thesis work, cuttlebones (CB), mussel shells (MS) and chicken eggshells (ES) were used as biogenic sources of calcium carbonate to synthesize calcium phosphates for bone regeneration applications. They were selected because of their abundance and availability, as well as for their different crystallographic composition: aragonite in CB, calcite in ES and aragonite/calcite in MS.

1.8 Additive manufacturing of bioceramic scaffolds

In the 2018-2019 biennium about 15'000 articles dealing with additive manufacturing (AM) were published on scientific journals, a fact that gives an idea of the increasing attention that this technology is attracting from scientists and engineers. In many cases these publications also highlight the potential use for bone tissue engineering [139].

With respect to conventional methods, AM technologies have several advantages for the fabrication of scaffolds for bone regeneration. First of

all, by using a three-dimensional computer aided design (CAD) model, it is possible to fully design the scaffold's porosity. As mentioned in paragraph 1.2, porosity is crucial not only for the mechanical properties, but also for the formation of blood vessels, for storing and protecting the bone marrow and for hosting the bone cells. Moreover, the geometry of the pores was found to have an influence on the bone cells, since tissue regeneration increases with curvature and on concave surfaces [140]. In contrast to AM, porosity is not easy to control with conventional scaffolds fabrication technologies such as chemical/gas foaming, solvent casting/particulate leaching, freeze drying, thermally induced phase separation and foam-gel [141,142]. Another important advantage of AM is that, by using x-ray computed tomography on the bone defect site, the shape of the scaffold can be fully customized to be patient-specific, without using any mold [143].

Polymers, metals, ceramics and composite materials can all be 3D printed with different AM processes, such as SLA (stereolithography), SLS (selective laser sintering), SLM (selective laser melting), FDM (fused deposition modelling), robocasting or DIW (direct ink writing) and binder jetting or P-3DP (powder 3D printing) [141,144]. SLA is a process that uses UV light to crosslink sequentially deposited layers of a photosensitive resin, while FDM, instead, consists of extruding a thermoplastic material through a printing nozzle [144,145]. In P-3DP, a liquid binder is selectively spit onto a powder bed, binding together the desired particles layer by layer, while in SLS and SLM the selected spots of the layers are consolidated through the heat provided by a laser beam. These processes can be applied to powders (P-3DP, P-SLS and P-SLM) or to slurries (S-3DP and S-SLS) [146]. DIW is somehow similar to FDM, where the material extruded is not a thermoplastic polymer but a ceramic paste. In this work, bone scaffolds are fabricated by FDM and P-3DP and therefore their schematic illustrations are shown in Figure 1-8.

When coming to the material choice, most processes have a limited range of printable materials, mainly consisting of synthetic polymers and metals [146]. In fact, polymers are very easily processed: thermoplastics can be extruded (FDM), while polymeric resins can be hardened by heat or by UV light (SLM and SLA). Metals are usually processed in the form of powders and consolidated by local heating (SLS). Either way, in the case of both polymers and metals, a finite component is produced with the 3D printing process. Ceramics, instead, due to their very high melting

temperature, usually need to be post-processed after printing to be consolidated. Either printed as slurries, pastes or powders, green ceramic parts are bound together by binders, which are for example liquid polymeric resins, photocurable polymers or organic substances [147]. After that, the binder needs to be removed and the part needs to be consolidated by a sintering process. It is worth to mention, though, that this is not the case of cements, because they harden simply by the addition of water, which is used as binder.

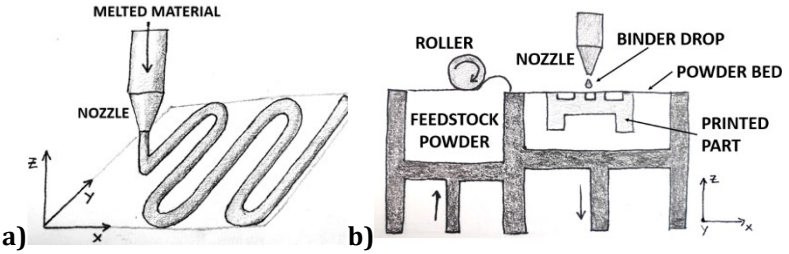

Figure 1-8 Simple illustrations of an extrusion-based 3D printing process or FDM (a) and of a powder 3D printing process (P-3DP) (b).

In bone tissue engineering (BTE), bone ceramic scaffolds were 3D printed by SLS, SLA, FDM, P-3DP and DIW by using several calcium phosphates, such as HA, β-TCP, α-TCP, biphasic HA/β-TCP, tetracalcium phosphate and octacalcium phosphate [148,149]. In general, two different approaches can be followed: either the ceramic material is used in combination with a polymer to form biocomposite scaffolds, or it is used alone to obtain pure bioceramic scaffolds. Both approaches have pros and cons, as described in paragraph 1.3 when discussing the properties of the different materials used in BTE. In the SLS process the ceramic powders are usually blended with polymers such as PLA [150], PDLLA [151], PCL and PEEK [152] to form composite materials. The same is applicable for FDM, for example by using calcium phosphates like HA and β-TCP as fillers in PLA [27–29] or PCL [24,25,30–32]. Conversely, P-3DP, SLA and DIW allow to fabricate pure ceramic scaffolds.

In the frame of this thesis work, we are particularly interested in the 3D printing of ion-doped and naturally derived calcium phosphates. Gómez-Lizárraga et al. [63] fabricated composite scaffolds via extrusion 3D printing using PCL and HA derived from bovine bones. They compared

pure PCL, PCL with synthetic-HA and PCL with bio-derived HA, finding that cells proliferation *in vitro* was highest on samples containing 10 wt% of bovine bones-derived HA. Similarly, Jiang et al. [153] used the same AM process to produce a 3D printed PCL/bovine-HA scaffold, which was then implanted into a 1.5-year-old dog. The experiment showed good bone ingrowth and connection with the surrounding tissue. More recently, Sr-doped nano-HA was used to fabricate pure ceramic scaffolds by DIW. The *in vitro* tests showed better cell proliferation and differentiation for the samples with 5% of Sr [154] and with 10-15% of Sr [155]. DIW was also used by Mocioiu et al. [156] to 3D print bone scaffolds by using *Rapana venosa* shells-derived HA, resulting in a cell viability similar to that of synthetic HA. The SLS process was instead used to fabricate composite scaffolds made of PLLA and cuttlefish bone powder [157]. Interestingly, the hydrothermal transformation of the cuttlebone into HA was performed after printing. The biological tests revealed that the scaffolds were non-cytotoxic.

When considering candidate materials for AM processes, one of the main technological aspects to take into account is the powder size distribution (PSD). For example, in extrusion-based processes, the main limitation is the size of the nozzle, which of course should be bigger of the dimensions of the ceramic particles. When, instead, coming to powder-based processes such as P-3DP, P-SLS and P-SLM, the particle size is important for obtaining a smooth and regular powder flow, which is desirable to have a flat and smooth surface of the powder bed. This property of the powders is called flowability. Moreover, the particle size distribution determines the density of the powder bed and therefore of the green object, that is crucial to achieve high densification during sintering.

In this perspective, it is very difficult to 3D print very fine powders or even nanopowders, which is usually the case of bio-derived calcium phosphates, as a result of their synthesis process. In fact, very fine powders tend to stick together due to their high specific surface area (SSA) and to form green parts with very low-density. As a reference, one shall consider that powder-based processes usually require particle sizes in the range of 30-100 μm in order to achieve good powder flowability and densification [146]. It is therefore not surprising that, so far, there are no studies about P-3DP of bio-derived nano-HA, while other technologies like DIW or the use of composite materials are instead preferred.

Aim of the work

The first objective of the present work is to synthesize bone-like apatite starting from biogenic calcium carbonate sources, namely cuttlefish bones, mussel shells and eggshells. Moreover, the second objective is to use these bio-derived materials to produce scaffolds for bone regeneration by 3D printing.

Chapter 2

Biogenic raw materials

2.1 Introduction

This chapter deals with the characterization of the raw materials used in this thesis work. These are biogenic calcium carbonates, namely cuttlefish bones (CB), eggshells (ES) and mussel shells (MS). Part of the material of this chapter has been already published in [158].

2.2 Methods

Cuttlefish (*Sepia Officinalis*) bones were collected from several local fish shops, where they had been stored in the refrigerator until collection. Mussel shells (*Mytilus Galloprovincialis*) were kindly supplied by a local restaurant, possibly after being cooked and served to customers, therefore most likely being exposed at temperatures below 200°C. Chicken eggshells, instead, were collected "fresh" in a local bakery, after being separated from yolks and albumens. The organic layer of MS, *periostracum*, was manually removed, while the two internal organic membranes of the ES were instead kept.

Then, all materials were rinsed under tap water and boiled in demineralized water for 10 min, in order to remove bacteria and other possible microorganisms. Afterwards, they were dried overnight in an oven at 100°C. Some CB, MS and ES were kept aside for the SEM analysis, while all the others were ground into powders in a centrifugal mill (Retsch S100) working at 400 rpm for 30 min. The powders were then sieved, in order to eliminate particles larger than 300 μm.

The morphology of the three biogenic powders and of the cross-sections of a cuttlebone, a mussel shell (with *periostracum*) and an eggshell were observed by field emission scanning electron microscopy. Images were taken with a FE-SEM SUPRA 40 (Carl Zeiss Microscopy GmbH) instrument, using secondary electrons and energy 3.00 kV. The FE-SEM images were analyzed with the software ImageJ.

Thermal analyses (TGA/DTA) were performed to evaluate the $CaCO_3$ content and organic matter in the biogenic powders. The analyses were carried out using a NETZSCH Geraetebau GmbH STA 409 thermobalance. The tests were performed by heating the samples in an alumina crucible from room temperature up to 975°C at 10°C/min in flowing air.

The crystalline phases were characterized X-ray diffraction (XRD), using an Italstructures IPD3000 X-ray diffractometer, equipped with a Co anode source (Kα radiation 1.78892 Å), a multilayer monochromator to suppress k-beta radiation and fixed 100 μm slits. The powder samples were put in reflection geometry, with a fixed omega angle with respect to the incident beam. An Inel CPS120 detector was used to collect the diffraction data over 5°-120° 2-theta range (0.03 degrees per channel). The quantitative analysis was done with the Rietveld software Maud [159], using the database COD [160] to download the following crystal phases: calcite n. 4502443 [121], aragonite n. 2100187 [122]. The JCPDS cards were instead taken from the PDF2-2004 database.

The FT-IR analyses were carried out in order to support and confirm XRD data. The spectra were collected with a FTIR Thermo Optics Avatar 330, in transmission mode, using KBr pellets, over the 4000–400 cm^{-1} range.

The presence of ions and trace elements (Na, K, Mg, Sr, Zn) in the biogenic powders was estimated by Inductively Coupled Plasma/Optical Emission Spectroscopy (ICP/OES), using a Spectro Ciros Vision CCD (125–770 nm). The samples were solubilized in ultrapure nitric acid (70 vol%, Sigma–Aldrich) and diluted with pure water (obtained by reverse osmosis, $\sigma < 0.1$ μS cm^{-1}).

2.3 Results and discussion

Some SEM pictures of the cross-section of a cuttlefish bone are shown in Figure 2-1. The two different regions, dorsal shield and lamellar matrix, are clearly visible. The thickness of the dorsal shield is 249 ± 19 μm, as measured with the software ImageJ. The lamellar matrix, instead, is formed by many different chambers of height 469 ± 12 μm and width 107 ± 14 μm.

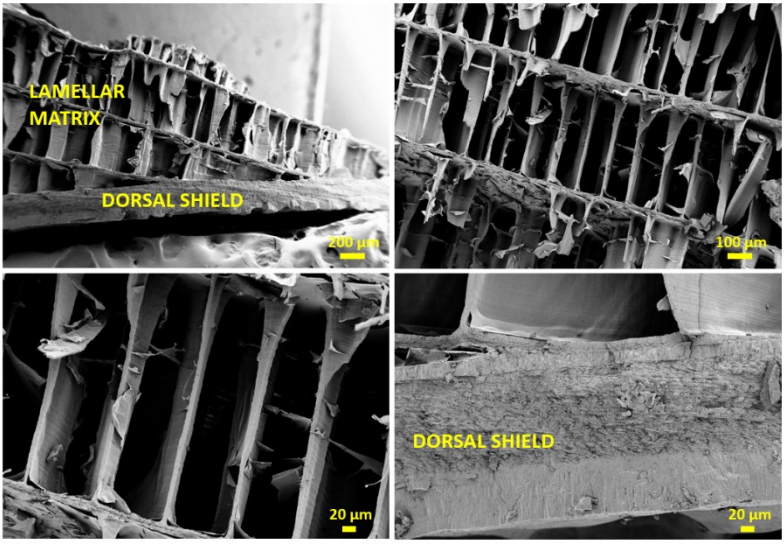

Figure 2-1 SEM pictures of the cross-section of a cuttlefish bone.

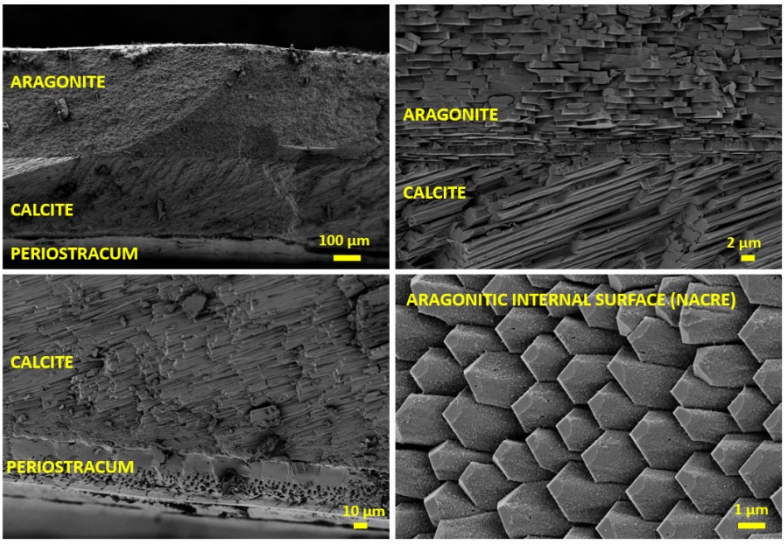

Figure 2-2 SEM pictures of the cross-section of a mussel shell and of the internal surface (bottom, right) of a mussel shell.

The cross-section and the internal surface of a mussel shell are shown in Figure 2-2. As already explained in paragraph 1.7, the cross section of the shell is characterized by three different layers: an external organic layer called *periostracum*, a middle layer made of calcite crystals and an inner aragonitic layer with the typical iridescent color, also known as nacre or mother of pearl. The iridescence of nacre is due to the periodicity of the stacked aragonite crystals [161], that is comparable to the wavelength of light [162]. The beautiful structure of nacre can be observed in Figure 2-2, both in the surface view (bottom, right) and in the cross-section (upper, right), where the stacked aragonitic tiles are clearly visible. The thickness of the nacre's platelets, measured with ImageJ, is 993 ± 68 nm, which is just slightly larger than what reported in the literature [161] and of the wavelength of light (400-700 nm). In the image reported in Figure 2-2 (upper, left), the thickness of the nacreous layer is 432 ± 9 μm and that of the calcitic layer is 307 ± 8 μm. However, the nacre's thickness is not constant along the shell, it decreasing from the center to the borders, where it is completely absent. The *periostracum*, instead, was measured to be 38 ± 1 μm thick.

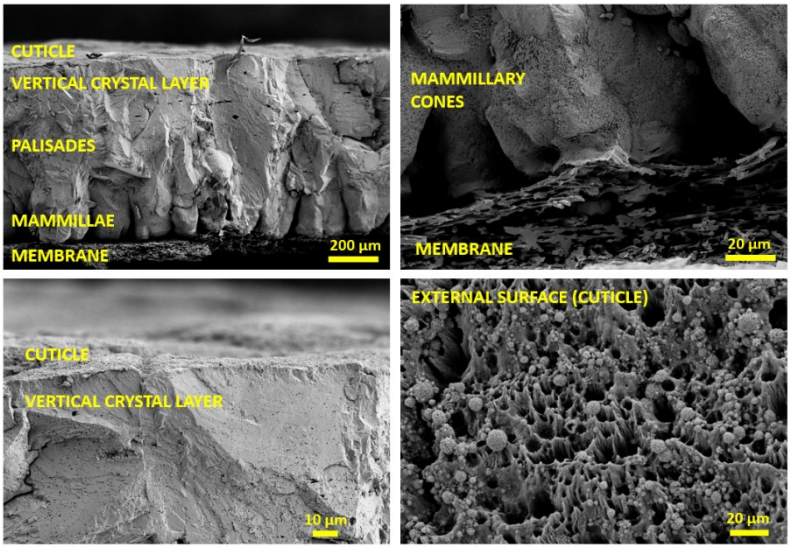

Figure 2-3 SEM pictures of the cross-section of an eggshell and of the external surface (bottom, right) of an eggshell.

An eggshell's cross-section and external surface are shown in the SEM pictures of Figure 2-3. The different layers of the eggshell are marked in the pictures following the explanation of paragraph 1.7. However, a clear separation between the *mammillae*, the palisade layer and the vertical crystal layer is not visible and therefore their individual thickness was not calculated. The peculiar porous structure of the cuticle is visible in the picture of the external surface (bottom, right), where the spherical aggregates most likely correspond to small hydroxyapatite crystals [138]. The total thickness of the calcitic part of the shell was measured to be 346 ± 4 μm, while that of the fibrous organic membranes is 33 ± 5 μm.

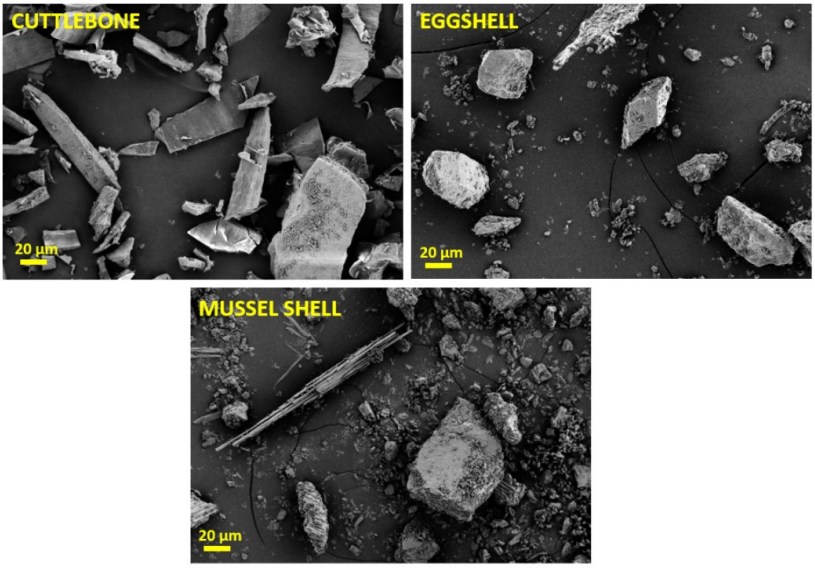

Figure 2-4 SEM pictures of the three biogenic powders.

The SEM pictures of cuttlebones, eggshells and mussel shells after being ground into powders by milling are reported in Figure 2-4. The particles show irregular shapes and sizes from few micrometers to 100-200 μm. Moreover, particles of organic material are visible in all three biogenic $CaCO_3$ powders.

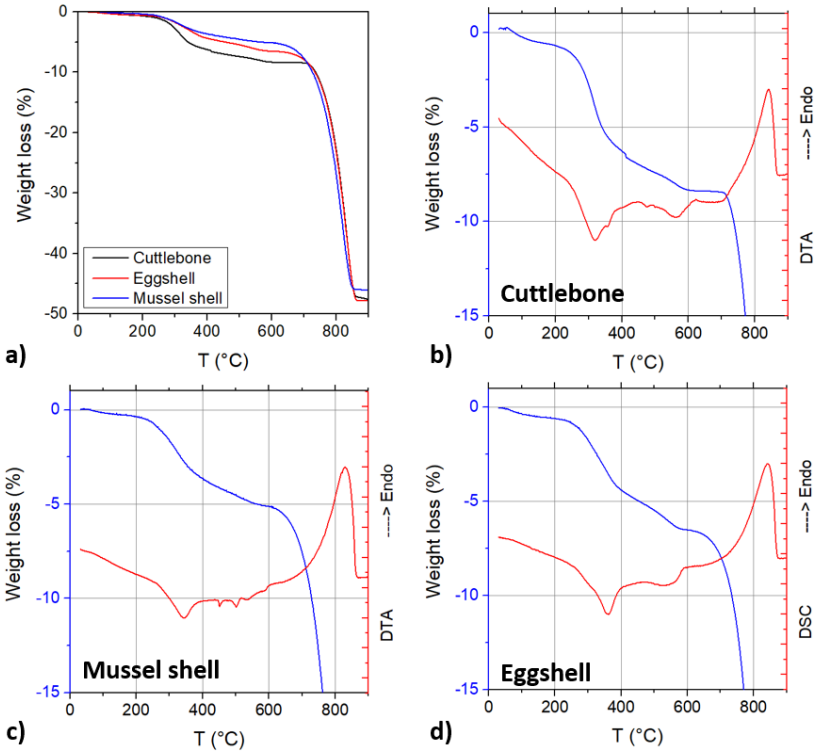

Figure 2-5 TGA/DTA diagrams of the biogenic calcium carbonate powders: all weight losses (a) and first part of the weight loss curves with DTA of cuttlebone (b), mussel shell (c) and eggshell (d).

The DTA/TG diagrams of the three biogenic $CaCO_3$ powders are shown in Figure 2-5. In the TGA diagrams, four different weight losses can be distinguished, as listed in Table 2-1. The first loss is observed at temperatures below 150°C and corresponds to the evaporation of water, while the second weight loss occurs at 250°C-380°C and it is related to the exothermic decomposition of proteins and other organics. A third mass reduction is visible at 380°C-600°C, and, as in [163], can be associated with the decomposition of residual organic. Finally, a large weight decrease corresponding to calcination (endothermic) occurs at 700-850°C.

Table 2-1 Weight losses of the biogenic powders as estimated by TGA.

	Cuttlebone	**Mussel shell**	**Eggshell**
1st loss (water)	0.7%	0.4%	0.6%
2nd loss (proteins and residual organics)	5.3%	3.0%	3.5%
3rd loss (residual organics)	2.4%	1.7%	2.1%
4th loss (calcination)	38.8%	41.1%	41.6%
Total loss	47.2%	46.0%	47.8%
Total $CaCO_3$	91.6%	94.9%	93.8%
Total organics	7.7%	4.7%	5.6%

The thermogravimetric analyses allowed to calculate the relative amount of calcium carbonate and organic material in the biogenic powders, an information that is used in the following chapter for the synthesis of calcium phosphates: the $CaCO_3$ content was estimated to be 91.6%, 94.9% and 93.8%, in the cuttlefish bone, mussel shell and eggshell powder, respectively. The cuttlebone powder contains the larger amount of organics, 7.7%, most likely because both the lamellar matrix and the dorsal shield were used to produce the powder, the dorsal shield containing about 30-40% of organics [131], as already mentioned in paragraph 1.7. As for mussel shells, even if the *periostracum* was manually removed, the organic content in the powder was found to be consistent with the literature [133], it being 4.7%. In fact, in addition to the *periostracum*, other organic material is present

also in the mineralized layers of the shell; for example, β-chitin and glycine- and alanine-rich proteins are the matrix where the aragonitic tiles of nacre are embedded [126]. Anyhow, it can also be observed that the organic contents estimated with TGA analyses all seem to be slightly larger than the values found in the literature. For eggshells, for example, 5.6% of organics is found by TGA, while in [136] it is reported about 4%. Anyhow, the deviation is really small and can be attributed either to the raw materials, that have an intrinsic variability, either to small differences in the experimental methods.

X-ray diffraction diagrams of the three biogenic powders are shown in Figure 2-6. The spectra were acquired on the powders as-is and after heating them at 420°C and 600°C (ramp 10°C/min, dwell 1 h). This was carried out in order to investigate any eventual phase transformation before calcination. As expected, cuttlebone was found to be composed by aragonite, eggshells by calcite and mussel shell by a mixture of calcite and aragonite. The relative quantity of aragonite and calcite in MS, as estimated by the Rietveld method, is about 70 wt% calcite and 30 wt% aragonite.

In all cases, but especially for ES and CB, the relative intensity of the diffraction peaks differs from standard calcite and aragonite, as can be seen by comparing the spectra with those in Figure 2-6d. This is not surprising, because biogenic calcium carbonates very often show a texture, due to a preferred orientation and growth direction of the crystals during biomineralization. Indeed, texture in cuttlefish bones has been already observed by Rocha et al. [76], who noted a great difference in the peak intensities between spectra taken with the X-ray incidence beam parallel or perpendicular to the direction of the lamellae. The eggshell, instead, was shown to have a texture gradient [137], which allow it to fulfill its needs: large crystals on the external surface, separated by thin organic layers, absorb the impacts from outside; while small spherulitic crystals in the inner *mammillae* layer make the cracks propagation easier, in order to be easily broken from the inside. According to Nikolayev et al. [164], mussel shells possess crystallographic textures both in the calcite and in the aragonite layers, the calcitic one showing a sharper texture than the nacreous aragonitic layer. Moreover, they found that nacre shows a change in texture depending on its position in the shell, while calcite does not.

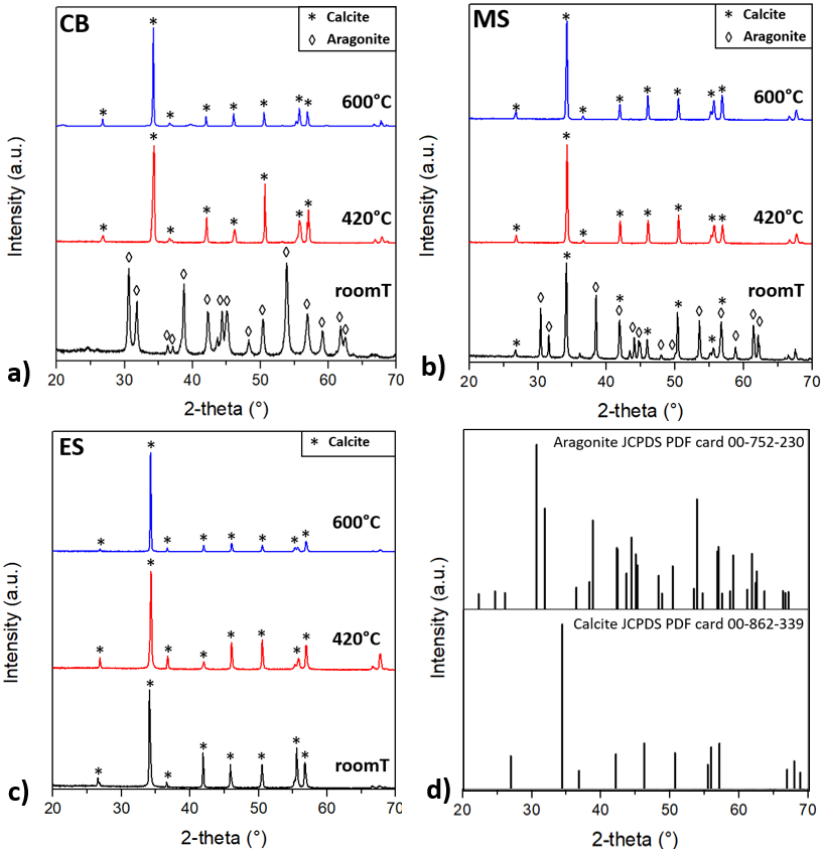

Figure 2-6 XRD spectra of cuttlebone (a), mussel shell (b) and eggshell (c) powders at room temperature and after heat treatment at 420°C and 600°C. Standard intensities of XRD reflections of aragonite and calcite from JCPDS cards (d).

The XRD data of the heated powders in Figure 2-6 show that the aragonitic phases of the cuttlebone and mussel shell powders convert into calcite upon heating. This is due to the fact that aragonite is a bit less stable than calcite, as already explained in paragraph 1.7. Moreover, one can observe that the crystallographic texture of the calcite crystals in the heated CB powder changes upon heating from 420°C to 600°C (Figure 2-6a), while the same effect is not clearly observable for the MS powder (Figure 2-6b). Similarly, the ES calcite shows different textures among

samples that were subjected to different thermal treatments, none of them corresponding to standard calcite (Figure 2-6c). The reasons for such behavior are probably complex, and specific XRD texture analyses would be needed to go deeper in this topic. However, this is not the objective of this study and therefore will not be further discussed.

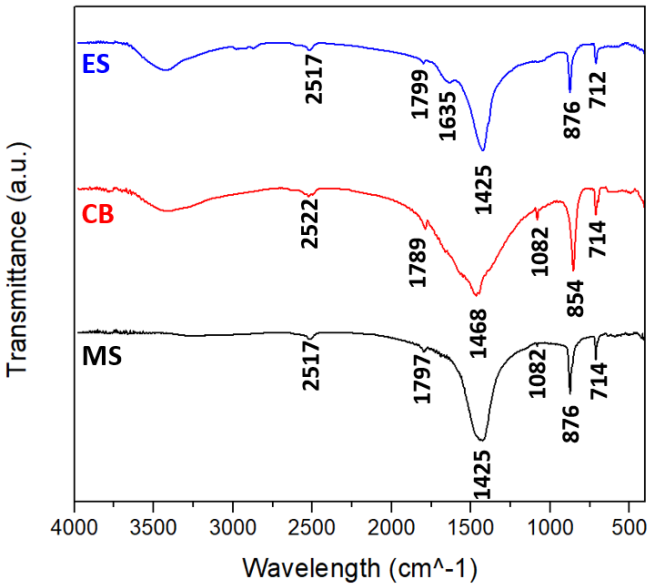

Figure 2-7 FT-IR spectra of eggshell (ES), cuttlebone (CB) and mussel shell (MS) powders.

The FT-IR spectra of the three biogenic powders are shown in Figure 2-7. All infrared absorptions are related to the carbonate vibrational modes [165,166], with the exception of the peaks corresponding to water at ~ 1635 cm^{-1} and at ~ 3400 cm^{-1}. These results also confirm the XRD analyses, since the aragonite phase in CB and MS is highlighted by the presence of the characteristic peak at 1082 cm^{-1}, which is associated with the symmetric carbonate stretching vibration (ν_1). The predominance of calcite in ES and MS is also revealed by the out-of-plane bending vibration (ν_2) at 876 cm^{-1}, typical of calcite, while in the CB spectrum the same vibrational mode is found at 854 cm^{-1} , which is typical for aragonite [118].

The presence of additional elements in the natural $CaCO_3$ sources was analyzed with ICP/OES and the results are listed in Table 2-2. Phosphorus and sodium are present in all samples, the content of P being very similar among the different natural sources (0.17 wt%), while Na being present especially in CB (0.68 wt%). Traces of Mg and Sr were also detected in all the three biogenic powders, magnesium being present in a larger amount in ES (~0.4 wt%) and strontium in CB (~0.2 wt%). The presence of Sr in cuttlebone and Mg in eggshell is already well known, as reported in other research works [138,167–169]. Moreover, cuttlebones shows also traces of K and Zn, and eggshells of K and Ba.

Table 2-2 ICP/OES semi-quantitative analyses (wt%) of trace elements in the biogenic powders.

Biogenic $CaCO_3$	P	Na	K	Mg	Sr	Other relevant traces
Cuttlebone	0.17	0.68	< 0.1	< 0.1	0.17	Zn
Mussel shell	0.17	0.30	-	0.1	0.1	-
Eggshell	0.17	0.13	< 0.1	0.35	< 0.1	Ba

2.4 Conclusions

Cuttlefish bones, mussel shells and chicken eggshells are biogenic sources of calcium carbonate, which constitutes, respectively, the 91.6%, 94.9% and 93.8% of their weight, while the rest is composed of absorbed water and organics. The $CaCO_3$ crystals are 100 wt% aragonite in cuttlebone, 100 wt% calcite in eggshell and 70/30 calcite/aragonite in mussel shell. The XRD spectra showed some texture in all samples, highlighting that these biogenic crystals have a preferential orientation. Moreover, other elements like P, Na, Mg and Sr were found in small amounts in all the three biogenic powders, especially Mg in eggshells and Sr in cuttlebones.

Chapter 3

Synthesis of bone-like apatite from biogenic calcium carbonates

3.1 Introduction

The synthesis of bone-like apatite powders starting from cuttlebones, eggshells and mussel shells powders is discussed in this chapter. The process used is basically a wet mechanosynthesis followed by drying in an oven at relatively low temperatures (up to 150°C). The process efficiency was studied in terms of efficiency by analyzing the influence of the following parameters: milling time, initial pH of the milling media and drying temperature. Part of the content of this chapter has been already published in [158].

3.2 Methods

The three biogenic $CaCO_3$ powders (cuttlebone, CB; mussel shell, MS; eggshell, ES) described in Chapter 2 were used for the synthesis of hydroxyapatite. The raw material was mixed with an aqueous solution in a 250 ml polyethylene bottle with 5 mm diameter zirconia balls (ball mass = 0.5 g), with ball-to-powder mass ratio equal to 10:1, using a planetary mixer (Turbula® T2F) working at 90 rpm.

The initial pH, measured with a laboratory pH-meter, was varied to perform the ball-milling in three different aqueous solutions:

1. ammonium phosphate dibasic ($(NH_4)_2HPO_4$) - initial pH = 8.5;
2. ammonium phosphate dibasic ($(NH_4)_2HPO_4$) and ammonium hydroxide (NH_4OH)- initial pH = 13;
3. phosphoric acid (H_3PO_4)- initial pH = 3.2.

Ammonium phosphate dibasic, CAS: 7783-28-0, was purchased from Fluka; the phosphoric acid, ~ 85 % H_3PO_4, CAS: 7664-38-2, from CARLO ERBA Reagents and the ammonium hydroxide, ~ 28-30% NH_4OH, CAS: 1336-21-6, from Sigma-Aldrich.

The relative quantities of the reactants ($CaCO_3$ and PO_4^{3-}) were set in order to have a Ca/P molar ratio equal to 1.67 (hydroxyapatite). The amount of $CaCO_3$ in the biogenic powders was estimated by thermogravimetric analysis, as discussed in the previous chapter. Different milling times were considered, from 30 min to 72 h. After milling, the slurry was dried for 24 h at different temperatures, 25°C, 90°C, 120°C and 150°C.

The output of each reaction, i.e. the conversion of aragonite and/or calcite into hydroxyapatite, was evaluated by XRD. As in the previous chapter, the used X-ray diffractometer was an Italstructures IPD3000, Co Kα radiation (1.78892 Å), detector Inel CPS120, 5°-120° 2-theta range (0.03 degrees per channel). The spectra were analyzed with the software QualX and Maud [159]. For Maud, the database COD [160] was used to download the following crystal phases: calcite n. 4502443 [121], aragonite n. 2100187 [122], hydroxyapatite (HA) n. 4317043 [170], brushite n. 1533075 [171] and ammonium phosphate dibasic n. 9011121 [172]. QualX was used with the database PDF2-2004, which allowed to recognize the peaks corresponding to ammonium calcium phosphate hydrate, $NH_4CaPO_4{*}H_2O$ (JCPDS cards 00-200-202).

Some of the as-synthesized powders were also characterized by FT-IR, ICP/OES and SEM. Infrared spectra were collected in transmission mode with a FTIR Thermo Optics Avatar 330, using KBr pellets, over the 4000–400 cm−1 range. The content of the carbonate substitutions into the apatite structure was estimated with a method proposed by Grunenwald et al. [173], by the equation

$$W_{CO_3} = 28.62\, r_{c/p} + 0.0843 \qquad (4)$$

where $r_{c/p}$ is the ratio of the area below the carbonate peaks (1330-1530 cm^{-1}) and the phosphate peaks (1230-900 cm^{-1}).

ICP/OES was used to estimate the Ca/P ratio with a Spectro Ciros Vision CCD (125–770 nm), using hydroxyapatite ultrapure standard (>99.995% trace metal basis, Sigma–Aldrich). The samples were solubilized in ultrapure nitric acid (70 vol%, Sigma–Aldrich) and diluted with pure water (obtained by reverse osmosis, σ < 0.1 μS cm-1). The emission lines chosen for the analysis were 184 nm for Ca and 178 nm for P. A FE-SEM SUPRA 40 (Carl Zeiss Microscopy GmbH) instrument was used to analyze the morphology of the powders. Finally, the specific

surface area (SSA) of the powders was measured with an ASAP 2010 Micromeritics apparatus, using the B.E.T. theory [174] on the adsorption of N_2 at -196°C.

3.3 Results and discussion

3.3.1 Synthesis of HA: analysis of the influence of the process parameters

The phase composition of powders dried at different temperatures, from room temperature to 150°C, are shown in Figure 3-1 and Figure 3-2. These results suggest that the temperature at which the slurries are dried after ball-milling has a significant influence on the synthesis efficiency. Figure 3-1 shows the diffraction patterns of eggshell powder ball-milled in basic (Figure 3-1a) and acidic (Figure 3-1b) solutions and dried at different temperatures. In both cases, ES-calcite converted into HA only when the slurry was dried in the oven, while, at room temperature, two different intermediate phases appeared instead. These other intermediate phases are brushite ($CaHPO_4*2(H_2O)$, ICDD card n. 00-009-0077) for the process carried on with H_3PO_4, and ammonium calcium phosphate monohydrate ($NH_4CaPO_4*H_2O$, ICDD card n. 00-020-0202) for the reaction with ammonium phosphate dibasic and NH_4OH. When, instead, the slurries were dried in the oven, the formation of HA was promoted. The higher the temperature, the more the reaction was favored, as indicated by the peaks corresponding to the unreacted calcite becoming smaller when the temperature increases from 90°C to 150°C.

Similar observations can be performed for MS- and CB-derived powders (Figure 3-2). After drying the ball-milled MS slurry at room temperature (Figure 3-2b), brushite is formed but, when heating at 100°C, HA is visible, as well as some residual calcite. This residual calcite is completely missing after drying at 120°C, which makes the transformation into HA complete. Slightly different is instead the behavior of the CB powder, as no intermediate phase appears at room temperature. In this case, the XRD spectrum reveals aragonite and unreacted ammonium phosphate dibasic, together with an incipient formation of HA (Figure 3-2a). The conversion of CB-aragonite into HA is instead almost complete when drying the slurry at 100°C (a small aragonite peak is still visible), and complete at 120°C.

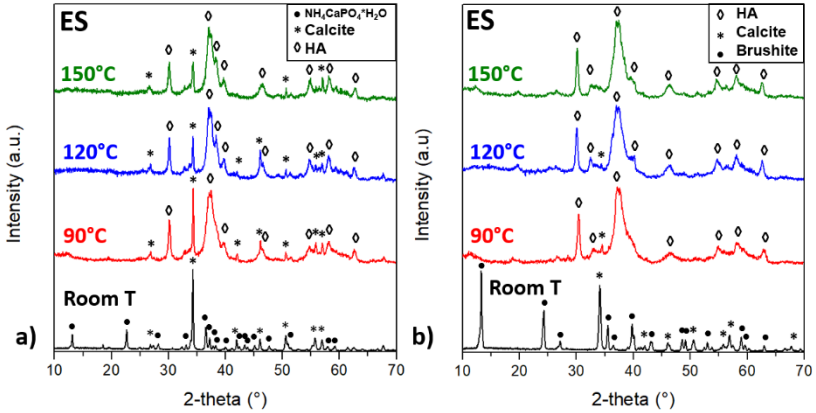

Figure 3-1 XRD spectra of eggshell powder milled for 4 h and dried and different temperatures. Synthesis in basic solution, initial pH = 13 (a) and synthesis in acidic solution, initial pH = 3.2 (b).

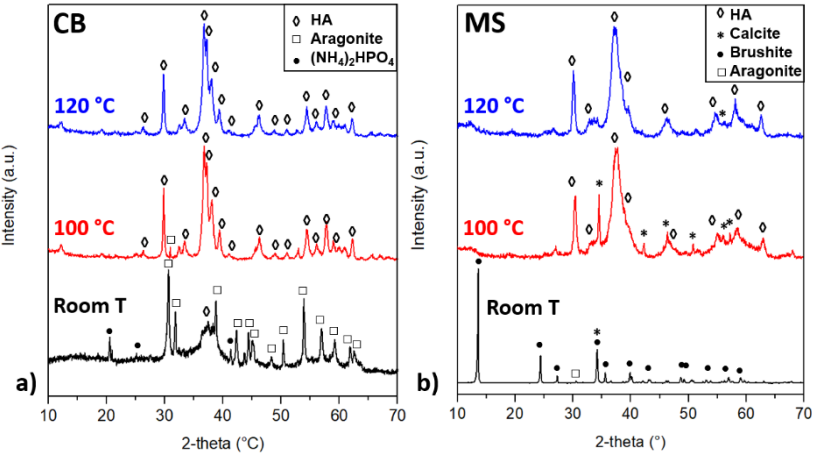

Figure 3-2 XRD spectra of cuttlebone powder (a) and mussel shell powder (b) milled for 4 h and dried at different temperatures. Synthesis performed at initial pH = 8.5 (a) and at initial pH = 3.2 (b).

This may suggest that the path for the conversion of the two calcium carbonate polymorphs into HA is different: calcite passes through an intermediate phase, which can be, depending on the pH, brushite or

$NH_4CaPO_4*H_2O$, while aragonite transforms directly into HA. In fact, only in the case of CB some unreacted phosphate is present after drying at room temperature, while the other two biogenic powders behave differently. First, they transform partially into an intermediate with Ca/P ratio 1:1 and then, with heating, the residual calcite reacts with the intermediate phase and forms HA, which is richer in calcium, with Ca/P ratio = 5:3.

The strong influence of the drying temperature on the synthesis process is quite interesting and rather surprising. In fact, initially the slurry was dried at about 100°C just to remove the water, without considering it as an important variable. This was because, as suggested in the work by Ferro and Guedes [117], the main parameter affecting the mechanosynthesis process was thought to be the milling time, i.e. the amount of mechanical energy. However, in the present study, the milling time appears to not have much influence of the process.

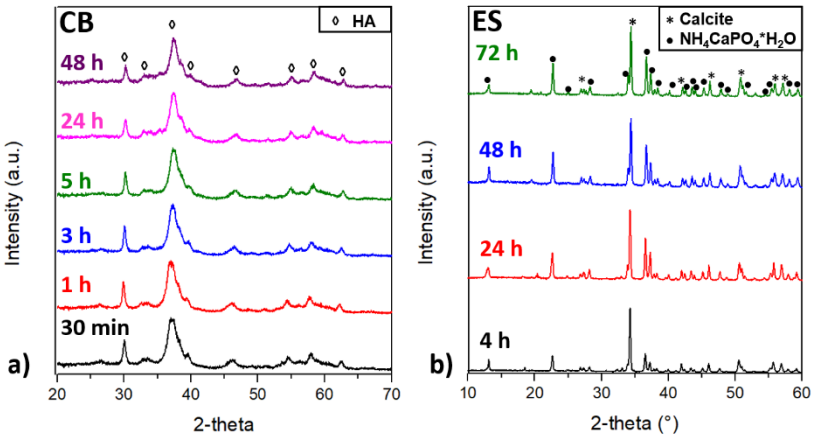

Figure 3-3 XRD spectra of powders ball-milled for different times. Cuttlebone powder milled at initial pH = 8.5 and dried at 120°C (a) and eggshell powder milled at initial pH = 13 and dried at room temperature.

This is clear when looking at the XRD spectra of cuttlebone and eggshell powders ball-milled for different times (Figure 3-3). The two powders were treated with different synthesis conditions: CB was ball-milled at initial pH = 8.5 and dried at 120°C while ES at initial pH = 13 and dried at room temperature. In both cases, the spectra of the powders ball-

milled for different times appear almost identical. In the case of ES, dried at room temperature, no HA is formed even after 72 h of milling (Figure 3-3b); in the case of CB, dried at 120°C, the transformation into HA is complete already after 30 min and no changes are observable up to 48 h of milling (Figure 3-3a).

It is believed that, for some reasons, in these experiments the mechanical energy alone was not sufficient to promote the reaction of hydroxyapatite formation. The heat used for drying the slurry, instead, supplied the required energy more efficiently with respect to the mechanical energy provided by milling. However, there are many other factors that could have influenced the reaction, such as the solid content of the slurries, the quantity of processed powder per batch (vial filling), the diameter and material of the milling balls, the ball-to-powder ratio, the milling speed, etc. It is therefore possible that different results could have been obtained when changing these variables.

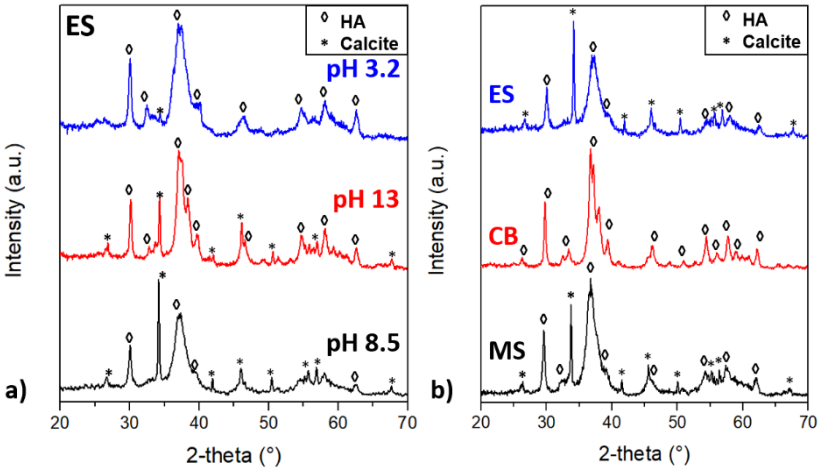

Figure 3-4 XRD spectra of eggshell powder processed at different initial pH (a) and of powders from different biogenic sources processed at initial pH = 8.5 (b). Milling time 4h, drying at 120°C for 24 h.

Figure 3-4a shows the diffraction patterns of eggshell powder processed at different initial pH, thus in slightly basic, basic or acidic milling media. It can be observed that the conversion of the ES-calcite into HA is complete only when the process is carried out with phosphoric acid, i.e.,

at initial pH = 3.2. When, instead, the process is performed using ammonium phosphate dibasic, some calcite remains unreacted. Similar observations can be done also by comparing Figure 3-1a and Figure 3-1b, which show the XRD spectra of ES powder synthesized at different temperatures in basic or acidic media, respectively. Therefore, the acidic solution favors the reaction, most likely because it promotes the dissolution of $CaCO_3$.

The difference between the behavior of the three biogenic sources can be further understood by looking at Figure 3-4b, which shows the spectra of ES, CB and MS powders processed with the same conditions (pH = 8.5, milling time 4 h, drying temperature 120°C). It can be seen that CB-aragonite converts completely into HA, while the transformation is only partial for MS and ES. As mentioned in paragraph 1.7, aragonite is slightly less stable than calcite [124,175] and therefore it is possible that it transforms more easily into HA, most probably requiring less energy with respect to calcite. This is in agreement with the literature [117] and it may explain why CB, which is composed of 100% aragonite, completely transforms into HA, while ES, consisting of pure calcite, has the largest amount of residual calcite. Some unreacted calcite is revealed also in the XRD pattern of MS; which is a mixture calcite/aragonite. Anyway, it can be observed that no residual aragonite is present, neither in CB nor in MS, which again confirms the idea that aragonite transforms easier into HA, most probably also following a different path.

3.3.2 Bio-derived apatites characterization

In the previous paragraph, the wide width of the peaks of the XRD spectra indicates that the crystals are nanosized. This is confirmed by the Rietveld analyses, which allowed to calculate crystallite sizes of 13 nm (ES and MS) and 25 nm (CB). Moreover, all the synthesized apatites show a preferential growth along the c-axis, which is revealed by the high relative intensity of the (002) peak at about 30° with respect to the (211) one at 37° (Figure 3-4) [176].

Figure 3-5 shows the FT-IR spectra of HA powders produced from the three different biogenic sources. The analyses show that, in all cases, we deal with carbonated hydroxyapatite. Carbonate substitutions correspond to the peaks at about 875 cm^{-1} for the $\nu_2(CO_3)$ vibration mode and between 1400 and 1500 cm^{-1} for the $\nu_3(CO_3)$ vibration mode. These substitutions are A-type, B-type and labile (meaning in a not crystallized

region), thus resulting in carbonated AB-type apatite. In fact, the A-type substitution typically give rise to a peak at about 1545 cm^{-1}, while labile CO_3^{2-} to peaks at 1416-19 cm^{-1} [173,177]. The B-type substitution, instead, is revealed by the peak centered at 874 cm^{-1}, that has two contributions (zoom in Figure 3-5c): A-type at 878 cm^{-1} and B-type at 872 cm^{-1} [177]. However, there could be also a contribution of HPO_4^{2-} that has a characteristic peak at 875 cm^{-1} [173]. The phosphate groups are revealed by the peaks at 563-602 cm^{-1} ($\nu_4(PO_4)$), at 960 cm^{-1} ($\nu_1(PO_4)$), at 1032 ($\nu_3(PO_4)$) and by the shoulder at 1100 cm^{-1} ($\nu_3(PO_4)$) [178,179]. Moreover, structural OH groups correspond to the peaks at 1635-1647 cm^{-1}, while the sharp peak at 1385 cm^{-1} might be associated to the presence of NO_3^{2-} [177,180].

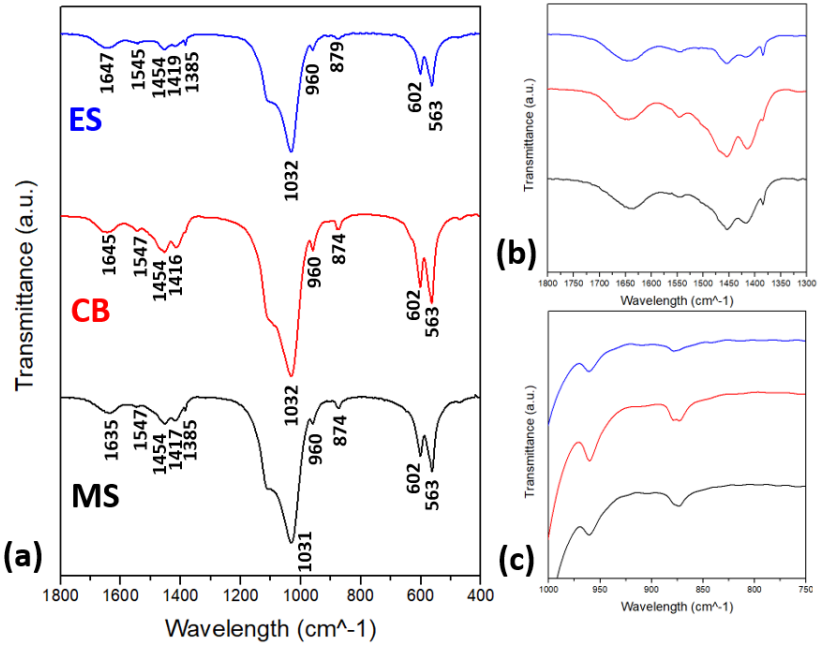

Figure 3-5 FTIR spectra of HA powders produced from ES, CB and MS (a); zoom on the $\nu_3(CO_3)$ band (b) and zoom on the $\nu_2(CO_3)$ (c). ES and MS: 4 h milling with H_3PO_4 and drying at 150 °C; CB: 4 h milling with $(NH_4)_2HPO_4$ and drying at 120 °C.

The total amount of carbonate substitutions was evaluated by comparing the area below the carbonate peaks (1330-1530 cm^{-1}) and

the phosphate ones (1230-900 cm^{-1}). The weight content of CO_3^{2-} is therefore equal to 4.0% for ES, 4.9% for MS and 6.0% for CB. These quantities are comparable with the composition of natural bone, which, as previously showed in Table 1-3, contains about 4–6 wt% of carbonate ions.

Table 3-1 shows the results of the ICP/OES analyses. The content of Ca and P yields to Ca/P ratios lower than 1.67 for the apatites synthesized from CB and ES, meaning that they are calcium deficient HAs (CDHA). The powder synthesized from MS, instead, is characterized by a Ca/P ratio larger than 1.67. Anyway, all of them are non-stoichiometric, like the bone mineral (see paragraph 1.5). The ICP/OES analyses also detected the presence of impurities, as a consequence of the natural origin of the powders. In fact, traces of Na, Mg and Sr are present in all apatites, while K only in CB and ES. Similarly to the original biogenic calcium carbonates (see Chapter 2), Mg is present mainly in the apatite derived from ES (~0.3%) and Sr in the one from CB (~0.2%). Moreover, other impurities in very small quantities (<50 ppm) were also detected, like Cl in CB, Ba in CB and ES, Zn in CB, and Fe, Si, and Mn in MS.

Table 3-1 Ca/P molar ratio and content of Na, K, Mg, and Sr of apatites synthesized from different natural sources (measurements by ICP/OES)

Biogenic source	Ca/P molar ratio	Na	K	Mg	Sr
MS	1.76 ± 0.02	0.3 wt%	-	0.1 wt%	0.1 wt%
CB	1.64 ± 0.02	0.9 wt%	0.1 wt%	0.1 wt%	0.2 wt%
ES	1.58 ± 0.02	0.1 wt%	0.1 wt%	0.3 wt%	< 0.1 wt%

The morphology of the HA crystals is shown in the FESEM pictures in Figure 3-6. The thickness of the crystals is about 20 nm, while the length is in the order of hundreds of nanometers. It can also be noticed that the crystals have a plate-like shape, also known as leaf or flake shape [181]. These HA crystals are aggregated in particles, with dimensions ranging

from few micrometers to about 300 µm. The specific surface area (SSA) of the powders was measured to be 47 m^2/g for CB-HA, 124 m^2/g for ES-HA and 94 m^2/g for MS-HA. These high values highlight the nanometric dimensions of the powders, resulting in mean sizes of 15-40 nm, if considering spherical particles.

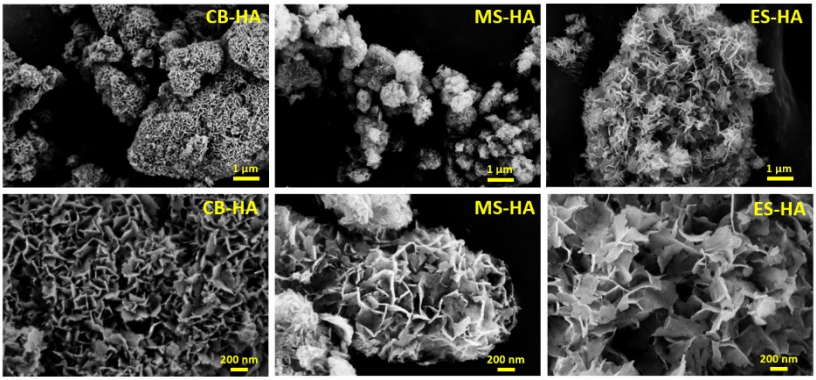

Figure 3-6 FESEM micrographs of the HA crystals obtained from CB, MS and ES. Milling time 4 h. Drying temperature 120 °C (CB, MS) and 150°C (ES); initial pH = 8.5 (CB, MS) and 3.2 (ES).

3.4 Conclusions

The study about the synthesis of HA starting from eggshells, mussel shells and cuttlebones is summarized in the simple scheme shown in Figure 3-7.

ES- and MS-calcite passes through an intermediate phase, that depends on the pH, while CB- and MS-aragonite convert directly into HA. Moreover, the reaction seem to require less energy for aragonite with respect to calcite, and for acidic milling media with respect to basic ones. This energy is better supplied by the temperature chosen to dry the slurry rather than the mechanical energy of milling.

The synthesized powders are non-stoichiometric apatites, characterized by AB-type carbonate substitutions and by the presence of many impurities, such as Mg^{2+} and Sr^{2+}. The crystals, which have nanometric dimensions and a flake-like shape, are aggregated in particles of 1-300 µm size.

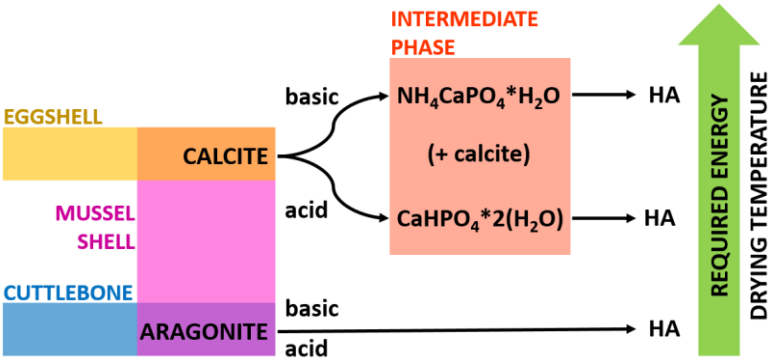

Figure 3-7 Scheme of the transformation paths of the three biogenic calcium carbonate sources into HA.

Chapter 4

Sintering and preliminary biological evaluation

4.1 Introduction

This chapter deals with the consolidation of the bio-derived HA powders by uniaxial pressing and sintering, to produce bioceramics pellets. In addition, potential cytotoxicity effects of the sintered pellets on human osteosarcoma cells were tested *in vitro,* as well as the initial cell adhesion on the materials. Part of the content of this chapter has been already published in [182].

4.2 Methods

4.2.1 Sintered pellets production and characterization

Bio-derived HA powders were produced as described in Chapter 3. The synthesis parameters were different for the different biogenic sources (CB, MS and ES), in order to obtain 100% HA. These parameters were: milling time 4 h (ES, MS) or 30 min (CB); initial pH 8.5 (CB, MS) or 3.2 (ES); drying temperature 150°C (MS, ES) or 120°C (CB). A synthetic pure stoichiometric HA (sHA) was also used for comparison. The HA granules, size 5-25 μm, were purchased from S.A.I. (Science Application Industry, France).

About 0.1 g of each powder was pressed with 2 tons in a 5 mm diameter cylindrical die, with a manual hydraulic press (Specac). The green bodies were heated at 10°C/min in a muffle furnace (Nabertherm P330), with 2 h dwell time and free cooling in the oven.

After preliminary dilatometric analyses on the green pellets, the sintering temperature was chosen for each powder, in order to obtain densification while maintaining some porosity. Therefore, the sintering temperature was 900°C for ES-HA, 1000°C for MS-HA and 1100°C for sHA. Two temperatures were instead selected for CB-HA, 900°C and 1100°C. The sintered samples are named after the raw material and the

sintering temperature, as sHA-1100, ES-900, MS-1000, CB-900 and CB-1100.

In order to determine the phase composition, the sintered pellets were crushed into powders with a manual mortar and then analyzed by XRD. The diffractometer used was a Rigaku IIID-max, Cu anode source (Kα radiation 1.5406 Å), step time 2 s, scan step 0.05° and 2-theta range 5° – 110°. The qualitative and quantitative analysis was carried on with the software Maud [159], using these phases from the COD database [160]: HA n. 4317043 [170], β-TCP n. 1517238 [183], $Ca(OH)_2$ n. 1000045 [184] and CaO n. 9006712 [185].

A JEOL JSM-5500 scanning electron microscope (SEM) was used to observe the surface morphology and the internal porosity of the pellets, using secondary electrons and Pt/Pd metallization. The density of the sintered pellets was measured with a laboratory scale and a caliper, considering 5 samples per type.

4.2.2 Biological *in vitro* tests

The potential cytotoxicity of the sintered pellets was evaluated with a LDH cytotoxic assay (ThermoFisher Scientific), which measures the amount of lactate dehydrogenase (LDH), that is released by the cells during death. The test was carried on following the European Standard EN ISO-10993-12:2004 and 10993-5:2009. Fibroblasts cell line (MRC5) were used for the test, after expansion and culture under standard conditions (37°C and 5% CO_2), in a medium of composition: minimal essential medium (MEM-Gibco), 10% inactivated fetal bovine serum (Euroclone), 1% L-glutamine (Euroclone), 1% sodium pyruvate (Gibco), 1% non-essential amino acids (SigmaAldrich), and 1% antibiotic-antimycotic (Euroclone).

The samples were sterilized in autoclave and then incubated for 72 h in a medium with heat inactivated serum and without phenol red. After the incubation, the conditioned medium was poured on MRC5 cells, which were previously seeded in a 96-well plate (5000 cell/well) and incubated for 48 h. Cells cultured in standard medium and fully lysate cells represented the positive and negative controls, respectively. The LDH released in the medium was quantified using a Tecan Infinite 200 microplate reader (Tecan Group, Männedorf, Switzerland), recording

the background at 680 nm and the absorbance at 490 nm. Each test condition was tested for five replicates.

A confocal microscope Nikon A1 Laser was used to observe the adhesion of human osteosarcoma cell line (MG63) on the sintered samples. 6000 cells/well were seeded on the sintered pellets in a 96-well culture plate and then the cells were cultured in standard conditions in a culture media of the same composition as in the LDH test, but, this time, with activated fetal bovine serum.

The cells adhered to the scaffolds were observed after 1, 3, and 5 days. In order to stain the cells to be seen at the microscope, at each time point 4% paraformaldehyde was used to fix the samples for 40 min, then cell membranes were permeabilized with 0.2% Triton X-100 and 4, 6 diamidino 2 phenylindole, dilactate (DAPI-SigmaAlrich) and I-Fluor 488 (Abcam) were used to stain the cellular nuclei and cytoskeleton, respectively.

4.3 Results

4.3.1 Sintered pellets characterization

The diffraction patterns of the sintered pellets are shown in Figure 4-1 and the relative crystallographic phase composition, as determined by the Rietveld analysis, is shown in Table 4-1.

First, it can be observed that the XRD spectra of the sintered pellets show sharper peaks with respect to the synthesized powders (Chapter 3), since the crystallites have grown during sintering, from few nanometers to micrometric dimensions (> 200 nm). Moreover, in the case of MS-1000 and CB-900, where the hexagonal HA structure is maintained, the preferred orientation along the c-axis that characterized the synthesized powders ((002)/(211) peaks relative height) is much less or even not visible anymore. Phase changes instead occurs in ES-900 and CB-1100, where β-TCP forms during the sintering process.

The phase composition of the sintered pellets can be discussed considering the CaO/P_2O_5 phase diagram (Figure 1-4) and the Ca/P molar ratio of the powders, which is reported for convenience in Table 4-1.

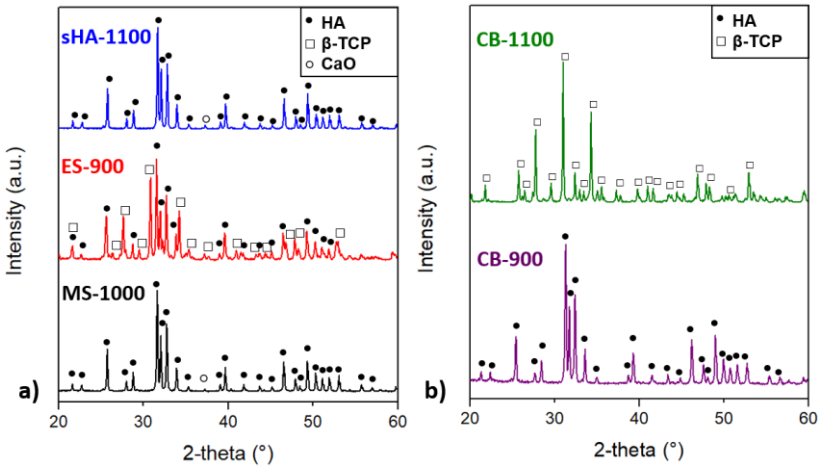

Figure 4-1 XRD spectra of the sintered pellets: synthetic HA (sHA) sintered at 1100°C, ES-HA sintered at 900°C and MS-HA sintered at 1000°C (a); CB-HA sintered at 900°C and 1100°C (b).

Table 4-1 Phase composition (wt%) of the sintered pellets, as determined by the Rietveld analysis. The Ca/P molar ratios were measured by ICP/OES (see Chapter 3).

Material	Sintering temperature	Ca/P molar ratio	Phase Composition
sHA	1100°C	1.71 ± 0.02	HA, <3% CaO
ES-HA	900°C	1.58 ± 0.02	∽50% HA, ∽50% β-TCP
MS-HA	1000°C	1.76 ± 0.02	HA, <3% CaO
CB-HA	1100°C	1.64 ± 0.02	∽ 90% β-TCP, ∽5% HA, ∽5% $Ca(OH)_2$
CB-HA	900°C	1.64 ± 0.02	100% HA

According to the phase diagram, Ca/P=1.67 results in 100% HA, while Ca/P=1.5 corresponds to pure β-TCP. When, instead, the Ca/P ratio is between these two values, both HA and β-TCP should form, following the lever rule. This is the case of ES-HA, which has a Ca/P ratio equal to 1.58 and thus transforms into 50/50 biphasic HA/β-TCP when sintered at 900°C (ES-900).

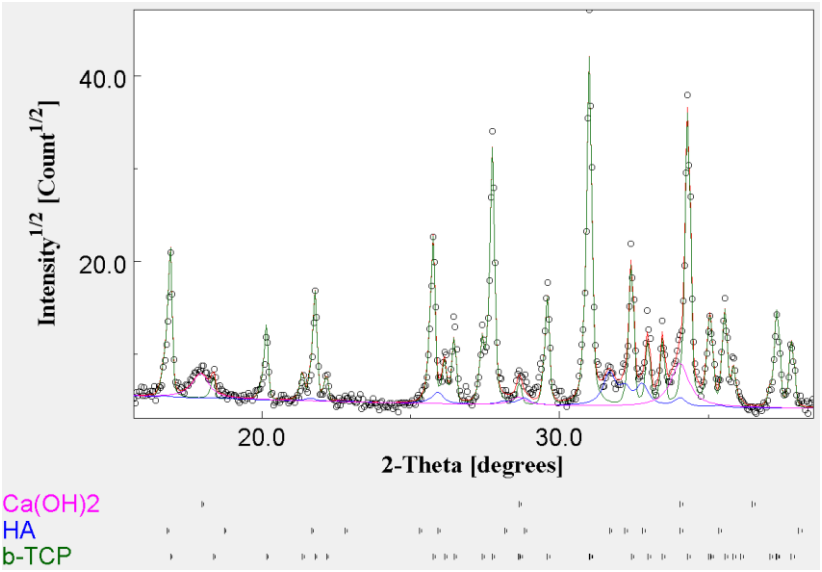

Figure 4-2 Detail of the Maud analysis of CB-1100: the contribution of HA and calcium hydroxide are visible. Refinement goodness parameters: Sig = 1.38 and Rwp(%) = 17.1.

Different was instead the behavior of the cuttlebone-derived apatite (CB-HA), which has Ca/P = 1.64, close to stoichiometric proportions. After sintering at 900°C (CB-900), it maintains the hexagonal HA structure, but, when heat treated at 1100°C (CB-1100), it transforms into ∽90% β-TCP, ∽5% HA and ∽5% $Ca(OH)_2$. Since the presence of apatite and calcium hydroxide is not visible in the XRD spectrum showed in Figure 4-1, a detail of the fitting from the Rietveld software Maud is reported in Figure 4-2. Here, the contribution of HA is visible from the small peak at 32°, while that of $Ca(OH)_2$ from the peak at 18° and the shoulder at 34°. The composition of CB-1100 is quite surprising because, according to the phase diagram, ∽85% HA and ∽15% β-TCP are expected with Ca/P =

1.64. It seems, instead, that the excess of calcium due to the predominance of β-TCP results in the formation of $Ca(OH)_2$.

The reason for behaviors that deviate from what it is expected by the phase diagram may be linked to the impurities that are present in the considered natural materials. In particular, bivalent cations like Sr^{2+} and Mg^{2+} are known to stabilize the crystal structure of β-TCP, at the expense of HA [186–188]. It is therefore possible that the strontium content in CB-HA leads to the formation of β-TCP, but the reason for the presence of $Ca(OH)_2$ is unclear. One possibility is that Ca^{2+} and PO_4^{3-} are not homogeneously distributed in the powders, this determining some areas were the Ca/P ratio is higher than 1.67 and therefore where calcium hydroxide can be formed.

Another observation regards ES-HA and CB-HA, both with Ca/P < 1.67, which behave differently when sintered at 900 °C. In fact, while ES-HA transforms into HA and β-TCP, CB-HA does not, maintaining the apatite structure. This can be due to the presence of Mg^{2+} ions in ES-HA, since magnesium was proven to lower the temperature at which CDHA transforms into a biphasic mixture of β-TCP and HA [189].

When the Ca/P ratio is larger than 1.67, the phases predicted by the phase diagram are CaO and HA. This the case of MS-1100 and sHA-1100, that have Ca/P equal to 1.76 and 1.71, respectively. In agreement with this, the XRD analyses revealed that the sintered pellets are composed of mainly HA, with small amounts of CaO (< 3%).

The SEM micrographs of the fracture and external surfaces of the pellets are shown in Figure 4-3 and Figure 4-4. All samples present well-developed necks between particles and some porosity, this indicating that densification is not complete, as confirmed also by the density measurements shown in Figure 4-5. Most of the pores are very small, having dimensions of about 1 μm or less. This type of porosity most probably is not perceived as holes by the cells, that have dimensions of about 100 μm, but the presence of these micropores is still thought to be beneficial for the material-cells interaction, as well as being useful for the passage of liquids and molecules [21].

As expected, CB-1100 and sHA-1100, that are sintered at the highest temperature, reached the highest densification, with relative density 91% and 89%, respectively. However, the CB-1100 grains appear bigger

than those of sHA-1100, probably due to the recrystallization that occurred in CB-1100 during sintering, from CDHA to β-TCP. In sHA-1100, instead, the original grains grow without recrystallization, and therefore reach smaller dimensions. MS-1000, CB-900 and ES-900, instead, reached similar densities, around 70% of relative density.

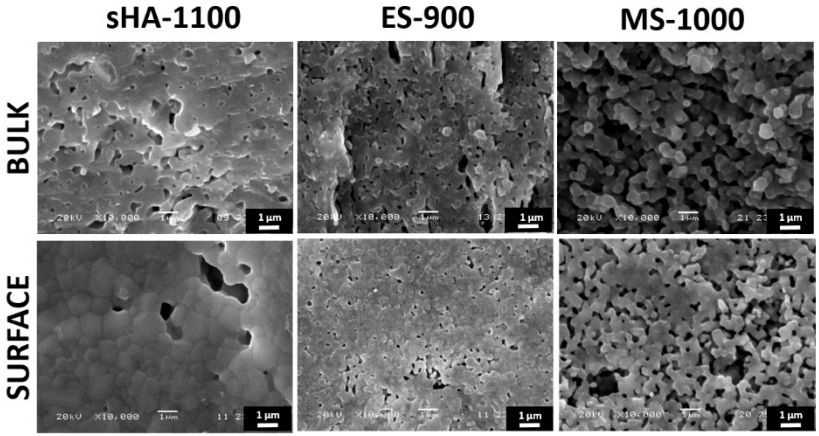

Figure 4-3 SEM micrographs of the fracture surface (bulk) and the external surface of sHA-1100, ES-900 and MS-1000.

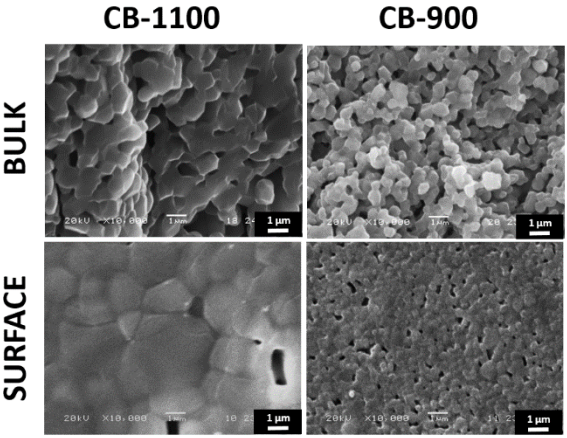

Figure 4-4 SEM micrographs of the fracture surface (bulk) and the external surface of CB-1100 and CB-900.

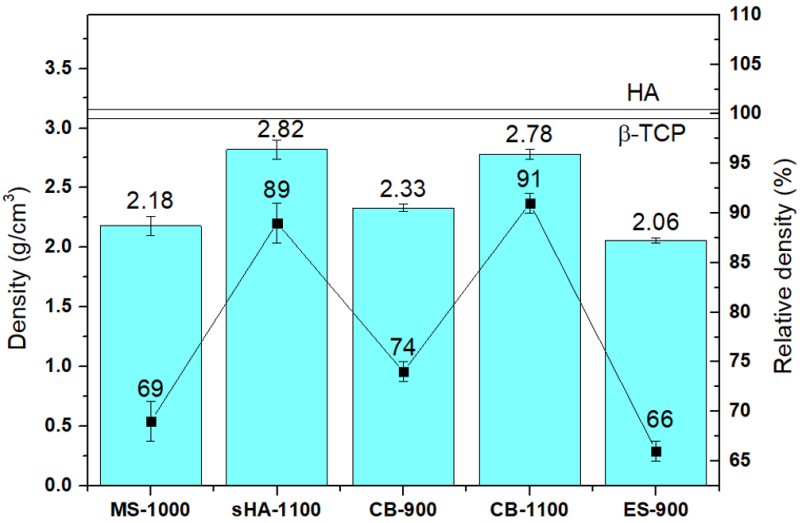

Figure 4-5 Bulk density of the sintered pellets, compared with the theoretical densities of HA and β-TCP. The relative density is calculated from the phase composition estimated by XRD.

4.3.2 Preliminary biological evaluation

The LDH amount released by the cells in a medium previously conditioned with a biomaterial is a method to evaluate potential cytotoxic effects of the material. The European standards EN ISO-10993-12:2004 and 10993-5:2009 consider cytotoxic those materials that induce a LDH release equal or superior to 30%, where the percentage is calculated based on the negative control, i.e. all dead cells. The results of the LDH assay of the sintered pellets is shown in Figure 4-6. All samples induced a LDH release below 8%, therefore much less than the cytotoxicity threshold, and very close to the positive control (cells cultured in standard medium), which is 8.3%.

Given that the sintered pellets are not cytotoxic, confocal microscopy was performed after 1, 3 and 5 days of culture in order to observe the adhesion and growth of MG63 osteosarcoma cells on the pellets. The confocal images are shown in Figure 4-7. At day 1, all samples are covered by round shape cells, ES-900 and CB-900 showing the highest number of cells, while MS-1000 and CB-1100 the lowest. At day 3, the

cell number significantly improves on sHA-1100 and ES-900, while the growth on CB-900 and CB-1100 is lower. In addition, the cells on sHA-1100 appear aggregated in clusters, while on the other samples they look homogenously distributed on the surface. Curiously, the cells on MS-1000 does not seem to be any different from day 1, being still in small numbers. However, at day 5, good cell adhesion and proliferation is observed on all samples, also on MS-1100. The cells have an elongated shape and are interconnected between each other on all the sintered pellets, with the exception of CB-900, where they appear still rounded and not interconnected. On sHA-1100, cell clusters are still present in certain areas of the surface.

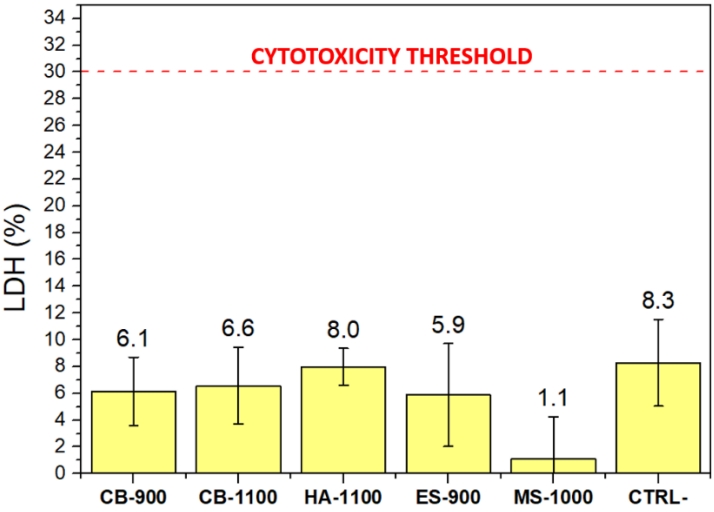

Figure 4-6 LDH released by the dead cells in a medium conditioned with the sintered pellets. All data were normalized on the positive control (100%, all dead).

It is difficult to correlate these results with the phase composition of the sintered pellets, since samples with the same composition show different behavior. For example, MS-1100 and CB-900 are both composed of mainly HA, but they show opposite behaviors: the cells on MS-1100 grow slowly in the first 3 days but form a well-interconnected network of elongated cells at day 5; cells on CB-900, instead, grow fast in the first days but remain rounded and not interconnected even at day 5.

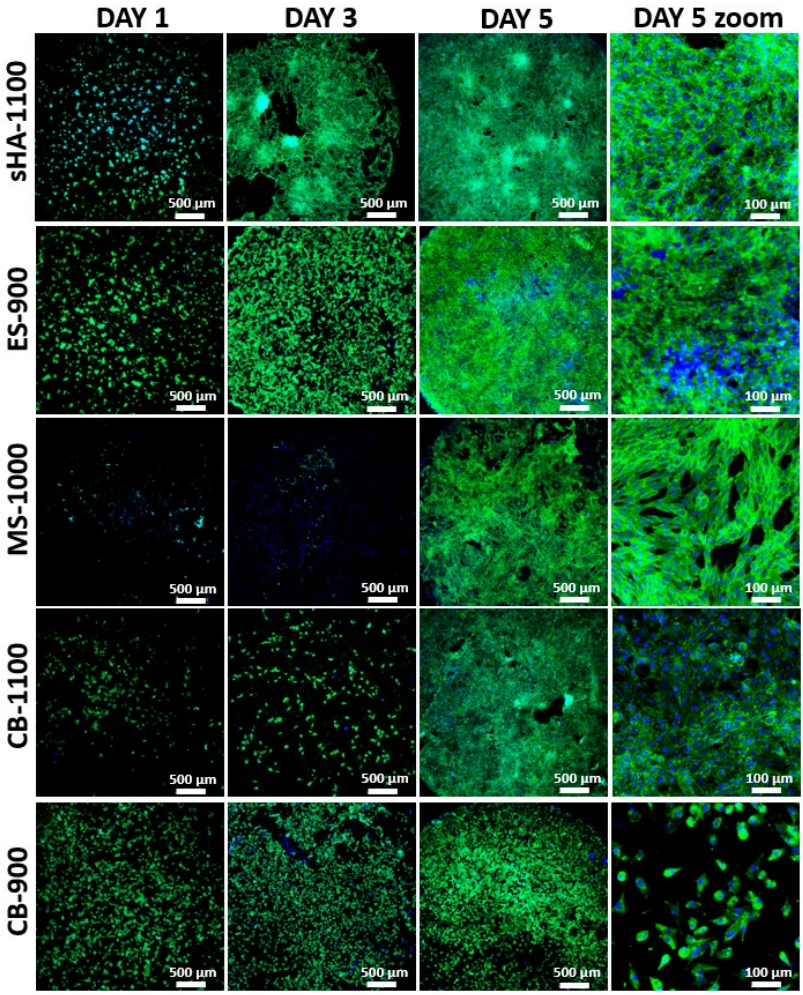

Figure 4-7 Confocal images of cells adhered on the sintered pellets after 1, 3 and 5 days of culture (day 5 is shown also with zoomed images). Cytoskeleton is highlighted in green and cell nuclei in blue.

It might be said that the best bioactivity was shown by ES-900, where the cells grow fast and, at day, 5, cover the entire surface with a dense cell network. However, this is hard to be correlated with the phase

composition, that in this case is 50/50 HA/β-TCP. One possible explanation is that the eggshell-derived HA contains the highest concentration of magnesium, which was found to promote the adhesion and spreading of osteosarcoma cells [52,190]. However, this is just an hypothesis that would need additional experiments to be confirmed.

Nevertheless, the purpose of this preliminary biological test was only to have a general idea of the interaction between osteoblasts and the sintered pellets made of bio-derived HA. The adhesion and proliferation of the cells on the bio-derived materials are generally good and comparable with synthetic HA. The main difference, that can be observed here, between synthetic HA and bio-derived calcium phosphates, is the formation of cell clusters on synthetic HA, which is not visible on the bio-derived materials.

4.4 Conclusions

The diffraction patterns of the sintered bio-derived HAs revealed that crystallites grow during sintering, from nanometric to micrometric dimensions, and that the preferential growth along the c-axis disappears. The phase composition was found to be dependent from the Ca/P ratio of the powders, as expected by the phase diagram: Ca/P > 1.67 results in HA and CaO (MS-1000 and sHA-1100) while Ca/P < 1.67 leads to the formation of biphasic HA/β-TCP (ES-900). However, the composition of cuttlebone-derived HA (Ca/P = 1.64) was found to depend on the heat treatment, since the apatite structure is maintained at 900°C, but mainly β-TCP is formed at 1100°C. Deviations from the phase diagram are thought to be related to the presence of impurities ions, such as Mg^{2+} and Sr^{2+}, or to a non-homogenous distribution of calcium and phosphorus in the material. All the sintered pellets showed some residual microporosity, from about 10% in the materials sintered at 1100°C to about 30% in the ones sintered at lower temperatures.

The preliminary biological tests showed that all materials are not cytotoxic and promote good adhesion and proliferation of MG63 osteosarcoma cell line after 5 days of culture, similarly to synthetic HA but without the formation of clusters. The cell proliferation rate, shape and distribution were found to be different on the different materials, although the reasons for this are not clear. Among the bio-derived materials, ES-900 promoted the best adhesion and proliferation of cells.

Chapter 5

Extrusion 3D printing of biocomposite scaffolds

5.1 Introduction

This chapter is about the production of biocomposite scaffolds by extrusion 3D printing, also called FDM (Fused Deposition Modeling). About 15 wt% of HA nanopowders derived from cuttlebones, mussel shells and eggshells, synthesized as described in Chapter 3, were dispersed in PCL, to obtain bioactive composites. The scaffolds were characterized in terms of mechanical properties and of biological behavior *in vitro*. This study was carried out in collaboration with the RAMSES laboratory of the Rizzoli Orthopedic Institute (Bologna), that holds the printing machine. Part of the content of this chapter has been already published in [191].

5.2 Methods

5.2.1 Composite materials fabrication and characterization

The bio-derived HA powders were synthesized as described in Chapter 3, using different process parameters for different biogenic sources, as listed in Table 5-1.

Table 5-1 Parameters used to synthesized the bio-HA powders used in this study

Raw material	Initial pH	Milling time	Drying temperature
CB	8.5	30 min	120°C
ES	3.2	4 h	150°C
MS	3.2	4 h	150°C

The PCL, with the commercial name of Facilan™ Ortho (MW ∽ 50,000), was purchased from 3D4MAKERS in the form of a 1.75 mm-diameter filament. The filament was chopped into 15-20 mm long portions to be

dissolved in chloroform. In order to make the composite material, 1.5 g of bio-derived HA was dispersed in 100 ml of chloroform (Sigma, CAS Number 67-66-3) and then 8.5 g of PCL were added while continuously stirring. After the complete dissolution of the polymer, the solution was poured on a flat glass, where it was left to let the chloroform evaporate. The composite sheet was then cut into pieces of about 5 x 5 mm^2. Three different composites were produced following this procedure: with CB-HA, with MS-HA and with ES-HA. In addition, pure PCL sheets without HA particles were also fabricated in the same way.

The real bio-HA content in each composite, that is expected to be 15 wt%, was determined by TGA/DTA, using a NETZSCH Geraetebau GmbH STA 409 thermobalance, heating the alumina crucibles at 10°C/min up to 600°C in flowing air. The melting temperature and enthalpy were instead determined by differential scanning calorimetry (DSC), with a Mettler® DSC30 instrument, aluminium pans, flowing nitrogen and temperature range -80°C to 120°C (10°C/min). The crystallinity was calculated using the following equation, which takes into account the bio-HA content measured by TGA:

$$\chi_c = \left(\frac{\Delta H_m}{\Delta H_m^0 \left(1 - \frac{\%wt_{HA}}{100}\right)} \right) \quad (5)$$

where ΔH_m and ΔH_m^0 are the melting enthalpy of the sample and of the pure crystalline PCL (142.0 J/g), respectively, and $\%wt_{HA}$ is the weight content of bio-HA powder in the composite [192]. Moreover, all materials were characterized by XRD, using a Rigaku IIID-max diffractometer working with Cu Kα radiation (1.5406 Å), step time = 2 s, scan step = 0.04° and 2-theta range = 10° – 70°.

5.2.2 Scaffolds fabrication and characterization

The scaffolds were designed and fabricated with a 3DDiscovery™ Evolution printer (RegenHU Ltd., Switzerland). They were designed with a square base of 5 x 5 mm^2 and a 0°/90° deposition pattern, with about 1 mm distance between parallel filaments (pore size 400 μm). The pieces of PCL/bio-HA were fed into a direct-dispenser heated extruder (DD-135), which was heated at the required temperature for 30 min before

printing, in order to have an homogenous melt. The temperature was adjusted for each material in order to optimize the flow: 90°C for pure PCL, 100°C for PCL/CB-HA, 110°C for PCL/ES-HA and 150°C for PCL/MS-HA. Then the material was extruded through a 600 μm nozzle, by the force of compressed air, with a pressure of 4 bar. The printing speed was set to 2.5 mm/s and the layer height to 200 μm. The height of the samples for the mechanical tests was 5 mm, while that of those for the biological assay 3 mm. Moreover, the samples for the biological *in vitro* tests were printed directly onto 6-well biological plates (SARSTEDT, 83.3920), performing the printing in a sterile environment, since the printer is equipped with a class II biosafety cabinet.

A scanning electron microscope JEOL JSM-5500 was used to investigate the morphology of the 3D printed scaffolds, after metallizing them with Pt/Pd with a QuorumQ150TES machine. The SEM images were also used to measure the dimensions of the strands and of the pores, by the software ImageJ. The scaffolds' base was instead measured with a calliper. The mechanical compression tests were carried out with an Instron® 5969 (Instron; Norwood, MA, USA) equipped with a 50 kN load cell. The strain was calculated based on the initial position of the crosshead, which was moved at 1 mm/min. Three scaffolds for each material were tested and the compressive modulus was calculated by linearly fitting the elastic part of the curves (R-Square ≈ 0.999) and making an average of the three. The yield stress was taken at 0.2%strain offset.

5.2.3 Biological *in vitro* tests

The biological tests were performed using human osteoblast cell line MG63. First, the cells were expanded onto culture flasks at 37°C in 5% CO_2 atmosphere in a medium composed of 87% MEM Gibco, 21090-022), 10% fetal bovine serum (EuroClone, ECS0180L), 1% sodium pyruvate (Gibco, 11360-039), 1% non-essential amino acids (Sigma-Aldrich, M7145), 1% L-glutamine (EuroClone, ECB3000D) and 1% of antibiotic/antimycotic (EuroClone, ECM0010D). When the cells covered ≈ 80% of the flask surface (confluence), they were detached with 0.1% trypsin and suspended in the culture medium at concentration 200000 cells/ml.

100 μl of cells suspension was put in each well of 48-well plates, were the scaffolds were previously placed. Then each well was covered by 200

µl of medium and, after 24 h of incubation, the scaffolds, seeded with cells, were moved into new 48-well plates with 300 µl of medium. This was done in order to culture only the cells that adhered on the scaffolds and not those that ended up on the bottom of the wells. The cell culture was carried out by changing the culture medium every second day. All analyses were done after 1, 3 and 7 days of culture.

For the confocal analysis, the samples were fixed with a 4% paraformaldehyde solution in PBS (phosphate buffer solution), while a Triton X-100 solution (0.2% in PBS) was used to permeabilized the cell membranes. Then, 0.02% Oregon Green Phalloidin was used to stain the cytoskeletons. The morphology of the adhered cells was then observed with a Nikon A1 confocal laser microscope (Nikon Instruments, Florence, Italy).

The metabolic activity was evaluated by Alamar Blue assay, considering five replicates for each sample. The scaffolds, seeded with cells, were incubated for 2 h at 37°C in 5% CO_2 atmosphere, after adding 300 µl/well of 10% Resazurin reagent. Then 100 µl/well of solution was measured with a Tecan Infinite 200 microplate reader (Tecan Group, Männedorf, Switzerland), which measured the fluorescence signal (excitation wavelength 535 nm and emission wavelength 590 nm).

The number of cells was measured by using a Quant-iT PicoGreen® dsDNA Assay (Invitrogen™, Carlsbad, USA). At each time point, 300 µl of 0.05% Triton-X in PBS was used to cover each scaffold, which were then stored at -20°C. For the analyses, the samples were then thawed at room temperature and sonicated for 10 s with a ultrasonic homogenizer (Hielscher Ultrasonics, Teltow, Germany). Then 100 µl of each sample was mixed with 100 µl of PicoGreen® solution and placed in a black 96-well plate. The same microplate reader used for the Alamar Blue assay was used to measure fluorescence, with excitation wavelength 485 nm and emission wavelength 535 nm. Four replicates were considered per each sample. The number of cells was calculated considering a conversion factor of 7.7 pg DNA per cell, where the DNA content was evaluated by performing a calibration using a DNA standard provided by the kit.

The Alamar Blue and PicoGreen® results were analysed using statistical analysis. Student's t-test was used to determine significant differences between samples' means, using Microsoft® Excel® 2016. Each pair of

samples was compared calculating the p-value with a two-tailed tests, assuming equal variances.

5.3 Results

5.3.1 Composite materials characterization

The thermogravimetric curves of pure PCL and of the composites PCL/bio-HA are shown in Figure 5-1. The ceramic filler content was evaluated based on the residual mass at 600°C, minus the residual mass of pure PCL. The results are listed in Table 5-2. For all the composite materials, the bio-HA content is less than the target 15%, most probably because the bio-derived powders contain humidity and a certain quantity of organics. This organic matter was present in the original biogenic calcium carbonates (see Chapter 2) and it was not eliminated during the synthesis process, that was carried out at relatively low temperature.

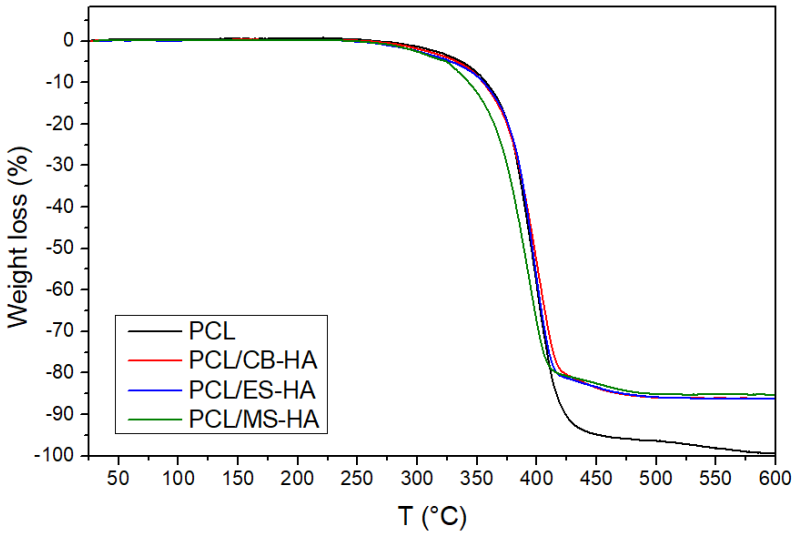

Figure 5-1 TGA curves of pure PCL and of the three composite materials.

In addition, the TGA analyses reveal that the materials start to degrade at about 250°C, which means that no deterioration is expected during the 3D printing process, where the materials are heated at 90-150°C. The

degradation onset temperature is around 365-370°C for PCL/ES-HA and PCL/CB-HA, while it was about 10°C lower for PCL/MS-HA.

Table 5-2 TGA data of pure PCL and of the PCL/bio-HA composites.

	PCL	PCL/CB-HA	PCL/ES-HA	PCL/MS-HA
Residual mass at 600°C	0.7%	13.9%	13.8%	14.8%
Bio-HA content	0%	13.2%	13.1%	14.1%
Onset temperature (°C)	367	366	369	356

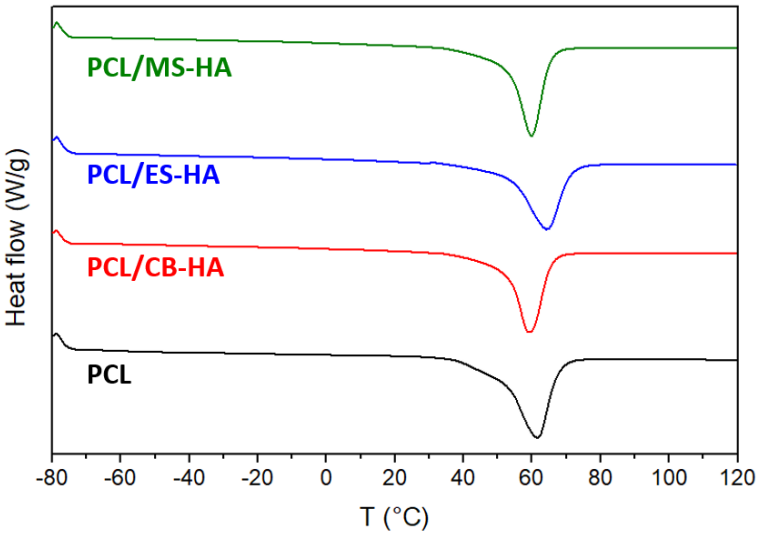

Figure 5-2 DSC curves of pure PCL and of the three composite materials.

Table 5-3 DSC data of PCL and of the PCL/bio-HA composites.

	PCL	PCL/CB-HA	PCL/ES-HA	PCL/MS-HA
T_m (°C)	61.5	59.3	64.3	59.9
H_m (J/g)	87.7	72.2	74.2	76.7
χ_c	62%	59%	60%	63%

The results of the DSC analyses are shown in Figure 5-2 and Table 5-3. It can be observed that neither the melting temperature nor the crystallinity seem to be significantly affected by the ceramic filler. In fact, the melting temperature is between 59°C and 64° for all materials and the crystallinity is in the range of 59-63%.

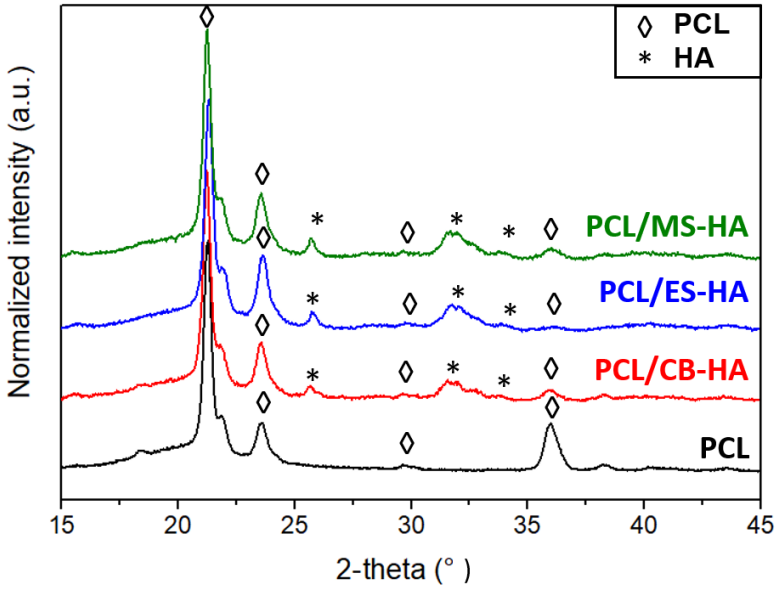

Figure 5-3 XRD curves of pure PCL and of the three composite materials.

Figure 5-3 shows the diffraction spectra of PCL and of the three composite materials. The PCL orthorhombic structure is revealed by the peaks at 2ϑ = 21.2°, 21.9° and 23.6°, that correspond to the planes (110), (111) and (200) [193], and by the peaks at 2ϑ = 29.7° and 35.9°, attributed to the (210) and (020) planes [194]. In the composite materials, the HA hexagonal lattice produce the reflections at 2ϑ = 25.7° (plane (002)) and at 2ϑ = 31-35°. This latter is a broad peak that correspond to the planes (211), (112), (300) and (202), which appear merged due to the broadening effect of the nanosized HA crystallites. This broadening effect was already observed in the XRD spectra of the bio-HA powders shown in Chapter 3.

5.3.2 Scaffolds characterization

The picture in Figure 5-4 shows the scaffolds 3D printed with the four different materials. It can be seen that the bio-HA particles change the white color of PCL, which becomes yellowish or reddish, most probably because the bio-derived powders contain some organic matter.

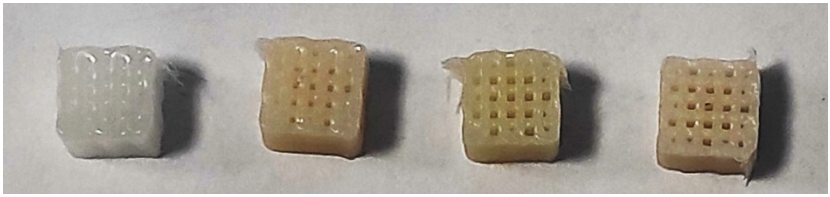

Figure 5-4 Picture of the 3D printed composite scaffolds. From the left: pure PCL, PCL/CB-HA, PCL/ES-HA and PCL/MS-HA.

Some SEM pictures of the scaffolds at different magnifications are shown in Figure 5-5 and the dimensions of the strands and pores, calculated based on these pictures, are summarized in Table 5-4. The strands of the pure PCL scaffolds have dimensions close to 600 μm, which is the dimension of the diameter of the nozzle. The PCL/CB-HA scaffolds, instead, have strands that are thicker than the nozzle, being around 670 μm. On the other hand, PCL/ES-HA and PCL/MS-HA scaffolds show thinner strands, i.e. about 540 μm and 570 μm thick, respectively. As a consequence, the pores are, in average, smaller than the target 400 μm in the PCL/CB-HA scaffolds (about 330 μm) and bigger in the other two composite scaffolds (about 460 μm and 420 μm).

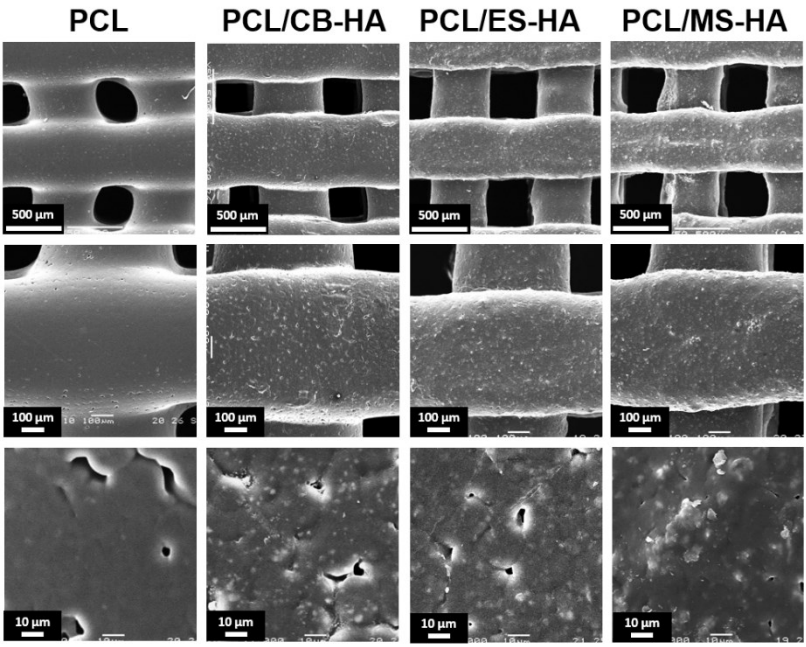

Figure 5-5 SEM micrographs of the 3D printed scaffolds.

Table 5-4 Dimensions of the 3D printed scaffolds.

	PCL	PCL/CB-HA	PCL/ES-HA	PCL/MS-HA
Scaffold base (mm)	5.60 ± 0.05	5.82 ± 0.02	5.59 ± 0.02	5.67 ± 0.06
Strands thickness (µm)	614 ±43	666 ± 46	542 ± 31	570 ± 47
Pores size (µm)	369 ± 42	328 ± 20	461 ± 21	422 ± 23

The diameter of the strands depends on the material flow and, since the air pressure and the printing speed were the same for all materials, the flow is supposed to depend only on the material viscosity. The viscosity of a thermoplastic composite material is generally expected to increase with the amount of ceramic filler and its SSA (specific surface area) and to decrease with the temperature [195]. Therefore, the SSA measurements (see paragraph 3.3.2) could explain why the strands of PCL/ES-HA, printed at 110°C, are thinner than those of PCL/CB-HA, printed at 100°C. In fact, the ES-HA powder has SSA = 124 m^2/g, much higher than CB-HA, that has SSA = 47 m^2/g. Moreover, the higher content of ceramic filler of PCL/MS-HA (14.1 wt%) with respect to the other two materials (13.1-13.2 wt%), combined with a SSA = 94 m^2/g, could explain why PCL/MS-HA required a temperature of 150°C to be printed, while the other two composites showed a sufficient flow at 100-110°C.

Another thing that can be noticed in the SEM micrographs of pure PCL (Figure 5-5) is that subsequent layers of deposited material appear fused together, as if the time span between the deposition of two layers was not enough for the solidification of the polymer. As a consequence, the shape of the pores is not perfectly squared but rather elongated in the deposition direction. Since this effect is not visible in the composite scaffolds, most probably the bio-HA particles accelerated the solidification of PCL.

The SEM pictures clearly show, in the composite scaffolds, the presence of ceramic particles aggregated in clusters of 1-10 μm. Anyhow, these clusters appear to be homogeneously dispersed in the polymeric matrix. Some micropores are visible on all the scaffolds, especially on the biocomposite ones. Moreover, it can be noticed that the bio-HA particles create a certain roughness on the scaffolds' strands, while the pure PCL ones look smoother. Micropores and roughness, along with the chemical composition, are factors that are thought to influence the interaction of the material with the bone cells.

The stress/strain curves related to the compression tests are shown in Figure 5-6 and the resulting mechanical properties, elastic modulus and yield stress, are listed in Table 5-5. The compression modulus ranges from 177 MPa (pure PCL) to 316 MPa (PCL/CB-HA) and the yield stress from 6.1 MPa (PCL/ES-HA) to 12.1 MPa (PCL/CB-HA), which are values that are comparable with those of trabecular bone (see paragraph 1.2).

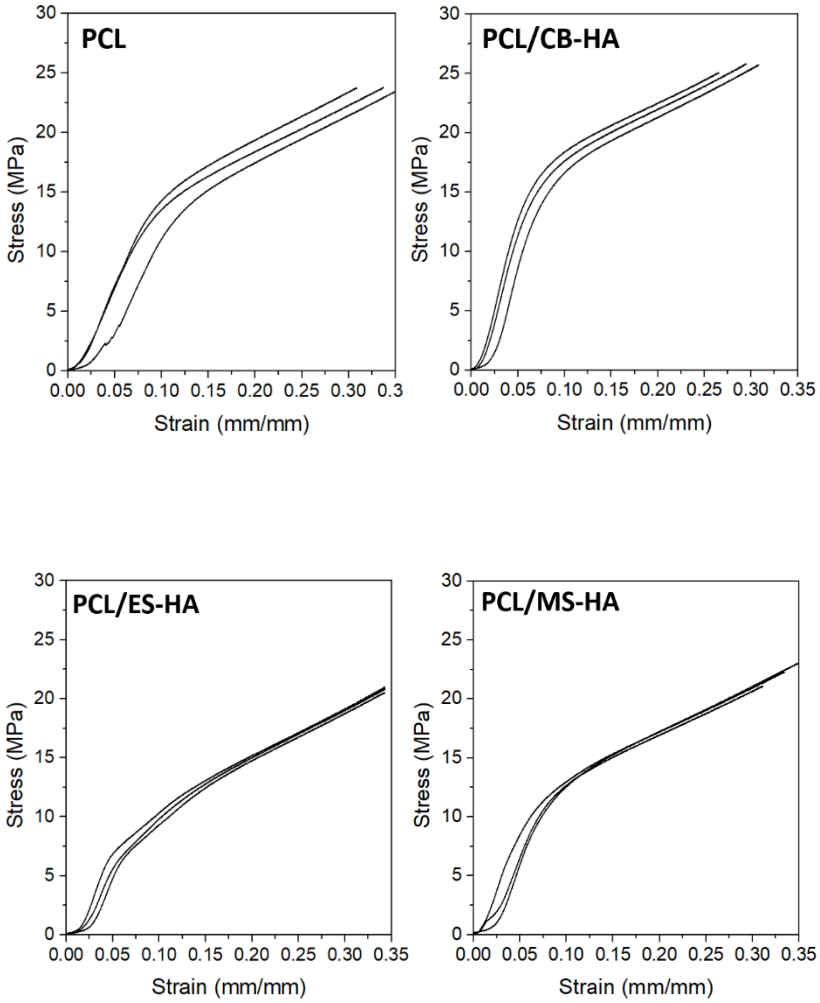

Figure 5-6 Stress/strain curves of the mechanical compression tests of the 3D printed scaffolds.

Table 5-5 Mechanical properties of the 3D printed scaffolds.

	PCL	PCL/CB-HA	PCL/ES-HA	PCL/MS-HA
Compressive Elastic Modulus (MPa)	177 ± 9	316 ± 10	203 ± 17	219 ± 14
Yield Stress (0.2% offset) (MPa)	11.4 ± 0.9	12.0 ± 0.5	6.1 ± 0.3	8.6 ± 1.1

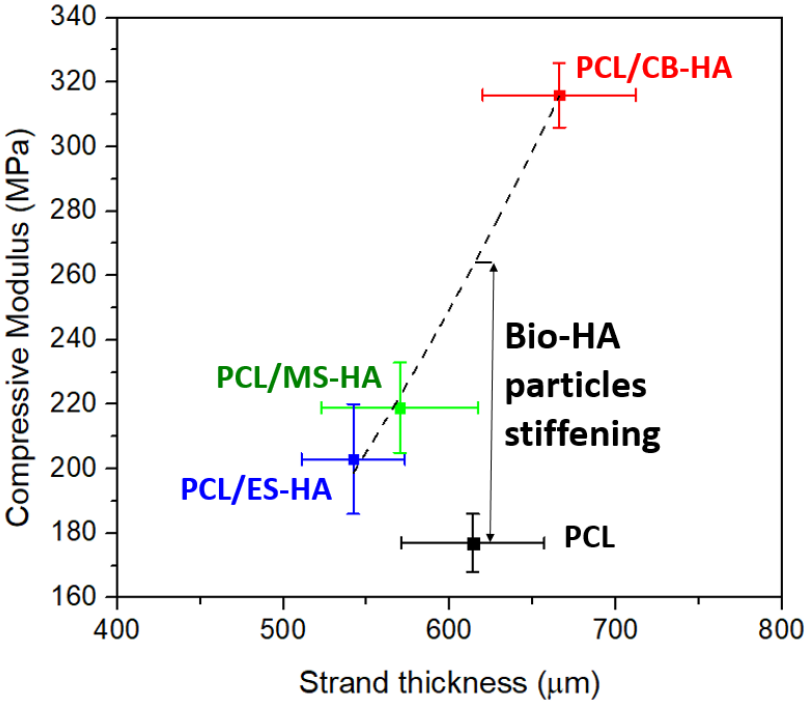

Figure 5-7 Compressive moduli vs. strand thickness. The modulus increases linearly with the thickness of strands, so the stiffening effect of the bio-HA particles is visible by comparing pure PCL to the bio-HA composites.

The elastic modulus of a porous scaffolds depends on its porosity, i.e. on the thickness of the strands and on the dimension of the pores. This relationship can be described by the following equation [196]:

$$E_{porous} = E_{solid} C\ (1 - \phi)^n \quad (6)$$

where ϕ is the fraction of porosity (from 0.0 to 1.0), C is a constant depending on the microstructure of the material and n is a number that varies from 1 to 4.

The compressive moduli of the 3D printed scaffolds as a function of the thickness of the strands are plotted in Figure 5-7. It can be observed that the moduli of the composite scaffolds increase linearly with the strand thickness, while that of pure PCL is considerably lower, despite its relatively low porosity. This suggests that the ceramic particles have a stiffening effect on the polymer matrix and, in particular, the contribution of the HA particles to the total modulus can be estimated, with a simplified approach, by fitting the modulus versus the strand thickness with a power-law equation, as shown in Figure 5-7. It results that the addition of ~ 15 wt% of bio-HA particles improves the compressive modulus of the PCL scaffolds of about 50%, which is in agreement with another study [197], which found that 10 wt% of HA particles increase the PCL compressive modulus of 46%, while 20 wt% particles of 61%.

5.3.3 Biological *in vitro* tests

The metabolic activity and the number of MG63 cells on the 3D printed scaffolds after 1, 3 and 7 days of culture are shown in Figure 5-8. The metabolic activity (Figure 5-8a) of cells seeded on PCL/MS-HA and PCL/CB-HA scaffolds increases from day 1 to day 7 and, eventually, is significantly higher than the other samples. Pure PCL and PCL/ES-scaffolds, instead, show a decrease in metabolic activity from day 1 to day 3, and then an increase from day 3 to day 7. Anyway, at day 7, the metabolic activity remains at low levels for pure PCL, while it is much higher on PCL/ES-HA, even if it does not reach the same level of the cells seeded on PCL/MS-HA and PCL/CB-HA scaffolds.

Cell proliferation analyses (Figure 5-8b) revealed a gradual increase of cells from day 1 to day 7 on all samples. However, starting

from day 3, the cells on the composite scaffolds are significantly more than those on scaffolds made of pure PCL, thus confirming the beneficial effect of the bio-HA particles. Among the different sources of bio-HA, the mussel shell-derived particles (PCL/MS-HA) promote the largest number of adhered cells, both after 3 and after 7 days of culture. PCL/CB-HA scaffolds showed a large proliferation of cells from day 3 to day 7, while PCL/ES-HA scaffolds, even with a constant increase of the cell number, show less adhered cells at day 7 with respect with the other two composite scaffolds.

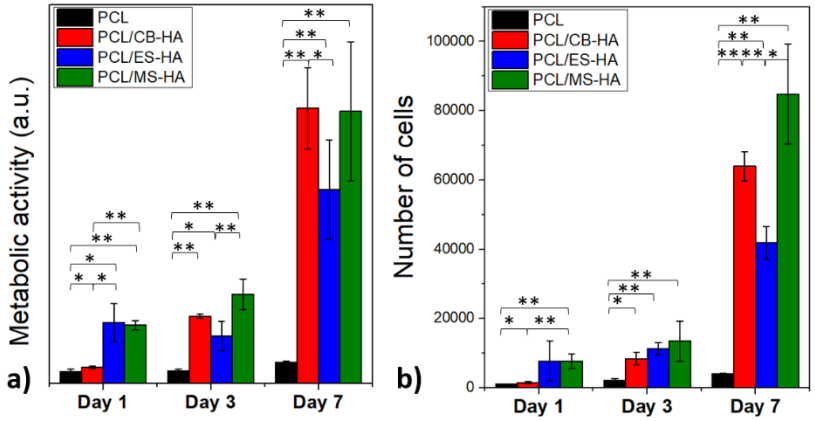

Figure 5-8 Metabolic activity and number of cells on the 3D printed scaffolds after 1, 3 and 7 days of culture. * p-value < 0.05, ** p-value < 0.01.

The confocal images in Figure 5-9 show the cells adhered on the scaffolds after 1, 3 and 7 days of culture and, in general, are consistent with the cell proliferation analyses. In fact, pure PCL scaffolds show only few cells aggregated in clusters, even at day 7, while the scaffolds containing bio-HA particles show a significant increase of adhered cells starting from day 3. Moreover, the highest adhesion ability of the PCL/MS-HA scaffolds is confirmed by the confocal images, as, at day 7, one can observe a continuous monolayer of cells covering all the scaffold's surface.

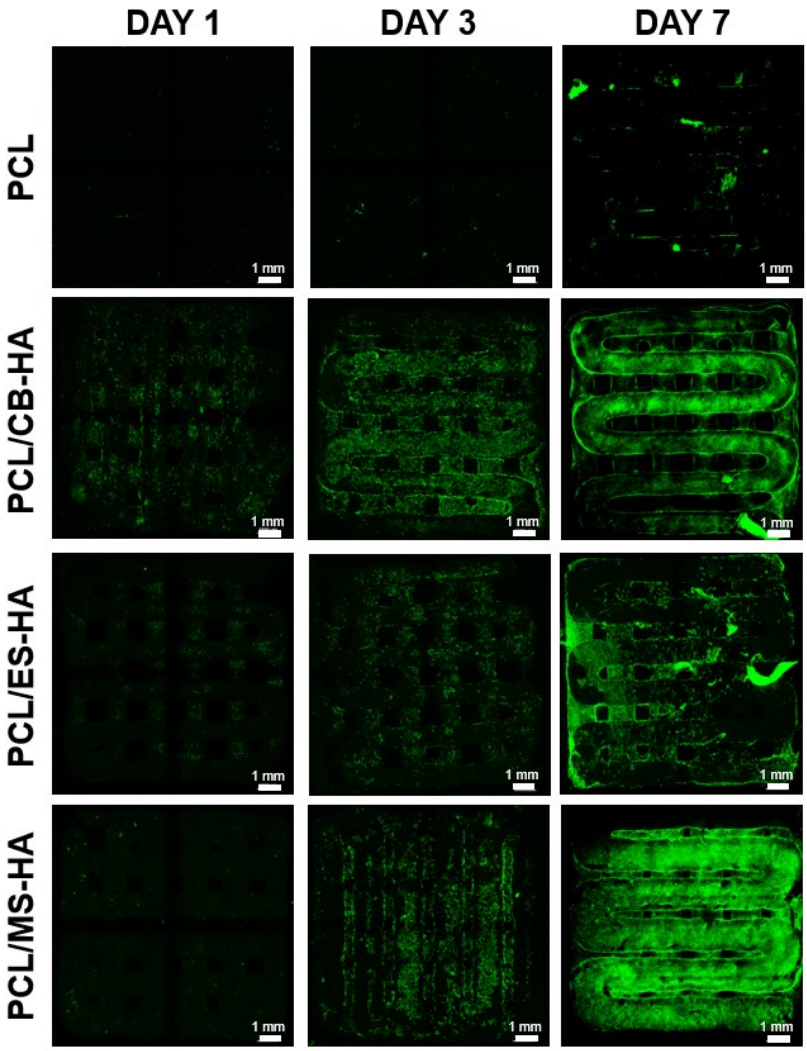

Figure 5-9 Confocal images of the cells adhered on the 3D printed scaffolds after 1, 3 and 7 days of culture.

The reasons behind the different behaviours of the cells seeded on the three different composite scaffolds are difficult to assess, but some

hypothesis can still be done in the frame of this discussion. First, since it is clear that the bio-HA particles do have a positive effect on the ability of the scaffolds to promote cell proliferation, the higher number of cells on the PCL/MS-HA scaffolds with respect to the others can be attributed to their slightly higher content of bio-HA particles (14.1 wt% instead of 13.1-13.2 wt%, see paragraph 5.3.1). Considering that the difference is only 1 wt% (less than 8%), this remains just a hypothesis that should be verified, for example by repeating the tests varying also the concentration of bio-HA particles.

Second, the reason of the low performance, so to say, of the PCL/ES-HA scaffolds compared to the other two could be linked to the different chemical composition of the biogenic sources. In fact, as showed in paragraph 3.3.2, strontium is present in both MS-HA and CB-HA, but not in ES-HA, which contains instead the largest content of magnesium. As already said in the introduction (paragraph 1.5), it is reported that Sr^{2+} could active the calcium-sensing receptor, resulting in the regulation of genes that, controlling bone resorption, promote the proliferation of osteoblasts [57]. In fact, Sr-substituted apatites are attractive for bone regeneration applications, as they were found to possess better bioactivity than pure hydroxyapatite [32,58]. However, Mg^{2+} should also have beneficial effects on bone formation [59] and, since the quantities of Sr^{2+} and Mg^{2+} in these bio-HAs are very low (0.1-0.4 wt% of 13.1-14.1 wt% of bio-HA particles in PCL), it is difficult to evaluate the effect of these ions in this work.

5.4 Conclusions

The pure PCL and the three PCL/bio-HA composites (with MS-HA, CB-HA and ES-HA) required to be heated at different temperatures in order to be processed by extrusion 3D printing in an optimal way. This is most probably due to the different specific surface area (SSA) of the bio-HA powders and to the different final content of HA particles in the composite (about 1 wt% higher in PCL/MS-HA), two factors that affect the viscosity of the melt.

However, even by changing the process temperature, the 3D printed scaffolds showed strands with different thicknesses, i.e. different porosities, as a consequence of a different material flow during printing. This affected the mechanical properties, in particular the compressive modulus of the scaffolds, which was higher for scaffolds with thicker

strands and lower porosity. Regardless this, scaffolds of pure PCL showed lower stiffness with respect to the composite ones, highlighting that the bio-HA particles improved the compressive modulus of about 50%. In general, the moduli were comparable with those reported for trabecular bone, being between 203 MPa and 316 MPa.

The biological *in vitro* tests clearly showed that the bio-HA nanoparticles significantly improved the bioactivity of PCL, promoting faster cell proliferation and better metabolic activation. Among the three composite scaffolds, the PCL/MS-HA ones were found to have the best interaction with the cells, while those of PCL/ES-HA the poorest. The reasons for this are unclear but, perhaps, they may be attributed to the higher bio-HA content in the PCL/MS-composite and to the different ionic composition of the biogenic sources.

Chapter 6

Powder 3D printing of bioceramic scaffolds

6.1 Introduction

The study presented in this chapter explores the possibility of using bio-derived nanopowder in the powder 3D printing process (P-3DP or binder jetting). Due to the fact that a relatively large amount of powder is needed for P-3DP, only the cuttlebone-derived powder was used because, as seen in Chapter 3, it is faster to synthesize. As already said in the introduction, the main problem of using bio-derived HA in P-3DP is the nanometric size of the powder. This issue was overcome by mixing the cuttlebone-derived nanopowder with a glass-ceramic powder with bigger particle size. Therefore, scaffolds with or without bio-derived powder were fabricated and compared in terms of biological behaviour *in vitro*. In addition, since the P-3DP process allows to design very freely the shape of the scaffolds and of the pores, scaffolds with different pore geometries were produced: with pores of uniform size and with a size gradient. This study was carried out mainly in Berlin, during the time spent as guest PhD student at the division of Advance Multi-Material Processing of BAM (Federal Institute for Materials Research and Testing), headed by prof. Jens Günster. Part of the material presented in this chapter has been already published in [198].

6.2 Methods

6.2.1 Bioceramic scaffolds fabrication by P-3DP

The cuttlebone-derived powder was synthesized from raw cuttlebones as described in Chapter 3. Since a large amount of powder was expected to be needed for the P-3DP process, the synthesis parameters were chosen in order to guarantee the maximum efficiency in the minimum time: initial pH = 3.2, milling time = 30 min and drying temperature = 150°C.

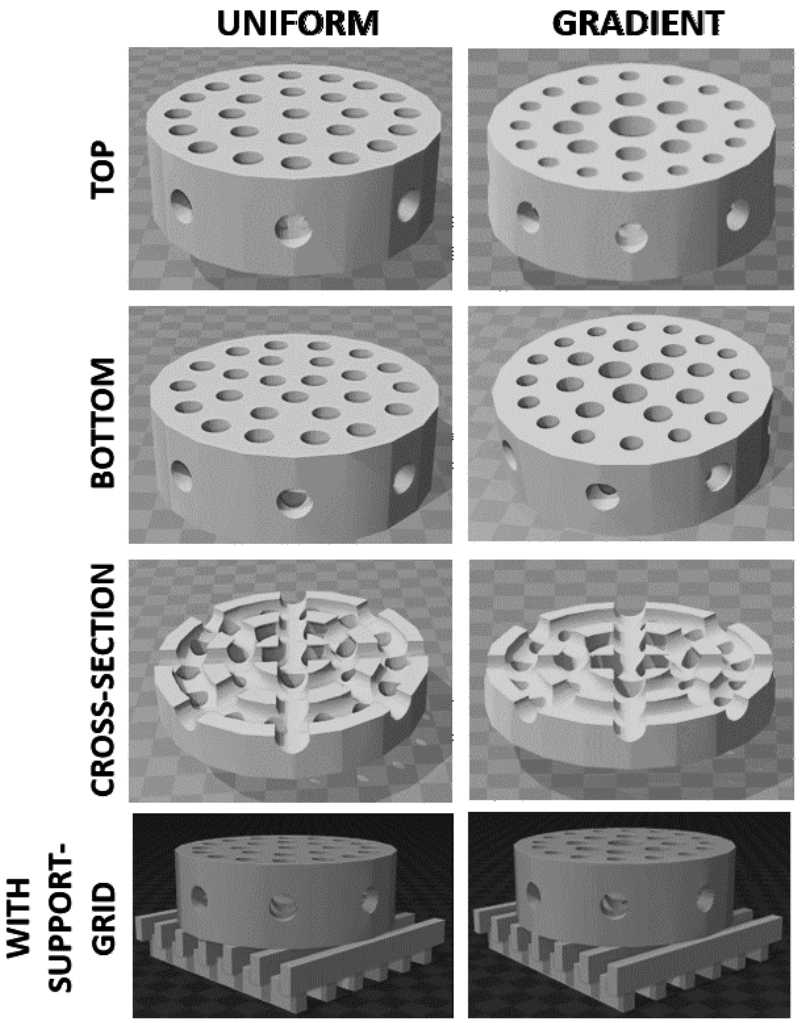

Figure 6-1 CAD models of the scaffolds with two different pore geometries: uniform or size-gradient pores.

The 3D cad models of the scaffolds were designed with the software Tinkercad® from Autodesk®, available online. All scaffolds have a round shape with a diameter of 9 mm and a thickness of 3 mm. The two

different pore geometries, with uniform pore size or with a size-gradient, are shown in Figure 6-1. The pores on the top and on the bottom are placed in different positions, in order to not have pores that pass through the whole thickness and therefore to avoid that the cells seeded during the biological tests end up on the bottom of the wells. However, the pores are all interconnected through circular channels and channels in the radial direction in the centre of the scaffolds' thickness (see the cross-sections in Figure 6-1). Uniform pores were designed with a diameter equal to 0.85 mm and the gradient-size ones with diameters of 1.5 mm, 1 mm and 0.7 mm (dimensions are slightly different for the pores on the bottom). The dimensions and number of pores were carefully chosen in order to guarantee the same amount of total macroporosity in both geometries. A support grid was also designed and printed together with the scaffolds, with the function of stabilizing the printed parts in the powder bed, preventing unwanted movements of the printed layers.

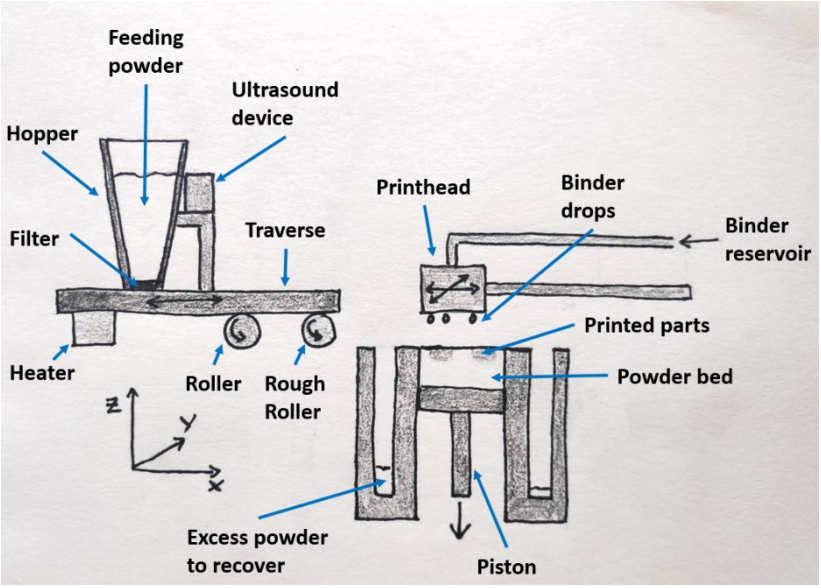

Figure 6-2 Schematic representation of the printer used to print the scaffolds.

The printing was performed with a commercial printer ExOne Innovent+® (The ExOne Company, Pennsylvania, USA), which is schematically represented in Figure 6-2. The binder, provided by the

producer, was an organic resin that solidifies by heating. The working process of this printer is briefly described as follows. The powder material is fed into a hopper, equipped with a metallic filter at its bottom, that moves in the x-direction. The hopper activates ultrasounds while passing above the powder bed, and the ultrasound intensity regulates the powder flow. Two rotating rollers, fixed on a traverse just after the moving hopper, flatten the powder bed and remove the excess powder. Then a movable printhead (x- and y-directions), equipped with multiple nozzles, selectively spit liquid binder drops on the desired spots, and the binder quantity is regulated by the set level of saturation. A movable heater, fixed before the hopper, passes above the powder bed to consolidate the binder, then the powder bed moves down in the z direction of a height corresponding to the layer thickness and new powder is spread again by the hopper to form the next layer.

Initially, some printing trials were performed with the as-synthesized powder. However, the printing was not possible due to the fact that the organic material present in the cuttlebone-derived powder was deteriorating during the heating phase, creating zones of brown color and irregularities in the powder bed surface. Therefore, the organics were eliminated from the powder by heat treating it at 800°C for 5 h (heating rate 10°C/min). The resulting powder will be called CB-800.

Then, other printing trials were performed, but again the results were not satisfactory due to the nanometric size of the powder. The main issues were: roughness of the powder bed surface, stickiness of the powder on the flattening rollers and fragility of the green parts, due to the low packing density (or high SSA) and therefore the low capability of the binder to wet and bind the particles together. To overcome this issue, some nanopowder was agglomerated by spray drying using a Niro Atomizer Minor (Copenhagen, Denmark). The granules showed perfectly rounded shapes and dimensions of about 80 ± 40 μm. Although the powder bed surface was very smooth and the granules were not sticking to the rollers, the green parts were still too fragile, indicating that the capability of the binder of wetting and binding the granules was still not good, even when using the maximum binder saturation (400%).

Therefore, the nanopowder was mixed with a glass-ceramic powder of bigger particles size, previously sieved to be in the range of 45-100 μm. The glass-ceramic, called AP40mod, had been previously prepared at

BAM (Berlin, Germany), following a procedure described in [199]. The name "AP40mod" means "AP40 modified", as it was developed modifying another material by adding titanium oxide. The chemical composition of AP40mod is (wt%): 39.60 SiO_2, 32.04 CaO, 11.26 P_2O_5, 2.01 Na_2O, 3.52 MgO, 5.03 CaF_2, and 6.54 TiO_2.

The AP40mod powder was mixed with CB-800 for about 30 min in a glass bottle with zirconia balls, using a Turbula® mixer at 23 rpm. The materials were mixed in different proportions, from 10 wt% to 50 wt% of CB-derived nanopowder, but only the mixture with 10 wt% nanopowder was suitable to be printed. In fact, with 20 wt% of CB-800, the powder was sticking too much to the rollers even at a very low speed and the green parts were too fragile to be handled even at high saturation levels. It has to be noticed that, although 10 wt% seems quite a low percentage, the CB nanopowder occupies a large volume, so the volume fraction is much higher.

Table 6-1 Parameters used for 3D printing the two different powders.

Parameters	Unit	AP40mod	10%CB-CaP
Layer height	µm	50	50
Bed temperature	°C	80	80
Binder saturation	%	100	110
Recoater speed	mm/s	100	20
Ultrasound intensity	%	50	100
Roller traverse speed	mm/s	3	1.5
Roller rotation speed	rpm	300	150
Rough roller rotation speed	rpm	250	100

For the printing, the layer height was set to 50 µm and the bed temperature, which in turn regulates the heater power, was set to 80°C.

The other printing parameters needed to be adapted for the mixture containing 10 wt% of CB-derived powder, which will be called 10%CB-CaP. In particular, the addition of nanoparticles required: enhancing the ultrasound intensity and slowing down the hopper (recoater) speed to increase the deposited powder for each layer; reducing the traverse speed and the rollers rotation speed to limit the stickiness of the powder to the rollers; increasing the binder saturation to improve the mechanical resistance of the green parts. The printing parameters used for the two materials are summarized in Table 6-1. It is worth to observe that the addition of nanopowder required to slow down the speed during the spreading of new powder and during the passage of the rollers, which significantly increased the total printing time. It has to be taken into account, therefore, that a larger amount of nanopowder leads to a longer printing time.

After printing, the green parts were extracted from the powder bed and placed in an oven at about 100°C overnight in order to completely solidify the binder. Then the scaffolds were cleaned with compressed air to remove the excess powder and the support grid was eliminated by gently scratching the scaffolds with sandpaper. The sintering was carried out in a Carbolite RHF-1400 furnace following this thermal treatment: de-binding through heating to 500°C at slow rate (3°C/min); first crystallization step at 800°C for 2 h (heating rate 10°C/min); second crystallization step at 1150°C for 2 h (heating rate 10°C/min) and free cooling in the furnace. The two crystallization steps were performed in order to fully crystallize the AP40mod, which undergoes two crystallizations, as will be discussed in the results section.

6.2.2 Materials and scaffolds characterization

Since the CB-derived powder used in this study was synthesized with a new combination of synthesis parameters, the ICP/OES analysis was performed again in order to check the Ca/P ratio and the presence of additional ions. The analysis was performed with a Spectro Ciros Vision CCD, following exactly the same procedure described in Chapter 3. Similarly, the FT-IR spectrum was recorded with a FTIR Thermo Optics Avatar 330, as in Chapter 3.

The particle size distribution of the CB-derived powder was measured with a laser diffraction particle size analyser Mastersizer 3000 (Mavern Panalytical GmbH), following the ISO 13320 (01/2020). For the

measurement, approximately 0.3 g of CB-powder was suspended in a 3 mol/l tetra-sodium diphosphate solution by stirring and then dispersing with ultrasounds.

The capability of flowing regularly is important for a powder in order to be used in P-3DP and it is called flowability. The flowability of the mixtures of AP40mod powder and 0-100 wt% CB-derived nanopowder was evaluated by calculating the Hausner ratio (HR) [200] as:

$$HR = \frac{\rho_{tapped}}{\rho_{free\ settled}}$$

where $\rho_{free\ settled}$ is the free settled density of the powder and ρ_{tapped} is the tapped density. The different mixtures, one by one, were placed in a 250 cl glass cylinder and the free settled density was calculated by simply dividing the mass of the powder by the occupied volume. Then the cylinder was placed in a jolting volumeter STAV-2003 (JEL, Germany) and 1250 cycles of tapping were performed. The 1250 cycles of tapping were repeated until the volume stopped decreasing. The final density is called tapped density. The HR, which is the ratio of the two densities, is an indicator of the powder flowability, the higher the HR, the lower the flowability. The procedure was replicated three times per each powder sample.

TGA/DTA analyses were performed with a STA 409 thermobalance (NETZSCH Geraetebau GmbH) on AP40mod and 10%CB-CaP powders in order to evaluate the crystallization temperatures. The samples were heated in alumina crucibles at 10°C/min from room temperature to 1160°C in flowing air.

The real density of the CB-800 powder (after the elimination of organics) and of the AP40mod powder, before and after crystallization, were measured by pycnometry, using a pycnometer from Pycnomatic (Porotec, Germany). This was done in order to calculate the relative density and the porosity of the sintered bodies.

X-ray diffraction analyses were performed on the powders and on the sintered bodies, after crushing them again into powders, in order to assess the crystallographic phase composition. The instrument used was a Rigaku IIID-max, Cu radiation (1.5406 Å), scan step 0.05°, step time 2 s and 2-theta range 10°-80°. The qualitative and quantitative analysis was

carried out with the software MAUD© [159], using the following phases downloaded from the database COD [160]: hydroxyapatite n. 4317043 [170], β-tricalcium phosphate n. 1517238 [183], wollastonite n. 9005777 [201], titanite n. 9000489 [202], cristobalite n. 1010944 [203] and diopside n. 1000007 [204].

The bulk density of the sintered scaffolds was measured by the Archimedes' method, considering five samples per each material and following the ISO18754:2013(E) standard. The total porosity, which includes the macroporosity, was instead evaluated by simply weighting ten samples per type and measuring their volume with a calliper.

The pores' dimensions were measured by analysing the pictures taken with an optical microscope Keyence VHX-100 with the software ImageJ. Electron microscopy was instead used to see the morphology of the fracture surface of the sintered scaffolds, using a FE-SEM SUPRA 40 (Carl Zeiss Microscopy GmbH).

6.2.3 Biological *in vitro* tests

First, the potential cytotoxicity of the 10wt%CB-CaP scaffolds was evaluated by the LDH assay, using human embryonal lung fibroblasts (MRC5 cell lines). The cells were placed for 48 h into extractions previously prepared by soaking the scaffolds into a standard medium for 72 h at 37°C. The positive control group was represented by the cells cultured in standard medium. Five replicates per variant were considered.

Once assured the non-cytotoxicity of the materials, a human bone marrow-derived mesenchymal stem cell line (hMSCs, ATCC number: PCS-500-012) was selected for the successive tests and therefore expanded in α-MEM medium containing 15% of fetal bovine serum (EuroClone) and 1% of antibiotic/antimycotic (Euroclone). The cells were cultured in standard conditions (37°C in 5% CO_2 humidified atmosphere), changing the medium every second day. A solution of 1% trypsin-EDTA (EuroClone) was used to detach the cells when they reached 70% confluence and then the cells were suspended in a standard medium at concentration 333,000 cells/ml.

The 3D printed scaffolds were sterilized by putting them in autoclave at 121° for 15 min. Then the scaffolds were placed in 48-well plates and

covered with 0.3 mm of cell suspension (100,000 cells/well). Cells seeded onto the tissue culture plate were used as control group. After 24 h of incubation in standard conditions the samples were moved in new 48-well plates and covered with standard medium. This was done in order to keep only those cells that adhered on the scaffolds and not those on the bottom of the wells. The cell culture was carried on for 10 days, changing the medium every second day.

As in Chapter 5, the metabolic activity was evaluated by the AlamarBlue assay (Invitrogen, Carlsbad, USA), the cell number by PicoGreen DNA assay (Invitrogen, Carlsbad, USA) and the cells adhered on the scaffolds were observed by confocal microscopy. These tests were performed after 3, 5 and 10 days of culture. For the AlamarBlue and PicoGreen assays, four replicates per variant (scaffold material and geometry) were considered.

The AlamarBlue reagent was added into each well, to reach the concentration of 10 vol% in the culture medium. After incubation in standard conditions for 3 h, 100 µl of reagent/medium solution was collected from each well and placed in a Tecan Infinite 200 microplate reader (Tecan Group, Männedorf, Switzerland), which measured the fluorescence signal of the emission wavelength 590 nm (excitation wavelength of 560 nm).

The procedure for quantifying the cells by PicoGreen assay was the following. After removing the culture medium the samples were washed with PBS solution, covered with 300 µl of 0.05% Triton-X PBS solution and incubated for 1 h in standard conditions. Then a Hielscher UP400S ultrasonic homogenizer (Hielscher Ultrasonics, Teltow, Germany) was used to sonicate the samples for 10 s at 400 W-24 kHz, cycle 1, amplitude 40%. 100 µl of supernatant was collected from each well and placed in a black 96-well plate, where it was mixed with 100 µl of PicoGreen solution. The fluorescence intensity at the emission wavelength of 535 nm was measured with the Tecan microplate reader, using the excitation wavelength 485 nm. The calibration curve was built using a DNA standard included in the PicoGreen kit and the number of cells was calculated by using the conversion factor 7.7 pgDNA/cell.

For confocal microscopy, the cells were stained with Oregon green phalloidin and 4′6-diamidino-2-phenylindole (DAPI), which give a green fluorescence to the cytoskeletons and a blue fluorescence to the nuclei,

respectively. At each time point the samples were fixed with a 4% solution of paraformaldehyde, washed with PBS solution, permeabilized with a 0.2% Triton X-100/PBS solution for 30 min, washed again and left soaking in 5.0 µl/well of Oregon green phalloidin and 1.0 ml/well (5.4 µl dilute in 25.0 ml PBS) DAPI solutions for 1 h. After other three washings with PBS, the cells adhered on the scaffolds were observed with a confocal laser microscope (Zeiss LSM 510 Meta).

The statistical analysis was carried out with the software graphPad Prism 9 (La Jolla, CA), performing two-way ANOVA tests (all-pair-wise multiple comparison) and setting *p<0.05 as the level of significance.

6.3 Results

6.3.1 Powder materials characterization

The FT-IR spectra of the AP40mod powder and of the CB-derived powder heat treated at 800°C (CB-800) are shown in Figure 6-3. The peaks of the CB-800 spectrum are those typical of HA and β-TCP. Indeed, the peaks at 603 cm^{-1} and 565 cm^{-1} can be attributed to the ν_4 PO_4^{3-} vibrational mode of HA and those at 1041 cm^{-1} and 1088 cm^{-1} to the ν_3 PO_4^{3-}, also of HA [178]. At the same time, the absorptions at 980 cm^{-1} and 1120 cm^{-1} are most likely attributed to PO_4^{3-} groups in the β-TCP phase [205].

The infrared spectrum also reveals that the HA phase is actually carbonated, as the peak at 877 cm^{-1} and those between 1400 and 1600 cm^{-1} are attributed to ν_2 CO_3^{2-} and ν_3 CO_3^{2-}, respectively [178,179]. In addition, the peaks at 632 cm^{-1} and 3570 cm^{-1} are related to the structural OH^- groups in the crystal lattice of HA [178,179].

The infrared absorptions of AP40mod glass, instead, reveal the presence of Si-O bonds together with PO_4^{3-} groups. In fact, the broad and intense absorption between 800 cm^{-1} and 1200 cm^{-1} results from the overlapping of the asymmetric stretching of SiO_4^{4-} and the ν_3 modes of PO_4^{3-} [178,206,207]. The presence of phosphate groups is responsible also for the peaks at 571 cm^{-1} and 604 cm^{-1}, while silicate units with non-bridging oxygens for the peak at 482 cm^{-1} [208]. Moreover, adsorbed water molecules are revealed by both spectra by the bands at 1633-1639 cm^{-1} [209] and at 3442-3444 cm^{-1} [179].

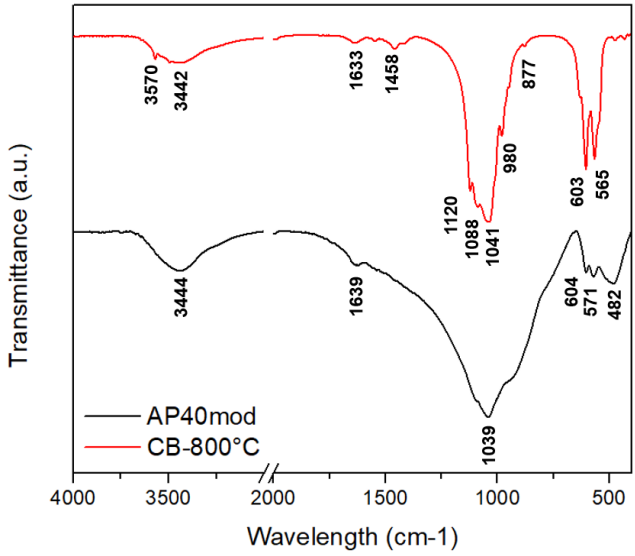

Figure 6-3 FT-IR spectra of AP40mod powder and of the CB-derived powder heat treated at 800°C.

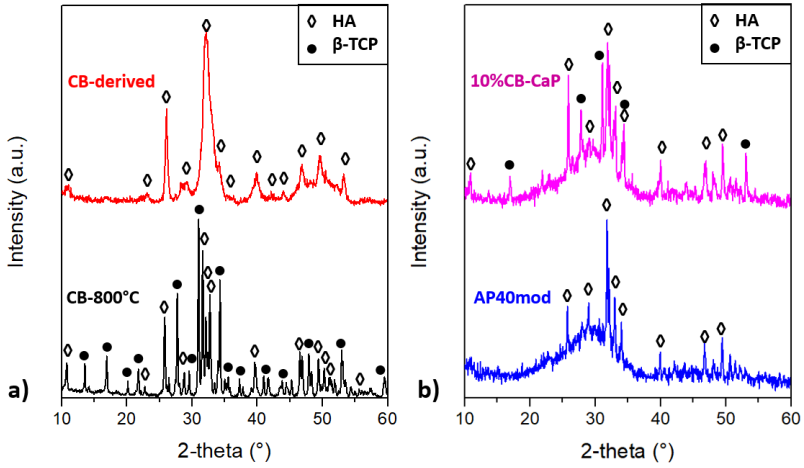

Figure 6-4 XRD patterns of the CB-derived nanopowder before and after the heat treatment at 800°C (a) and of the AP40mod powder, with or without the addition of 10 wt% of CB-800°C powder (b).

The crystallographic phases of the powder materials were investigated by XRD and the resulting diffraction patterns are shown in Figure 6-4. The CB-derived material was analyzed both before and after the heat treatment at 800°C and the two spectra are shown in Figure 6-4a. Before the heat treatment, only the HA phase is present and the shape of the peaks is that of nano-sized crystallites, as for the as-synthesized powders showed in Chapter 3. However, after the heat treatment, the peaks are sharper, indicating that the crystallites have grown in size to the micrometric scale, and the composition is ~47 wt% HA and ~53 wt% β-TCP, as calculated with the Rietveld analysis. This is agreement with the results of the ICP/OES analysis, which reveals a Ca/P molar ratio equal to 1.58. It is in fact known that, when subjected to high temperatures, calcium-deficient hydroxyapatites (CDHA) transform into HA (Ca/P = 1.67) and β-TCP (Ca/P = 1.5), their relative quantities depending on the lever rule [43]. On the other hand, the XRD spectrum of AP40mod is characterized by a broad, noisy band centered at about 30°, which reveals the amorphous nature of this glassy material (Figure 6-4b). However, some crystallized zones are also present, since small peaks attributed to the HA crystal lattice are also visible. The diffraction pattern of the 10%CB-CaP powder is, as expected, a sum of the spectra of CB-800 and AP40mod, revealing both amorphous phase, HA and β-TCP.

Finally, it is worth to mention that the CB-800 chemical composition include also the presence of small traces of K, Na, Mg, Sr and Zn, which were detected by the ICP/OES measurements.

The density measurements performed by pycnometry are listed in Table 6-2. The real density of CB-800 (3.009 ± 0.016 g/cm^3) is coherent with the literature [33] but it is slightly lower than what expected, given that β-TCP has a density of 3.08 g/cm^3 and HA of 3.16 g/cm^3. On the other hand, the density of the AP40mod powder was found to increase upon sintering, as a consequence of the crystallization of the glassy material.

Table 6-2 Density measurements of the powders by pycnometry.

	AP40mod (glassy)	**AP40mod (crystallized)**	**CB-800°C**
Density (g/cm^3)	2.875 ± 0.04	2.967 ± 0.01	3.009 ± 0.016

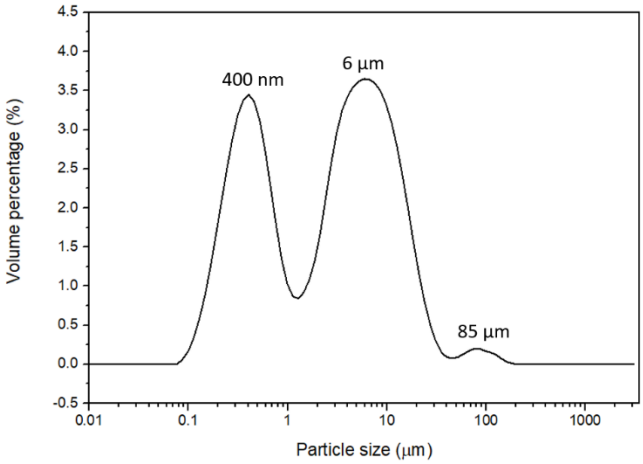

Figure 6-5 Particle size distribution of CB-derived powder heat treated at 800°C, measured by laser diffraction.

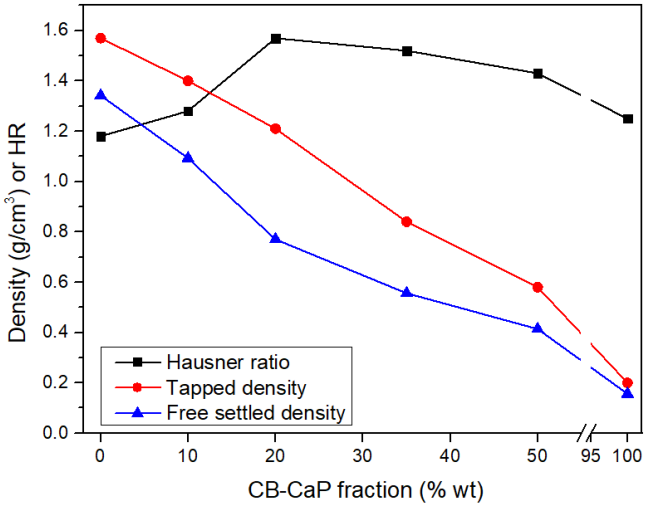

Figure 6-6 Free settled density, tapped density and Hausner ratio of AP40mod (45-100 μm) mixed with different wt% of CB-derived nanopowder. Standard deviations are not reported in the graph because they are small (< 0.01 g/cm³).

The particle size distribution of the CB-800 powder, as measured by laser diffraction, is shown in Figure 6-5. It can be observed that the powder exhibits a bi-modal distribution, with two main peaks at 400 nm and 6 μm. A small peak centred at 85 μm is also visible. Most likely the first peak is related to primary nanoparticles, which have dimensions in the range 90-1280 nm. Conversely, the other two peaks correspond to agglomerates of finer particles, which were not dispersed during the sample preparation.

The results of the measurements of the free settled density, the tapped density and the consequent Hausner ratio (HR) of AP40mod powder mixed with increasing quantities of CB-800 are shown in Figure 6-6. Both the tapped density and the free settled density gradually decrease with the addition of the nanopowder, since the packing density of the latter is very low. However, the HR does not increase gradually, as would be logical given that the flowability of the mixture gets worse and worse when a finer powder is added. In fact, a high HR is usually associated with higher friction among particles and therefore with worse flowability. This was what Sun et al. [199] observed when they added fractions of 0-25 μm fine powder to a 45-100 μm one. In our case, instead, the HR index increases up to 20 wt% nanopowder and then decreases. This is due to the fact that, when a large amount of nanosized powder is added to the mixture, the tapping process is not efficient anymore, because the interaction forces between nanoparticles are too strong to be broken by the tapping cycles and therefore the voids between particles are not eliminated. This is evident when looking at the tapped and free settled density of 100% CB-800, which are almost the same.

The TGA/DTA thermograms of the powder materials are shown in Figure 6-7. The CB-800 powder does not show any phase transformation or significant weight loss, just a little discontinuity is barely visible at 800°C, most likely due to the previous heat treatment. The DTA of the AP40mod powder, instead, shows two exothermic transformations, one starting at about 770°C and one at 870°C. These two transformations correspond to the two crystallizations of the AP40mod glass, as already observed in another study [199]. This crystallization behavior led to the choice of a two-step sintering cycle for the 3D printed scaffolds, with two isotherms at 800°C and 1150°C. The 10%CB-CaP powder also shows the presence of these two crystallizations, the first starting at 770°C, like pure AP40mod, and the second at 880°C, about 10°C more than the

AP40mod. This might indicate that the presence of the nanopowder somehow delay the second crystallization event, but the reason for this is still unclear.

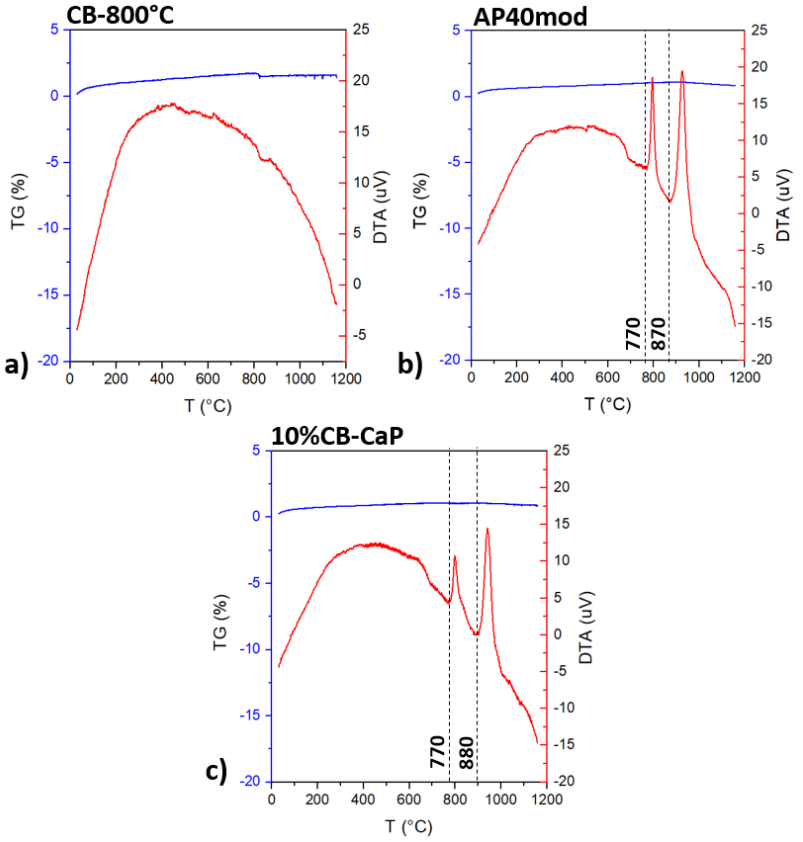

Figure 6-7 TG/DTA thermograms of the CB-800 (a); the AP40mod powder (b) and the AP40mod powder mixed with 10 wt% of CB-800°C powder (10%CB-CaP) (c).

6.3.2 3D printed scaffolds characterization

The crystallographic phase composition of the scaffolds after sintering was investigated by XRD and the resulting diffraction patterns are shown in Figure 6-8. AP40mod appears to be fully crystallized, with composition ~34 wt% β-wollastonite ($CaSiO_3$), ~27 wt% HA, ~18 wt% diopside ($CaMg(SiO_3)_2$), ~16 wt% titanite ($CaTiSiO_5$) and ~ 5 wt% β-cristobalite (SiO_2).

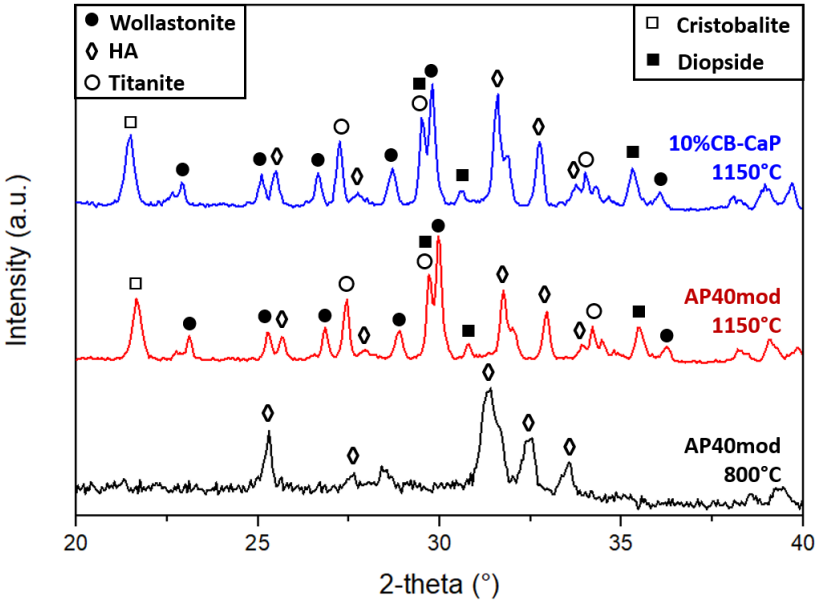

Figure 6-8 Diffraction patterns of the 10%CB-CaP and AP40mod sintered scaffolds; diffraction pattern of the AP40mod powder heat treated at 800°C.

As said in the previous paragraph, the DTA curve revealed that AP40mod is subjected to two different crystallization events, one starting at about 770°C and one at ~870°C (Figure 6-7). Therefore, in order to understand which phases crystallize first, some AP40mod powder was heated up to 800°C (10°C/min, no dwell, free cooling in furnace) and analyzed by XRD. The resulting spectrum (Figure 6-8) shows the presence of HA peaks only, which are very weak and come out from a noisy background. Although the big broad bump corresponding to the amorphous phase

(see the spectrum of the raw powder in Figure 6-4b) seems to be attenuated, it is very likely that the HA crystals have just began to nucleate and are still very small. However, this result leads to the conclusion that the first crystallization event corresponds to the formation of HA, while the second one is related to the crystallization of the other phases. This would be in agreement with a previous study [210], where a glass-ceramic with a composition similar to AP40mod was found to show two crystallizations as well, the first corresponding to apatite and the second to wollastonite.

The phase composition of the 10%CB-CaP sample is almost the same of that of the pure AP40mod one, but the relative quantities between HA and wollastonite are different. This can be easily seen by looking, in Figure 6-8, at the relative heights of the main peaks of HA (2-theta = 31.6°) and of wollastonite (2-theta = 29.8°). The quantitative analysis, carried out with the Rietveld method, allowed to calculate ~36/29 wt% of HA/wollastonite in the 10%CB-CaP sample, while ~27/34 wt% HA/wollastonite are the quantities calculated for pure AP40mod. The extra-amount of HA that is present in 10%CB-CaP comes from the addition of the CB-800 powder. However, the CB-800 powder is composed of ~50/50 HA/β-TCP, but β-TCP is not present anymore in the sintered scaffolds. It is therefore thought that, during sintering, β-TCP transforms into HA by taking up additional Ca atoms from the glass-ceramic. Therefore, the total HA phase that is present in the 10%CB-CaP scaffolds is produced partially by the AP40mod material and partially by the CB-derived nanopowder.

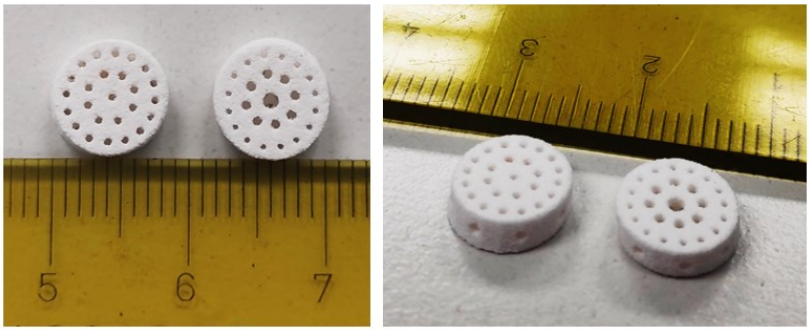

Figure 6-9 Pictures of two 3D printed scaffolds with two different pore geometries: uniform and gradient pore sizes.

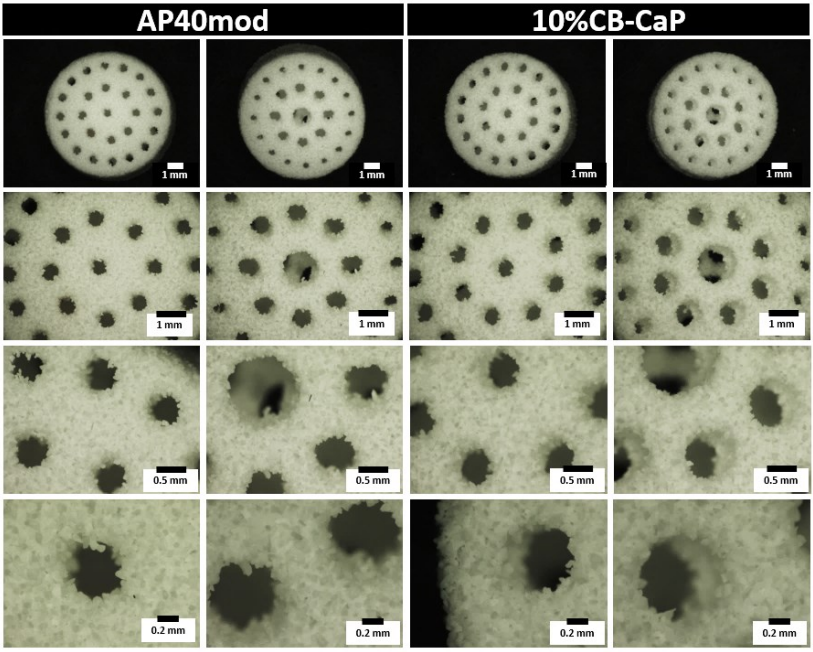

Figure 6-10 Optical microscope pictures of the four types of 3D printed scaffolds.

The geometry of the sintered scaffolds is well-defined, with pores with regular shapes, as can be observed from the pictures in Figure 6-9 and in Figure 6-10. The dimensions of the scaffolds and of their pores, calculated from the microscope pictures with ImageJ, are listed in Table 6-3. As can be seen, the reproducibility of the printing process was good, since the measured dimensions show relatively small standard deviations, below 0.1 mm. All dimensions are smaller than those set in the CAD files, obviously because of the shrinkage that occurs upon sintering. This shrinkage appears to occur mostly in the radial direction, as the final diameters are about 8.4-8.5 mm, while the diameter of the designed shapes was 9 mm. On the other hand, the thickness remained almost unchanged, it being ~3 mm, as in the original CAD files.

Table 6-3 also reports the total porosity, calculated by dividing the mass by the total volume, and the bulk density and the apparent porosity, which were measured by the Archimedes' method. The total porosity is

~60% for AP40mod and ~70% for 10%CB-CaP, therefore being in the range of the cancellous bone's typical porosity (see paragraph 1.2). It is quite clear that the AP40mod scaffolds reached higher densification levels than the 10%CB-CaP ones. In fact, the AP40mod scaffolds show smaller diameters, pores of smaller sizes, less total porosity, less apparent porosity and higher bulk density (1.57 g/cm^3, while that of 10%CB-CaP scaffold is 1.40 g/cm^3). This can be explained by considering the different material properties and particle size distribution of the two ceramic powders. The glassy AP40mod is made of bigger particles and, due to its amorphous nature, it easily densifies by viscous flow. On the other hand, CB-800 is made of nanosized particles of HA and β-TCP crystals. When the two powders are mixed, the small particles of CB-derived BCP most likely surround the bigger AP40mod particles and act like a shield between the glassy grains, slowing down the densification.

Table 6-3 Dimensions, mass, density and porosity of the 3D printed sintered scaffolds.

	AP40mod		**10%CB-CaP**	
	Gradient	**Uniform**	**Gradient**	**Uniform**
Diameter (mm)	8.41 ± 0.05	8.45 ± 0.08	8.46 ± 0.09	8.48 ± 0.09
Thickness (mm)	3.11 ± 0.06	3.09 ± 0.06	2.96 ± 0.07	2.94 ± 0.89
Mass (mg)	197 ± 2	195 ± 6	150 ± 5	148 ± 6
Pores size (mm)	1.17 ± 0.03 0.62 ± 0.05 0.34 ± 0.05	0.47 ± 0.04	1.26 ± 0.03 0.74 ± 0.07 0.44 ± 0.07	0.50 ± 0.06
Total porosity (%)	61	62	70	70
Bulk density (g/cm3)	1.57 ± 0.02		1.40 ± 0.09	
Apparent porosity (%)	47 ± 4		53 ± 3	

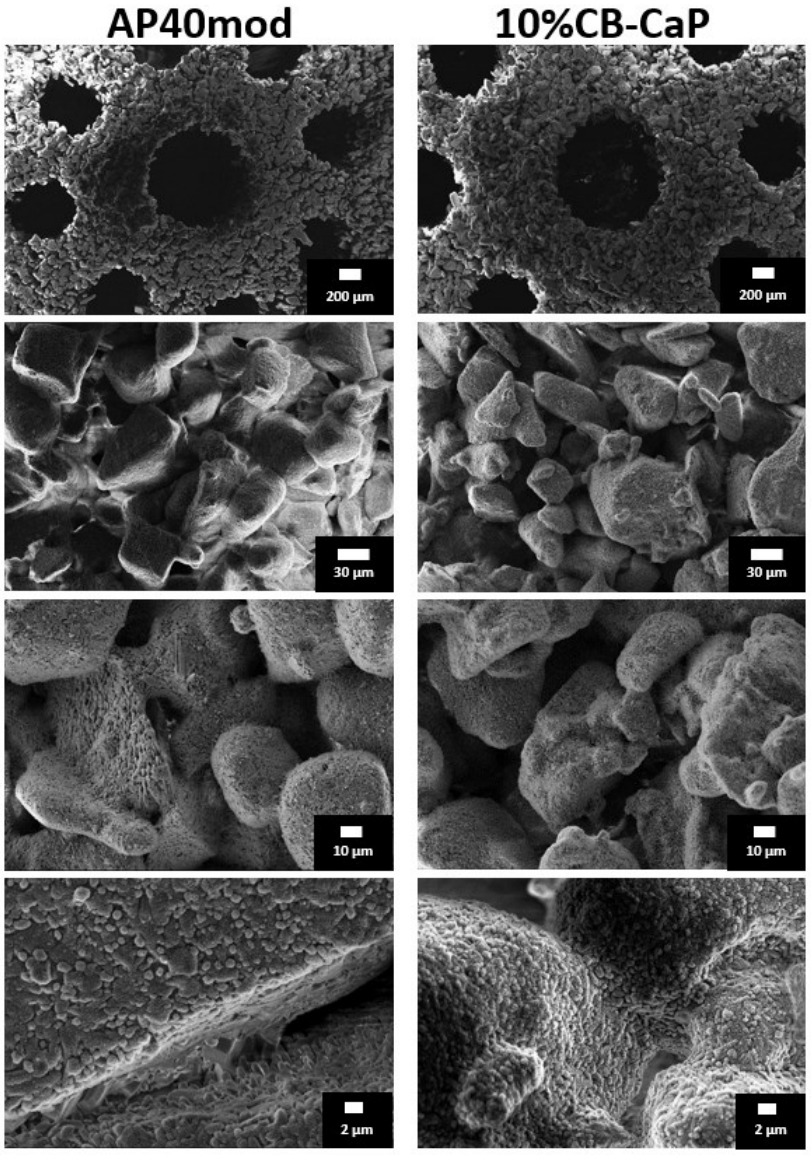

Figure 6-11 SEM pictures of the external top surfaces of a AP40mod and a 10%CB-CaP scaffold.

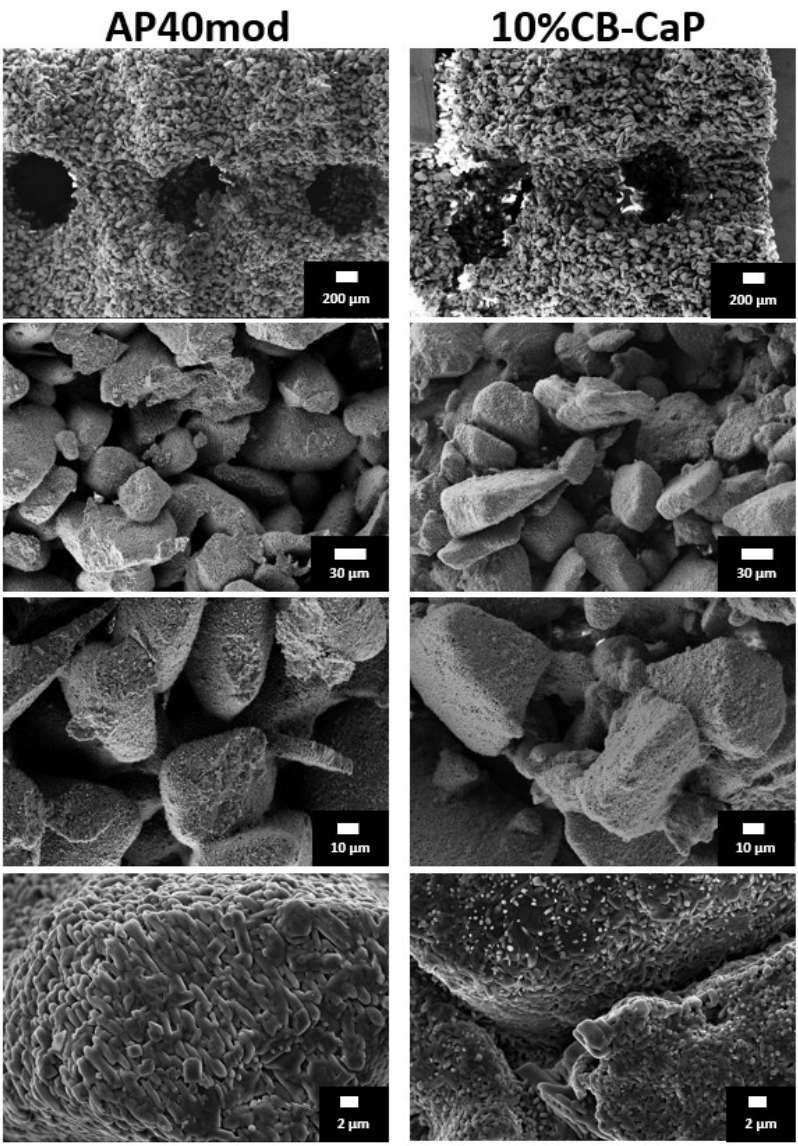

Figure 6-12 SEM pictures of the internal fracture surfaces of a AP40mod and a 10%CB-CaP scaffold.

This is somehow confirmed by the FE-SEM pictures shown in Figure 6-11 and Figure 6-12. The images taken at the highest magnification show that the big glass-ceramic particles are covered by many finer particles, which have dimensions < 1 μm. The presence of the small HA crystals that surround the bigger grains can be seen also in the images at lower magnification (2nd and 3rd row, Figure 6-12). Here, the big particles of the 10%CB-CaP scaffold appear smoother than those of the pure AP40mod, as if they are covered by very small particles that give them a silky texture.

6.3.3 Biological *in vitro* tests

The LDH released by the cells during the cytotoxicity test is shown in Figure 6-13. The death rate of the cells in contact with the extraction of 10%CB-CaP is almost the same as the negative control, well below the cytotoxicity threshold, which is 30%. Therefore, there is no cytotoxicity effect induced by the material or by the scaffolds' fabrication process.

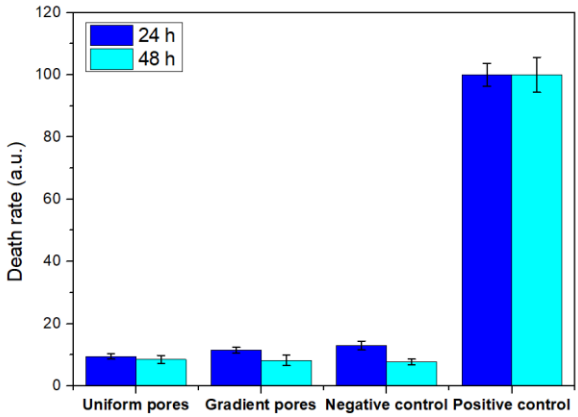

Figure 6-13 LDH released by the dead cells in a medium conditioned with the sintered 10%CB-CaP scaffolds.

The results of the cell proliferation and metabolic activity assays are shown in Figure 6-14. The cells seeded on the 10%CB-CaP scaffolds gradually increased in number from day 3 to day 10, while those seeded on AP40mod scaffolds didn't show a significant growth in the first five days, but grew rapidly from day 5 to day 10 (Figure 6-14a). Although no significant differences between the two pore geometries are observed in

terms of cell proliferation, there are differences in terms of metabolic activity. Indeed, all samples show a decrease in metabolic activity over time, but this seems to be statistically significant only for gradient-pores scaffolds (Figure 6-14a). Moreover, this decrease in metabolic activity is more evident for scaffolds containing the CB-derived nanopowder.

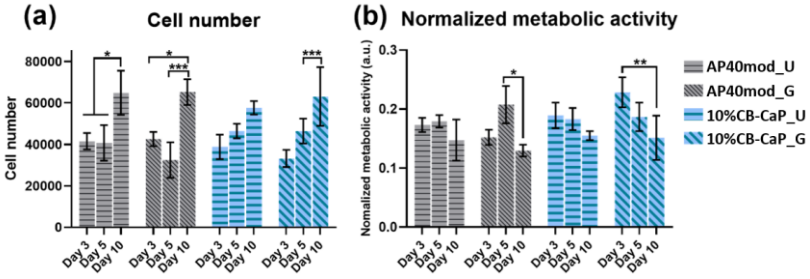

Figure 6-14 Cell number (a) and metabolic activity (b) after 3, 5 and 10 days of culture on the sintered scaffolds. U = uniform pores; G = gradient pores.

The images that show the cell distribution on the scaffolds' surface (Figure 6-15) and their migration in the 3D structure (Figure 6-16) are consistent with the results of the cell proliferation assay. In general, the adhesion was fast on all samples, as the cells cover all the surface except the pores after 3 days of culture. On the other hand, at day 10, the cells created a monolayer on the surface that was able to cover also some small pores, i.e. all pores of uniform size and the smallest of the gradient-size ones (Figure 6-15). Moreover, as visible in Figure 6-16, the cells were able to penetrate the pores and colonize the 3D structure of the scaffolds.

In general, the behavior of the cells on the different scaffolds appears very similar. Most probably, 10% of CB-derived nanopowder is not enough to observe significant differences, also because AP40mod already shows a good bioactivity. However, the presence of CB-derived nanopowder and of gradient pores seems to have an influence on the metabolic activity, which is decreasing after 10 days. As reported in the literature [211], this phenomenon could be a sign of the differentiation of stem cells, but more tests are needed to verify this hypothesis. Indeed, stem cells differentiation tests on these scaffolds are currently in plan at the University of Trento.

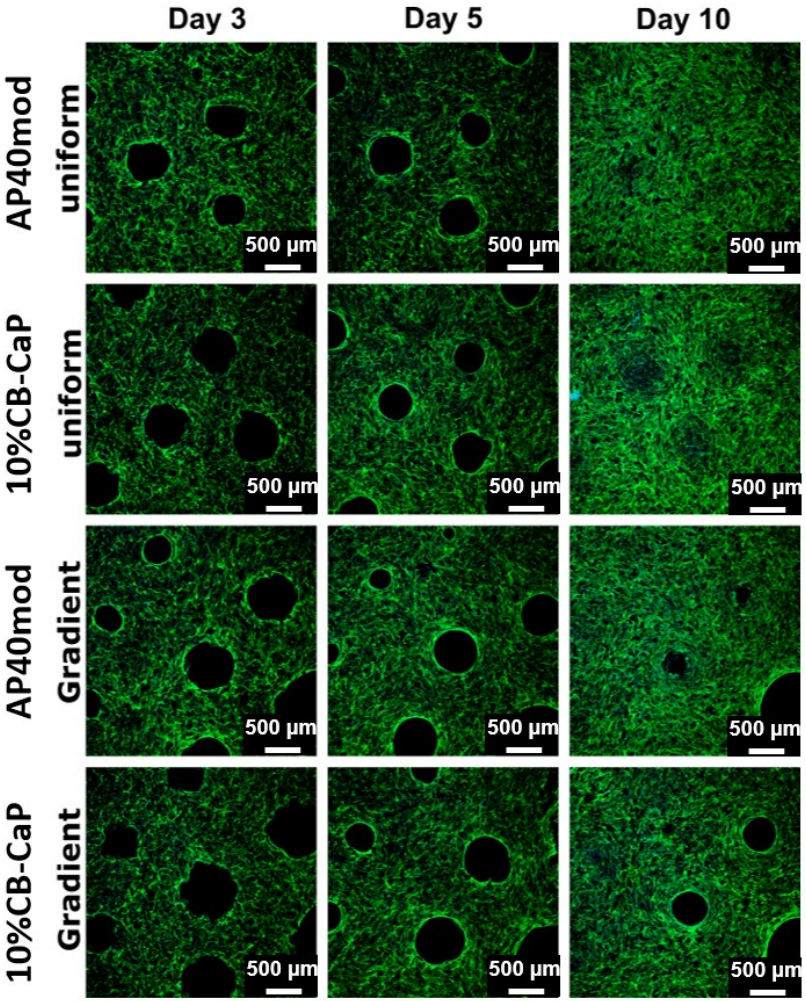

Figure 6-15 Confocal images of the cells on the scaffolds' surface. Cytoskeleton is highlighted in green and cell nuclei in blue.

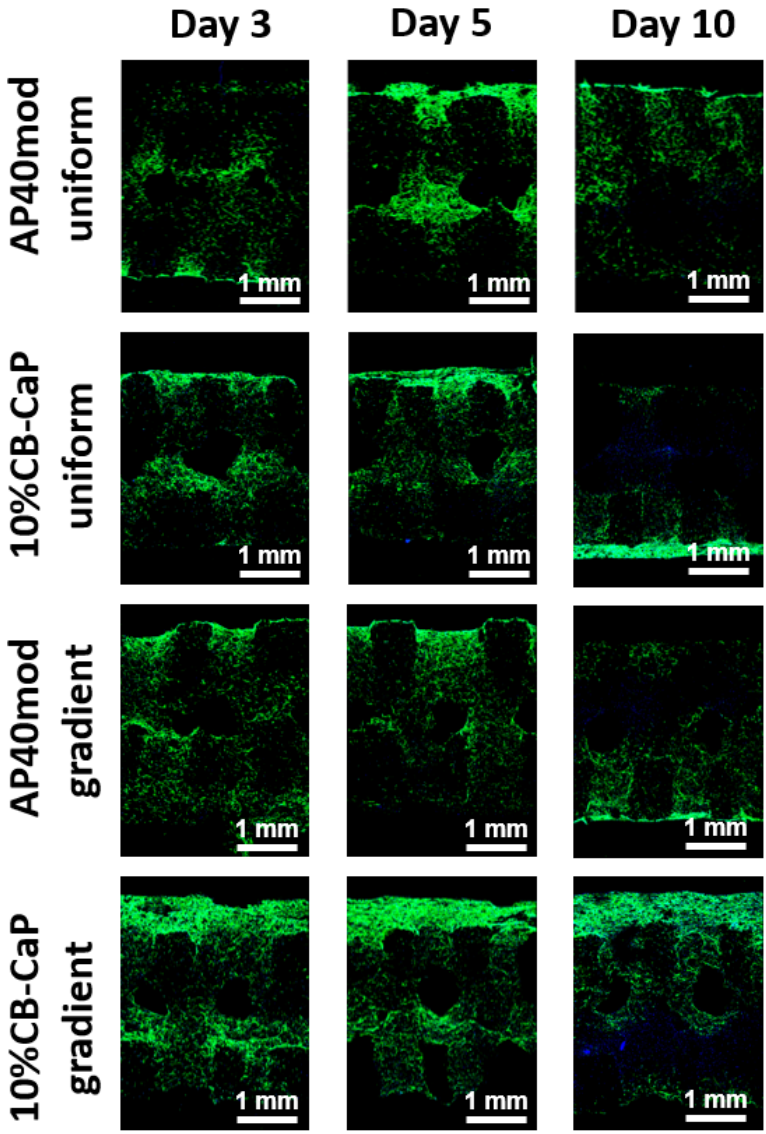

Figure 6-16 Confocal images of the cells in the scaffolds' cross-section. Cytoskeleton is highlighted in green and cell nuclei in blue.

6.4 Conclusions

Cuttlebone-derived biphasic calcium phosphate (BCP) was used to fabricate porous scaffolds by binder jetting 3D printing. Due to the nanometric size of the powder, it was not possible to print the powder as-is, therefore it was mixed with a glass-ceramic powder with particle size 45-100 μm, called AP40mod. The maximum amount of CB-derived powder that was possible to be printed together with the glass-ceramic was 10 wt%. In addition, two pores geometries were designed and printed: with pores of uniform size or with a size-gradient.

After sintering, the scaffolds were composed by mainly hydroxyapatite and wollastonite, their relative quantity being different when the cuttlebone-derived nanopowder was added, since BCP converted into HA during sintering. Diopside, titanite and cristobalite were also present in smaller amounts. The total porosity was ~60% for the pure AP40mod scaffolds and ~70% for the ones containing CB-derived nanopowder. Most probably, the nanosized particles limited the mutual contact of the big glassy particles by surrounding them, slowing down the densification.

The biological *in vitro* tests showed good cell adhesion and proliferation of human mesenchymal stem cells (hMSCs) on all samples, and no significant differences were observed between different materials and different geometries. Moreover, in all samples, the cells were able to penetrate the pores colonizing the porous 3D structure. The metabolic activity showed a gradual decrease over time, which was particularly significant for the scaffolds with CB-derived powder and size-gradient pores. This might be a sign of the differentiation of stem cells, but additional tests are needed to clarify this point.

Scientific production

F. Cestari, G. Chemello, A. Galotta, V.M. Sglavo, Low-temperature synthesis of nanometric apatite from biogenic sources, Ceram. Int. (2020). doi:https://doi.org/10.1016/j.ceramint.2020.06.123.

F. Cestari, F. Agostinacchio, A. Galotta, G. Chemello, A. Motta, V.M. Sglavo, Nano-hydroxyapatite derived from biogenic and bioinspired calcium carbonates: Synthesis and in vitro bioactivity, Nanomaterials. 11 (2021) 1–14. doi:10.3390/nano11020264.

M. Biesuz, F. Valentini, M. Bortolotti, A. Zambotti, F. Cestari, A. Bruni, V.M. Sglavo, G.D. Sorarù, A. Dorigato, A. Pegoretti, Biogenic architectures for green, cheap, and efficient thermal energy storage and management, Renew. Energy. 178 (2021) 96–107. doi:10.1016/j.renene.2021.06.068.

F. Cestari, M. Petretta, Y. Yang, A. Motta, B. Grigolo, V.M. Sglavo, 3D printing of PCL / nano-hydroxyapatite scaffolds derived from biogenic sources for bone tissue engineering, Sustain. Mater. Technol. 29 (2021) e00318. doi:10.1016/j.susmat.2021.e00318.

F. Cestari, Y. Yang, J. Wilbig, J. Günster, A. Motta, V.M. Sglavo, Powder 3D Printing of Bone Scaffolds with Uniform and Gradient Pore Sizes Using Cuttlebone-Derived Calcium Phosphate and Glass-Ceramic, Materials (Basel). 15 (2022). doi:10.3390/ma15155139.

Participation to congresses, schools and workshops

26-30 November 2018: participation to the Winter School MAUD; Materials Characterization by the Combined Analysis and Raw Materials Applications.

16-20 June 2019: participation to the XVI ECerS Conference with an oral presentation with the title: «Innovative synthesis of hydroxyapatite from biogenic calcium carbonate sources».

2-6 December 2019: participation to the Winter School ECOPADS, from linear to circular thinking.

14-16 September 2020: participation to the Summer School Electric and Magnetic Field Processing of Inorganic Materials.

26-27 October 2020: participation to the ECerS School on Additive Manufacturing of Ceramics.

Other activities

From February to June 2019: tutor for the laboratory activity of the course in Glass Engineering of the University of Trento (Materials and Production Engineering master course).

Collaboration with the master students Anna Galotta and Giovanni Chemello for their master thesis projects. They both graduated on the 23rd October 2019.

From October to December 2019: tutor for the laboratory activity of the course in Ceramic Materials Engineering (Materials and Production Engineering master course).

Bibliography

[1] K.D. Poss, Advances in understanding tissue regenerative capacity and mechanisms in animals, Nat. Rev. Genet. 11 (2010) 710–722. doi:10.1038/nrg2879.

[2] T.S.N. Chen, P.S.Y. Chen, The myth of prometheus and the liver, J. R. Soc. Med. 87 (1994) 754–755.

[3] C. Trautwein, Liver Regeneration, Zakim Boyer's Hepatol. 276 (2006) 23–36. doi:10.1016/B978-1-4160-3258-8.50007-3.

[4] G.L. Koons, M. Diba, A.G. Mikos, Materials design for bone-tissue engineering, Nat. Rev. Mater. 5 (2020) 584–603. doi:10.1038/s41578-020-0204-2.

[5] K. Kerényi, Gli dèi e gli eroi della Grecia. Il racconto del mito, la nascita della civiltà, Il Saggiatore, 2015.

[6] D. Donati, C. Zolezzi, P. Tomba, A. Viganò, Bone grafting: Historical and conceptual review, starting with an old manuscript by Vittorio Putti, Acta Orthop. 78 (2007) 19–25. doi:10.1080/17453670610013376.

[7] A. Oryan, S. Alidadi, A. Moshiri, N. Maffulli, Bone regenerative medicine: Classic options, novel strategies, and future directions, J. Orthop. Surg. Res. 9 (2014) 1–27. doi:10.1186/1749-799X-9-18.

[8] L. Roseti, V. Parisi, M. Petretta, C. Cavallo, G. Desando, I. Bartolotti, B. Grigolo, Scaffolds for Bone Tissue Engineering: State of the art and new perspectives, Mater. Sci. Eng. C. 78 (2017) 1246–1262. doi:10.1016/J.MSEC.2017.05.017.

[9] J. Henkel, M.A. Woodruff, D.R. Epari, R. Steck, V. Glatt, I.C. DIckinson, P.F.M. Choong, M.A. Schuetz, Di.W. Hutmacher, Bone

Regeneration Based on Tissue Engineering Conceptions-A 21st Century Perspective, Bone Res. 1 (2013) 216–248. doi:10.4248/BR201303002.

[10] E. Solheim, Growth factors in bone, Int. Orthop. 22 (1998) 410–416. doi:10.1007/s002640050290.

[11] K. Hing, Biomimetic bone regeneration, in: Biomim. Biomater. Struct. Appl., 2013: pp. 207–237. doi:10.1533/9780857098887.2.207.

[12] M.A. Meyers, P.-Y. Chen, Calcium-phosphate-based composites, in: Biol. Mater. Sci., Cambridge University Press, Cambridge, 2014: pp. 223–291. doi:10.1017/CBO9780511862397.010.

[13] N. Eliaz, N. Metoki, Calcium phosphate bioceramics: A review of their history, structure, properties, coating technologies and biomedical applications, Materials (Basel). 10 (2017). doi:10.3390/ma10040334.

[14] D.L. Kopperdahl, E.F. Morgan, T.M. Keaveny, Quantitative computed tomography estimates of the mechanical properties of human vertebral trabecular bone, J. Orthop. Res. 20 (2002) 801–805. doi:10.1016/S0736-0266(01)00185-1.

[15] T.A. Burgers, J. Mason, G. Niebur, H.L. Ploeg, Compressive properties of trabecular bone in the distal femur, J. Biomech. 41 (2008) 1077–1085. doi:10.1016/J.JBIOMECH.2007.11.018.

[16] C. Öhman, M. Baleani, C. Pani, F. Taddei, M. Alberghini, M. Viceconti, M. Manfrini, Compressive behaviour of child and adult cortical bone, Bone. 49 (2011) 769–776. doi:10.1016/j.bone.2011.06.035.

[17] P. Fratzl, R. Weinkamer, Nature's hierarchical materials, Prog. Mater. Sci. 52 (2007) 1263–1334. doi:10.1016/j.pmatsci.2007.06.001.

[18] J.Y. Rho, L. Kuhn-Spearing, P. Zioupos, Mechanical properties and

the hierarchical structure of bone, Med. Eng. Phys. 20 (1998) 92–102. doi:10.1016/S1350-4533(98)00007-1.

[19] T. Hassenkam, G.E. Fantner, J.A. Cutroni, J.C. Weaver, D.E. Morse, P.K. Hansma, High-resolution AFM imaging of intact and fractured trabecular bone, Bone. 35 (2004) 4–10. doi:10.1016/j.bone.2004.02.024.

[20] D.J. Hadjidakis, I.I. Androulakis, Bone remodeling, Ann. N. Y. Acad. Sci. 1092 (2006) 385–396. doi:10.1196/annals.1365.035.

[21] G. Turnbull, J. Clarke, F. Picard, P. Riches, L. Jia, F. Han, B. Li, W. Shu, 3D bioactive composite scaffolds for bone tissue engineering, Bioact. Mater. 3 (2018) 278–314. doi:10.1016/J.BIOACTMAT.2017.10.001.

[22] D.W. Hutmacher, Scaffolds in tissue engineering bone and cartilage, Biomater. Silver Jubil. Compend. 21 (2000) 175–189. doi:10.1016/B978-008045154-1.50021-6.

[23] L. Zhang, G. Yang, B.N. Johnson, X. Jia, Three-dimensional (3D) printed scaffold and material selection for bone repair, Acta Biomater. 84 (2019) 16–33. doi:10.1016/J.ACTBIO.2018.11.039.

[24] J.L. Dávila, M.S. Freitas, P. Inforçatti Neto, Z.C. Silveira, J.V.L. Silva, M.A. D'Ávila, Fabrication of PCL/β-TCP scaffolds by 3D mini-screw extrusion printing, J. Appl. Polym. Sci. 133 (2016) 1–9. doi:10.1002/app.43031.

[25] B. Huang, G. Caetano, C. Vyas, J.J. Blaker, C. Diver, P. Bártolo, Polymer-ceramic composite scaffolds: The effect of hydroxyapatite and β-tri-calcium phosphate, Materials (Basel). 11 (2018). doi:10.3390/ma11010129.

[26] Y. Li, C. Liao, S.C. Tjong, Synthetic biodegradable aliphatic polyester nanocomposites reinforced with nanohydroxyapatite and/or graphene oxide for bone tissue engineering applications,

Nanomaterials. 9 (2019). doi:10.3390/nano9040590.

[27] F.S. Senatov, K.V. Niaza, M.Y. Zadorozhnyy, A.V. Maksimkin, S.D. Kaloshkin, Y.Z. Estrin, Mechanical properties and shape memory effect of 3D-printed PLA-based porous scaffolds, J. Mech. Behav. Biomed. Mater. 57 (2016) 139–148. doi:10.1016/J.JMBBM.2015.11.036.

[28] F.S. Senatov, K.V. Niaza, A.A. Stepashkin, S.D. Kaloshkin, Low-cycle fatigue behavior of 3d-printed PLA-based porous scaffolds, Compos. Part B Eng. 97 (2016) 193–200. doi:10.1016/J.COMPOSITESB.2016.04.067.

[29] K. V. Niaza, F.S. Senatov, S.D. Kaloshkin, A. V. Maksimkin, D.I. Chukov, 3D-printed scaffolds based on PLA/HA nanocomposites for trabecular bone reconstruction, J. Phys. Conf. Ser. 741 (2016). doi:10.1088/1742-6596/741/1/012068.

[30] S.A. Park, S.H. Lee, W.D. Kim, Fabrication of porous polycaprolactone/hydroxyapatite (PCL/HA) blend scaffolds using a 3D plotting system for bone tissue engineering, Bioprocess Biosyst. Eng. 34 (2011) 505–513. doi:10.1007/s00449-010-0499-2.

[31] D. Ronca, F. Langella, M. Chierchia, U. D'Amora, T. Russo, M. Domingos, A. Gloria, P. Bartolo, L. Ambrosio, Bone Tissue Engineering: 3D PCL-based Nanocomposite Scaffolds with Tailored Properties, Procedia CIRP. 49 (2016) 51–54. doi:10.1016/J.PROCIR.2015.07.028.

[32] D. Liu, W. Nie, D. Li, W. Wang, L. Zheng, J. Zhang, J. Zhang, C. Peng, X. Mo, C. He, 3D printed PCL/SrHA scaffold for enhanced bone regeneration, Chem. Eng. J. 362 (2019) 269–279. doi:10.1016/J.CEJ.2019.01.015.

[33] S. V. Dorozhkin, Calcium orthophosphates: occurrence, properties,

biomineralization, pathological calcification and biomimetic applications., Biomatter. 1 (2011) 121–164. doi:10.4161/biom.18790.

[34] S.V.D. and M. Epple, Biological and Medical Significance of Calcium Phosphates, Angew. Chemie - Int. Ed. 41 (2002) 3213–3215. doi:10.1002/1521-3773(20020902)41.

[35] S. V. Dorozhkin, Bioceramics of calcium orthophosphates, Biomaterials. 31 (2010) 1465–1485. doi:10.1016/J.BIOMATERIALS.2009.11.050.

[36] M. Yashima, A. Sakai, High-temperature neutron powder diffraction study of the structural phase transition between α and α′ phases in tricalcium phosphate Ca3(PO4)2, Chem. Phys. Lett. 372 (2003) 779–783. doi:10.1016/S0009-2614(03)00505-0.

[37] N. Rangavittal, A.R. Landa-Cánovas, J.M. González-Calbet, M. Vallet-Regí, Structural study and stability of hydroxyapatite and β-tricalcium phosphate: Two important bioceramics, J. Biomed. Mater. Res. 51 (2000) 660–668. doi:10.1002/1097-4636(20000915)51:4<660::AID-JBM14>3.0.CO;2-B.

[38] K.A. Gross, C.C. Berndt, Thermal processing of hydroxyapatite for coating production, J. Biomed. Mater. Res. 39 (1998) 580–587. doi:10.1002/(SICI)1097-4636(19980315)39:4<580::AID-JBM12>3.0.CO;2-B.

[39] S. Serena, L. Carbajal, M.A. Sainz, A. Caballero, Thermodynamic assessment of the system CaO-P2O5: Application of the ionic two-sublattice model to glass-forming melts, J. Am. Ceram. Soc. 94 (2011) 3094–3103. doi:10.1111/j.1551-2916.2011.04445.x.

[40] D.W. Kim, J.S. An, I.S. Cho, Effects of Mg and Sr co-addition on the densification and biocompatible properties of calcium

pyrophosphate, Ceram. Int. 44 (2018) 9689–9695. doi:10.1016/j.ceramint.2018.02.198.

[41] R.Z. LeGeros, J.P. LeGeros, Phosphate minerals in human tissues, in: Phosphate Miner., 1984: pp. 351–385. doi:10.1007/978-3-642-61736-2_12.

[42] K. Lin, J. Chang, Structure and properties of hydroxyapatite for biomedical applications, in: Hydroxyapatite Biomed. Appl., Elsevier Ltd., 2015: pp. 3–19. doi:10.1016/b978-1-78242-033-0.00001-8.

[43] E.I. Dorozhkina, S. V. Dorozhkin, Mechanism of the solid-state transformation of a calcium-deficient hydroxyapatite (CDHA) into biphasic calcium phosphate (BCP) at elevated temperatures, Chem. Mater. 14 (2002) 4267–4272. doi:10.1021/cm0203060.

[44] N.C. Blumenthal, F. Betts, A.S. Posner, Formation and structure of Ca-deficient hydroxyapatite, Calcif. Tissue Int. 33 (1981) 111–117. doi:10.1007/BF02409422.

[45] T.. Feenstra, P.. De Bruyn, The ostwald rule of stages in precipitation from highly supersaturated solutions: a model and its application to the formation of the nonstoichiometric amorphous calcium phosphate precursor phase, J. Colloid Interface Sci. 84 (1981) 66–72. doi:10.1016/0021-9797(81)90260-5.

[46] R. Gelli, F. Ridi, P. Baglioni, The importance of being amorphous: calcium and magnesium phosphates in the human body, Adv. Colloid Interface Sci. 269 (2019) 219–235. doi:10.1016/j.cis.2019.04.011.

[47] F. Betts, A.S. Posner, An X-ray radial distribution study of amorphous calcium phosphate, Mater. Res. Bull. 9 (1974) 353–360. doi:https://doi.org/10.1016/0025-5408(74)90087-7.

[48] N. Kanzaki, G. Treboux, K. Onuma, S. Tsutsumi, A. Ito, Calcium

phosphate clusters, Biomaterials. 22 (2001) 2921–2929. doi:https://doi.org/10.1016/S0142-9612(01)00039-4.

[49] J. Zhao, Y. Liu, W. Bin Sun, H. Zhang, Amorphous calcium phosphate and its application in dentistry, Chem. Cent. J. 5 (2011) 1–7. doi:10.1186/1752-153X-5-40.

[50] C. Rey, B. Collins, T. Goehl, I.R. Dickson, M.J. Glimcher, The carbonate environment in bone mineral: A resolution-enhanced fourier transform infrared spectroscopy study, Calcif. Tissue Int. 45 (1989) 157–164. doi:10.1007/BF02556059.

[51] V. Aina, G. Lusvardi, B. Annaz, I.R. Gibson, F.E. Imrie, G. Malavasi, L. Menabue, G. Cerrato, G. Martra, Magnesium- and strontium-co-substituted hydroxyapatite: the effects of doped-ions on the structure and chemico-physical properties, J. Mater. Sci. Mater. Med. 23 (2012) 2867–2879. doi:10.1007/s10856-012-4767-3.

[52] F. Scalera, B. Palazzo, A. Barca, F. Gervaso, Sintering of magnesium-strontium doped hydroxyapatite nanocrystals: Towards the production of 3D biomimetic bone scaffolds, J. Biomed. Mater. Res. - Part A. 108 (2020) 633–644. doi:10.1002/jbm.a.36843.

[53] I.R. De Lima, G.G. Alves, C.A. Soriano, A.P. Campaneli, T.H. Gasparoto, E.S. Ramos, L.Á. De Sena, A.M. Rossi, J.M. Granjeiro, Understanding the impact of divalent cation substitution on hydroxyapatite: An in vitro multiparametric study on biocompatibility, J. Biomed. Mater. Res. - Part A. 98 A (2011) 351–358. doi:10.1002/jbm.a.33126.

[54] E. Landi, J. Uggeri, V. Medri, S. Guizzardi, Sr, Mg cosubstituted HA porous macro-granules: Potentialities as resorbable bone filler with antiosteoporotic functions, J. Biomed. Mater. Res. - Part A. 101 A

(2013) 2481–2490. doi:10.1002/jbm.a.34553.

[55] A. Farzadi, F. Bakhshi, M. Solati-Hashjin, M. Asadi-Eydivand, N.A. abu Osman, Magnesium incorporated hydroxyapatite: Synthesis and structural properties characterization, Ceram. Int. 40 (2014) 6021–6029. doi:10.1016/J.CERAMINT.2013.11.051.

[56] S. Kannan, F. Goetz-Neunhoeffer, J. Neubauer, J.M.F. Ferreira, Ionic substitutions in biphasic hydroxyapatite and β-tricalcium phosphate mixtures: Structural analysis by rietveld refinement, J. Am. Ceram. Soc. 91 (2008) 1–12. doi:10.1111/j.1551-2916.2007.02117.x.

[57] Z. Saidak, P.J. Marie, Strontium signaling: Molecular mechanisms and therapeutic implications in osteoporosis, Pharmacol. Ther. 136 (2012) 216–226. doi:https://doi.org/10.1016/j.pharmthera.2012.07.009.

[58] D. Pierantozzi, A. Scalzone, S. Jindal, L. Stīpniece, K. Šalma-Ancāne, K. Dalgarno, P. Gentile, E. Mancuso, 3D printed Sr-containing composite scaffolds: Effect of structural design and material formulation towards new strategies for bone tissue engineering, Compos. Sci. Technol. 191 (2020) 108069. doi:10.1016/J.COMPSCITECH.2020.108069.

[59] A. Hoppe, N.S. Güldal, A.R. Boccaccini, A review of the biological response to ionic dissolution products from bioactive glasses and glass-ceramics, Biomaterials. 32 (2011) 2757–2774. doi:10.1016/j.biomaterials.2011.01.004.

[60] C.D. Ghiţulică, A. Cucuruz, G. Voicu, A.T. Cucuruz, S. Dinescu, A. Selaru, M. Costache, Ceramics based on calcium phosphates substituted with magnesium ions for bone regeneration, Int. J. Appl. Ceram. Technol. 17 (2020) 342–353. doi:10.1111/ijac.13333.

[61] S. Yoshizawa, A. Brown, A. Barchowsky, C. Sfeir, Magnesium ion

stimulation of bone marrow stromal cells enhances osteogenic activity, simulating the effect of magnesium alloy degradation, Acta Biomater. 10 (2014) 2834–2842. doi:https://doi.org/10.1016/j.actbio.2014.02.002.

[62] M. Akram, R. Ahmed, I. Shakir, W.A.W. Ibrahim, R. Hussain, Extracting hydroxyapatite and its precursors from natural resources, J. Mater. Sci. 49 (2014) 1461–1475. doi:10.1007/s10853-013-7864-x.

[63] K.K. Gómez-Lizárraga, C. Flores-Morales, M.L. Del Prado-Audelo, M.A. Álvarez-Pérez, M.C. Piña-Barba, C. Escobedo, Polycaprolactone- and polycaprolactone/ceramic-based 3D-bioplotted porous scaffolds for bone regeneration: A comparative study, Mater. Sci. Eng. C. 79 (2017) 326–335. doi:10.1016/J.MSEC.2017.05.003.

[64] P. Terzioğlu, H. Öğüt, A. Kalemtaş, Natural calcium phosphates from fish bones and their potential biomedical applications, Mater. Sci. Eng. C. 91 (2018) 899–911. doi:10.1016/J.MSEC.2018.06.010.

[65] M. Boutinguiza, J. Pou, R. Comesaña, F. Lusquiños, A. de Carlos, B. León, Biological hydroxyapatite obtained from fish bones, Mater. Sci. Eng. C. 32 (2012) 478–486. doi:10.1016/J.MSEC.2011.11.021.

[66] C. Piccirillo, M.F. Silva, R.C. Pullar, I. Braga da Cruz, R. Jorge, M.M.E. Pintado, P.M.L. Castro, Extraction and characterisation of apatite- and tricalcium phosphate-based materials from cod fish bones, Mater. Sci. Eng. C. 33 (2013) 103–110. doi:10.1016/J.MSEC.2012.08.014.

[67] S. Mondal, U. Pal, A. Dey, Natural origin hydroxyapatite scaffold as potential bone tissue engineering substitute, Ceram. Int. 42 (2016) 18338–18346. doi:10.1016/J.CERAMINT.2016.08.165.

[68] B. Ben-Nissan, A.H. Choi, D.W. Green, Marine Derived Biomaterials

for Bone Regeneration and Tissue Engineering: Learning from Nature, Springer Singapore, 2019. doi:10.1007/978-981-13-8855-2_3.

[69] S.A. Clarke, P. Walsh, Marine organisms for bone repair and regeneration, in: Bone Substit. Biomater., Woodhead Publishing, 2014: pp. 294–318. doi:10.1533/9780857099037.3.294.

[70] S. Ramesh, A.N. Natasha, C.Y. Tan, L.T. Bang, S. Ramesh, C.Y. Ching, H. Chandran, Direct conversion of eggshell to hydroxyapatite ceramic by a sintering method, Ceram. Int. 42 (2016) 7824–7829. doi:10.1016/J.CERAMINT.2016.02.015.

[71] D. Roy, S.K. Linnehan, Hydroxyapatite formed from Coral Skeletal Carbonate by Hydrothermal Exchange, Nature. 247 (1974) 220–222.

[72] E. Tkalčec, J. Popović, S. Orlić, S. Milardović, H. Ivanković, Hydrothermal synthesis and thermal evolution of carbonate-fluorhydroxyapatite scaffold from cuttlefish bones, Mater. Sci. Eng. C. 42 (2014) 578–586. doi:10.1016/J.MSEC.2014.05.079.

[73] J. Hu, J.J. Russell, B. Ben-Nissan, R. Vago, Production and analysis of hydroxyapatite from Australian corals via hydrothermal process, J. Mater. Sci. Lett. 20 (2001) 85–87. doi:10.1023/A:1006735319725.

[74] Y. Xu, D. Wang, L. Yang, H. Tang, Hydrothermal conversion of coral into hydroxyapatite, Mater. Charact. 47 (2001) 83–87. doi:10.1016/S1044-5803(01)00154-1.

[75] Y.H. Kim, H. Song, D.H. Riu, S.R. Kim, H.J. Kim, J.H. Moon, Preparation of porous Si-incorporated hydroxyapatite, Curr. Appl. Phys. 5 (2005) 538–541. doi:10.1016/J.CAP.2005.01.031.

[76] J.H.G. Rocha, A.F. Lemos, S. Agathopoulos, P. Valério, S. Kannan, F.N. Oktar, J.M.F. Ferreira, Scaffolds for bone restoration from cuttlefish, Bone. 37 (2005) 850–857. doi:10.1016/j.bone.2005.06.018.

[77] H. Ivankovic, G. Gallego Ferrer, E. Tkalcec, S. Orlic, M. Ivankovic, Preparation of highly porous hydroxyapatite from cuttlefish bone, J. Mater. Sci. Mater. Med. 20 (2009) 1039–1046. doi:10.1007/s10856-008-3674-0.

[78] H. Ivankovic, E. Tkalcec, S. Orlic, G. Gallego Ferrer, Z. Schauperl, Hydroxyapatite formation from cuttlefish bones: Kinetics, J. Mater. Sci. Mater. Med. 21 (2010) 2711–2722. doi:10.1007/s10856-010-4115-4.

[79] J.H.G. Rocha, A.F. Lemos, S. Kannan, S. Agathopoulos, J.M.F. Ferreira, Hydroxyapatite scaffolds hydrothermally grown from aragonitic cuttlefish bones, J. Mater. Chem. 15 (2005) 5007–50011. doi:10.1016/j.actbio.2006.09.006.

[80] S. Kannan, J.H.G. Rocha, S. Agathopoulos, J.M.F. Ferreira, Fluorine-substituted hydroxyapatite scaffolds hydrothermally grown from aragonitic cuttlefish bones, Acta Biomater. 3 (2007) 243–249. doi:10.1016/J.ACTBIO.2006.09.006.

[81] A.F. Lemos, J.H.G. Rocha, S.S.F. Quaresma, S. Kannan, F.N. Oktar, S. Agathopoulos, J.M.F. Ferreira, Hydroxyapatite nano-powders produced hydrothermally from nacreous material, J. Eur. Ceram. Soc. 26 (2006) 3639–3646. doi:10.1016/J.JEURCERAMSOC.2005.12.011.

[82] Y. Yang, Q. Yao, X. Pu, Z. Hou, Q. Zhang, Biphasic calcium phosphate macroporous scaffolds derived from oyster shells for bone tissue engineering, Chem. Eng. J. 173 (2011) 837–845. doi:10.1016/J.CEJ.2011.07.029.

[83] K.S. Vecchio, X. Zhang, J.B. Massie, M. Wang, C.W. Kim, Conversion of sea urchin spines to Mg-substituted tricalcium phosphate for bone implants, Acta Biomater. 3 (2007) 785–793. doi:10.1016/j.actbio.2007.03.009.

[84] M. Sivakumar, T.S.S. Kumar, K.L. Shantha, K.P. Rao, Development of hydroxyapatite derived from Indian coral, Biomaterials. 17 (1996) 1709–1714. doi:10.1016/0142-9612(96)87651-4.

[85] E.M. Rivera, M. Araiza, W. Brostow, V.M. Castaño, J.. Diaz-Estrada, R. Hernández, J.R. Rodriguez, Synthesis of hydroxyapatite from eggshells, Mater. Lett. 41 (1999) 128–134. doi:10.1016/S0167-577X(99)00118-4.

[86] P.J. Walsh, F.J. Buchanan, M. Dring, C. Maggs, S. Bell, G.M. Walker, Low-pressure synthesis and characterisation of hydroxyapatite derived from mineralise red algae, Chem. Eng. J. 137 (2008) 173–179. doi:10.1016/J.CEJ.2007.10.016.

[87] F. Kusmanto, G. Walker, Q. Gan, P. Walsh, F. Buchanan, G. Dickson, M. McCaigue, C. Maggs, M. Dring, Development of composite tissue scaffolds containing naturally sourced mircoporous hydroxyapatite, Chem. Eng. J. 139 (2008) 398–407. doi:10.1016/J.CEJ.2007.11.041.

[88] S. Jinawath, D. Polchai, M. Yoshimura, Low-temperature, hydrothermal transformation of aragonite to hydroxyapatite, Mater. Sci. Eng. C. 22 (2002) 35–39. doi:10.1016/S0928-4931(02)00110-8.

[89] R. Murugan, S. Ramakrishna, Crystallographic study of hydroxyapatite bioceramics derived from various sources, Cryst. Growth Des. 5 (2005) 111–112. doi:10.1021/cg034227s.

[90] S.-C. Wu, H.-C. Hsu, S.-K. Hsu, C.-P. Tseng, W.-F. Ho, Preparation and characterization of hydroxyapatite synthesized from oyster shell powders, Elsevier, 2017. doi:10.1016/J.APT.2017.02.001.

[91] P. Álvarez-Lloret, A.B. Rodríguez-Navarro, G. Falini, S. Fermani, M. Ortega-Huertas, Crystallographic control of the hydrothermal conversion of calcitic sea urchin spine (Paracentrotus lividus) into

apatite, Cryst. Growth Des. 10 (2010) 5227–5232. doi:10.1021/cg101012a.

[92] S.-C. Wu, H.-K. Tsou, H.-C. Hsu, S.-K. Hsu, S.-P. Liou, W.-F. Ho, A hydrothermal synthesis of eggshell and fruit waste extract to produce nanosized hydroxyapatite, Ceram. Int. 39 (2013) 8183–8188. doi:10.1016/J.CERAMINT.2013.03.094.

[93] B. Chaudhuri, B. Mondal, D.K. Modak, K. Pramanik, B.K. Chaudhuri, Preparation and characterization of nanocrystalline hydroxyapatite from egg shell and K2HPO4 solution, Mater. Lett. 97 (2013) 148–150. doi:10.1016/J.MATLET.2013.01.082.

[94] S. Nayar, A. Guha, Waste utilization for the controlled synthesis of nanosized hydroxyapatite, Mater. Sci. Eng. C. 29 (2009) 1326–1329. doi:10.1016/J.MSEC.2008.10.002.

[95] K.P. Sanosh, M.-C. Chu, A. Balakrishnan, T.N. Kim, S.-J. Cho, Utilization of biowaste eggshells to synthesize nanocrystalline hydroxyapatite powders, Mater. Lett. 63 (2009) 2100–2102. doi:10.1016/J.MATLET.2009.06.062.

[96] D.L. Goloshchapov, V.M. Kashkarov, N.A. Rumyantseva, P.V. Seredin, A.S. Lenshin, B.L. Agapov, E.P. Domashevskaya, Synthesis of nanocrystalline hydroxyapatite by precipitation using hen's eggshell, Ceram. Int. 39 (2013) 4539–4549. doi:10.1016/J.CERAMINT.2012.11.050.

[97] S. Rujitanapanich, P. Kumpapan, P. Wanjanoi, Synthesis of Hydroxyapatite from Oyster Shell via Precipitation, Energy Procedia. 56 (2014) 112–117. doi:10.1016/J.EGYPRO.2014.07.138.

[98] S.M. dePaula, M.F.G. Huila, K. Araki, H.E. Toma, Confocal Raman and electronic microscopy studies on the topotactic conversion of

calcium carbonate from Pomacea lineate shells into hydroxyapatite bioceramic materials in phosphate media, Micron. 41 (2010) 983–989. doi:10.1016/J.MICRON.2010.06.014.

[99] D. Siva Rama Krishna, A. Siddharthan, S.K. Seshadri, T.S. Sampath Kumar, A novel route for synthesis of nanocrystalline hydroxyapatite from eggshell waste, J. Mater. Sci. Mater. Med. 18 (2007) 1735–1743. doi:10.1007/s10856-007-3069-7.

[100] G.S. Kumar, A. Thamizhavel, E.K. Girija, Microwave conversion of eggshells into flower-like hydroxyapatite nanostructure for biomedical applications, Mater. Lett. 76 (2012) 198–200. doi:10.1016/J.MATLET.2012.02.106.

[101] A. Shavandi, A.E.-D.A. Bekhit, A. Ali, Z. Sun, Synthesis of nano-hydroxyapatite (nHA) from waste mussel shells using a rapid microwave method, Mater. Chem. Phys. 149–150 (2015) 607–616. doi:10.1016/J.MATCHEMPHYS.2014.11.016.

[102] G.S. Kumar, E.K. Girija, M. Venkatesh, G. Karunakaran, E. Kolesnikov, D. Kuznetsov, One step method to synthesize flower-like hydroxyapatite architecture using mussel shell bio-waste as a calcium source, Ceram. Int. 43 (2017) 3457–3461. doi:10.1016/J.CERAMINT.2016.11.163.

[103] P. Baláž, M. Achimovicová, M. Baláž, P. Billik, C.Z. Zara, J.M. Criado, F. Delogu, E. Dutková, E. Gaffet, F.J. Gotor, R. Kumar, I. Mitov, T. Rojac, M. Senna, A. Streletskii, W.C. Krystyna, Hallmarks of mechanochemistry: From nanoparticles to technology, Chem. Soc. Rev. 42 (2013) 7571–7637. doi:10.1039/c3cs35468g.

[104] S.J. Lee, S.H. Oh, Fabrication of calcium phosphate bioceramics by using eggshell and phosphoric acid, Mater. Lett. 57 (2003) 4570–4574.

doi:10.1016/S0167-577X(03)00363-X.

[105] C. Balázsi, F. Wéber, Z. Kövér, E. Horváth, C. Németh, Preparation of calcium–phosphate bioceramics from natural resources, J. Eur. Ceram. Soc. 27 (2007) 1601–1606. doi:10.1016/J.JEURCERAMSOC.2006.04.016.

[106] G. Gergely, F. Wéber, I. Lukács, A.L. Tóth, Z.E. Horváth, J. Mihály, C. Balázsi, Preparation and characterization of hydroxyapatite from eggshell, Ceram. Int. 36 (2010) 803–806. doi:10.1016/J.CERAMINT.2009.09.020.

[107] S.-C. Wu, H.-C. Hsu, S.-K. Hsu, Y.-C. Chang, W.-F. Ho, Effects of heat treatment on the synthesis of hydroxyapatite from eggshell powders, Ceram. Int. 41 (2015) 10718–10724. doi:10.1016/J.CERAMINT.2015.05.006.

[108] A.A. Francis, M.K. Abdel Rahman, The environmental sustainability of calcined calcium phosphates production from the milling of eggshell wastes and phosphoric acid, J. Clean. Prod. 137 (2016) 1432–1438. doi:10.1016/J.JCLEPRO.2016.08.029.

[109] A.A. Hamidi, M.N. Salimi, A.H.M. Yusoff, Synthesis and characterization of eggshell-derived hydroxyapatite via mechanochemical method: A comparative study, AIP Conf. Proc. 1835 (2017). doi:10.1063/1.4981867.

[110] N. Nuamsrinuan, W. Kaewwiset, P. Limsuwan, K. Naemchanthara, Hydroxyapatite Synthesized from Waste Eggshell via Ball Milling, Appl. Mech. Mater. 866 (2017) 12–16. doi:10.4028/www.scientific.net/AMM.866.12.

[111] S.J. Lee, Y.C. Lee, Y.S. Yoon, Characteristics of calcium phosphate powders synthesized from cuttlefish bone and phosphoric acid, J.

Ceram. Process. Res. 8 (2007) 427–430.

[112] N. Cozza, F. Monte, W. Bonani, P. Aswath, A. Motta, C. Migliaresi, Bioactivity and mineralization of natural hydroxyapatite from cuttlefish bone and Bioglass® co-sintered bioceramics, J Tissue Eng Regen Med. (2017) 1–12.

[113] K. Faksawat, W. Kaewwiset, P. Limsuwan, K. Naemchanthara, Comparison of characteristics of hydroxyapatite powders synthesized from cuttlefish bone via precipitation and ball milling techniques, J. Phys. Conf. Ser. 901 (2017). doi:10.1088/1742-6596/901/1/012083.

[114] S.-C. Wu, H.-C. Hsu, Y.-N. Wu, W.-F. Ho, Hydroxyapatite synthesized from oyster shell powders by ball milling and heat treatment, Mater. Charact. 62 (2011) 1180–1187. doi:10.1016/J.MATCHAR.2011.09.009.

[115] A. Pal, S. Maity, S. Chabri, S. Bera, A.R. Chowdhury, M. Das, A. Sinha, Mechanochemical synthesis of nanocrystalline hydroxyapatite from Mercenaria clam shells and phosphoric acid, Biomed. Phys. Eng. Express. 3 (2017) 15010. doi:https://doi.org/10.1088/2057-1976/aa54f5.

[116] S.-C. Wu, H.-C. Hsu, S.-K. Hsu, Y.-C. Chang, W.-F. Ho, Synthesis of hydroxyapatite from eggshell powders through ball milling and heat treatment, J. Asian Ceram. Soc. 4 (2016) 85–90. doi:10.1016/J.JASCER.2015.12.002.

[117] A.C. Ferro, M. Guedes, Mechanochemical synthesis of hydroxyapatite using cuttlefish bone and chicken eggshell as calcium precursors, Mater. Sci. Eng. C. 97 (2019) 124–140. doi:10.1016/J.MSEC.2018.11.083.

[118] D. Chakrabarty, S. Mahapatra, Aragonite crystals with unconventional morphologies, J. Mater. Chem. 9 (1999) 2953–2957. doi:10.1039/a905407c.

[119] J. Perić, M. Vučak, R. Krstulović, L. Brečević, D. Kralj, Phase transformation of calcium carbonate polymorphs, Thermochim. Acta. 277 (1996) 175–186. doi:10.1016/0040-6031(95)02748-3.

[120] C. Tsao, P.T. Yu, C.H. Lo, C.K. Chang, C.H. Wang, Y.W. Yang, J.C.C. Chan, Anhydrous amorphous calcium carbonate (ACC) is structurally different from the transient phase of biogenic ACC, Chem. Commun. 55 (2019) 6946–6949. doi:10.1039/c9cc00518h.

[121] E. Zolotoyabko, E.N. Caspi, J.S. Fieramosca, R.B. Von Dreele, F. Marin, G. Mor, L. Addadi, S. Weiner, Y. Politi, Differences between Bond Lengths in Biogenic and Geological Calcite, Cryst. Growth Des. 10 (2010) 1207–1214. doi:10.1021/cg901195t.

[122] E.N. Caspi, B. Pokroy, P.L. Lee, J.P. Quintana, E. Zolotoyabko, On the structure of aragonite, Acta Crystallogr. Sect. B Struct. Sci. 61 (2005) 129–132. doi:10.1107/S0108768105005240.

[123] A. Le Bail, S. Ouhenia, D. Chateigner, Microtwinning hypothesis for a more ordered vaterite model, Powder Diffr. 26 (2011) 16–21. doi:10.1154/1.3552994.

[124] W.S. Fyfe, J.L. Bischoff, The Calcite-Aragonite Problem, Dolomitization Limestone Diagenes. 13 (1965) 3–13.

[125] D.B. Trushina, T. V. Bukreeva, M. V. Kovalchuk, M.N. Antipina, CaCO3 vaterite microparticles for biomedical and personal care applications, Mater. Sci. Eng. C. 45 (2014) 644–658. doi:10.1016/j.msec.2014.04.050.

[126] G. Falini, S. Albeck, S. Weiner, L. Addadi, Control of aragonite or

calcite polymorphism by mollusk shell macromolecules, Science (80-.). 271 (1996) 67–69. doi:10.1126/science.271.5245.67.

[127] A. Sykes, P. Domingues, M. Correia, J. Andrade, Cuttlefish culture-state of the art and future trends, Vie Milieu/Life Environ. (2006) 129–137.

[128] A. Ospina-Alvarez, S. de Juan, P. Pita, G.B. Ainsworth, F.L. Matos, C. Pita, S. Villasante, A network analysis of global cephalopod trade, Sci. Rep. 12 (2022) 1–14.

[129] Z.A. Doubleday, T.A.A. Prowse, A. Arkhipkin, G.J. Pierce, J. Semmens, M. Steer, S.C. Leporati, S. Lourenço, A. Quetglas, W. Sauer, B.M. Gillanders, Global proliferation of cephalopods, Curr. Biol. 26 (2016) R406–R407. doi:https://doi.org/10.1016/j.cub.2016.04.002.

[130] J. Cadman, S. Zhou, Y. Chen, Q. Li, Cuttlebone: Characterisation, Application and Development of Biomimetic Materials, J. Bionic Eng. 9 (2012) 367–376. doi:10.1016/S1672-6529(11)60132-7.

[131] J.D. Birchall, N.L. Thomas, On the architecture and function of cuttlefish bone, J. Mater. Sci. 18 (1983) 2081–2086. doi:10.1007/BF00555001.

[132] F.A.O., Fishery and Aquaculture Statistics -Aquaculture production, 2018.

[133] D.E. Jacob, A.L. Soldati, R. Wirth, J. Huth, U. Wehrmeister, W. Hofmeister, Nanostructure, composition and mechanisms of bivalve shell growth, Geochim. Cosmochim. Acta. 72 (2008) 5401–5415.

[134] J. Engel, A critical survey of biomineralization: control, mechanisms, functions and material properties, Springer, 2016.

[135] C. Martínez-García, B. González-Fonteboa, F. Martínez-Abella, D. Carro-López, Performance of mussel shell as aggregate in plain

concrete, Constr. Build. Mater. 139 (2017) 570–583.

[136] M. Baláž, E. V. Boldyreva, D. Rybin, S. Pavlović, D. Rodríguez-Padrón, T. Mudrinić, R. Luque, State-of-the-Art of Eggshell Waste in Materials Science: Recent Advances in Catalysis, Pharmaceutical Applications, and Mechanochemistry, Front. Bioeng. Biotechnol. 8 (2021). doi:10.3389/fbioe.2020.612567.

[137] Y. Nys, J. Gautron, J.M. Garcia-Ruiz, M.T. Hincke, Avian eggshell mineralization: biochemical and functional characterization of matrix proteins, Comptes Rendus Palevol. 3 (2004) 549–562. doi:10.1016/J.CRPV.2004.08.002.

[138] T. Hincke, Maxwell, The eggshell: structure, composition and mineralization, Front. Biosci. 17 (2012) 1266. doi:10.2741/3985.

[139] C. Wang, W. Huang, Y. Zhou, L. He, Z. He, Z. Chen, X. He, S. Tian, J. Liao, B. Lu, Y. Wei, M. Wang, 3D printing of bone tissue engineering scaffolds, Bioact. Mater. 5 (2020) 82–91. doi:10.1016/J.BIOACTMAT.2020.01.004.

[140] A.A. Zadpoor, Bone tissue regeneration: The role of scaffold geometry, Biomater. Sci. 3 (2015) 231–245. doi:10.1039/c4bm00291a.

[141] S. Bose, S. Vahabzadeh, A. Bandyopadhyay, Bone tissue engineering using 3D printing, Mater. Today. 16 (2013) 496–504. doi:10.1016/J.MATTOD.2013.11.017.

[142] J. An, J.E.M. Teoh, R. Suntornnond, C.K. Chua, Design and 3D Printing of Scaffolds and Tissues, Engineering. 1 (2015) 261–268. doi:10.15302/J-ENG-2015061.

[143] A.P. Moreno Madrid, S.M. Vrech, M.A. Sanchez, A.P. Rodriguez, Advances in additive manufacturing for bone tissue engineering scaffolds, Mater. Sci. Eng. C. 100 (2019) 631–644.

doi:10.1016/j.msec.2019.03.037.

[144] G. Brunello, S. Sivolella, R. Meneghello, L. Ferroni, C. Gardin, A. Piattelli, B. Zavan, E. Bressan, Powder-based 3D printing for bone tissue engineering, Biotechnol. Adv. 34 (2016) 740–753. doi:10.1016/J.BIOTECHADV.2016.03.009.

[145] D.W. Hutmacher, M. Sittinger, M. V Risbud, Scaffold-based tissue engineering: rationale for computer-aided design and solid free-form fabrication systems, Trends Biotechnol. 22 (2004) 354–362. doi:10.1016/J.TIBTECH.2004.05.005.

[146] A. Zocca, P. Colombo, C.M. Gomes, J. Günster, Additive Manufacturing of Ceramics: Issues, Potentialities, and Opportunities, J. Am. Ceram. Soc. 98 (2015) 1983–2001. doi:10.1111/jace.13700.

[147] Z. Chen, Z. Li, J. Li, C. Liu, C. Lao, Y. Fu, C. Liu, Y. Li, P. Wang, Y. He, 3D printing of ceramics: A review, J. Eur. Ceram. Soc. (2018). doi:10.1016/j.jeurceramsoc.2018.11.013.

[148] R. Trombetta, J.A. Inzana, E.M. Schwarz, S.L. Kates, H.A. Awad, 3D Printing of Calcium Phosphate Ceramics for Bone Tissue Engineering and Drug Delivery, Ann. Biomed. Eng. 45 (2017) 23–44. doi:10.1007/s10439-016-1678-3.

[149] Y. Zhao, Y. Hou, Z. Li, Z. Wang, X. Yan, Powder-Based 3D Printed Porous Structure and Its Application as Bone Scaffold, Front. Mater. 7 (2020) 1–5. doi:10.3389/fmats.2020.00150.

[150] C. Gayer, J. Ritter, M. Bullemer, S. Grom, L. Jauer, W. Meiners, A. Pfister, F. Reinauer, M. Vučak, K. Wissenbach, H. Fischer, R. Poprawe, J.H. Schleifenbaum, Development of a solvent-free polylactide/calcium carbonate composite for selective laser sintering of bone tissue engineering scaffolds, Mater. Sci. Eng. C. 101 (2019)

660–673. doi:https://doi.org/10.1016/j.msec.2019.03.101.

[151] K. Lin, J. Liu, J.M. Wu, Y. Sun, F. Li, Y. Zhou, Y. Shi, Selective laser sintered nano-HA/PDLLA composite microspheres for bone scaffolds applications, Rapid Prototyp. J. 26 (2020) 1131–1143. doi:10.1108/RPJ-06-2019-0155.

[152] L. Cheng, K. Shoma Suresh, H. He, R.S. Rajput, Q. Feng, S. Ramesh, Y. Wang, S. Krishnan, S. Ostrovidov, G. Camci-Unal, M. Ramalingam, 3d printing of micro-and nanoscale bone substitutes: A review on technical and translational perspectives, Int. J. Nanomedicine. 16 (2021) 4289–4319. doi:10.2147/IJN.S311001.

[153] W. Jiang, J. Shi, W. Li, K. Sun, Three dimensional melt-deposition of polycaprolactone/bio-derived hydroxyapatite composite into scaffold for bone repair, J. Biomater. Sci. Polym. Ed. 24 (2013) 539–550. doi:10.1080/09205063.2012.698894.

[154] H.W. Kim, Y.J. Kim, Fabrication of strontium-substituted hydroxyapatite scaffolds using 3D printing for enhanced bone regeneration, J. Mater. Sci. 56 (2021) 1673–1684. doi:10.1007/s10853-020-05391-y.

[155] K. Li, S. Li, F. Ai, J. Yan, K. Zhou, Fabrication and Characterization of Sr-doped Hydroxyapatite Porous Scaffold, Jom. 73 (2021) 1745–1753. doi:10.1007/s11837-021-04684-0.

[156] A.M. Mocioiu, R. Tutuianu, L.M. Cursaru, R.M. Piticescu, P. Stanciu, B.S. Vasile, R. Trusca, V. Sereanu, A. Meghea, 3D structures of hydroxyapatite obtained from Rapana venosa shells using hydrothermal synthesis followed by 3D printing, J. Mater. Sci. 54 (2019) 13901–13913. doi:10.1007/s10853-019-03872-3.

[157] Y. Shi, T. Pan, W. Zhu, C. Yan, Z. Xia, Artificial bone scaffolds of coral

imitation prepared by selective laser sintering, J. Mech. Behav. Biomed. Mater. 104 (2020) 103664. doi:10.1016/j.jmbbm.2020.103664.

[158] F. Cestari, G. Chemello, A. Galotta, V.M. Sglavo, Low-temperature synthesis of nanometric apatite from biogenic sources, Ceram. Int. (2020). doi:https://doi.org/10.1016/j.ceramint.2020.06.123.

[159] M. Bortolotti, L. Lutterotti, G. Pepponi, Combining XRD and XRF analysis in one Rietveld-like fitting, Powder Diffr. 32 (2017) S225–S230. doi:10.1017/S0885715617000276.

[160] S. Graulis, D. Chateigner, R.T. Downs, A.F.T. Yokochi, M. Quirós, L. Lutterotti, E. Manakova, J. Butkus, P. Moeck, A. Le Bail, Crystallography Open Database - An open-access collection of crystal structures, J. Appl. Crystallogr. 42 (2009) 726–729. doi:10.1107/S0021889809016690.

[161] A. Finnemore, P. Cunha, T. Shean, S. Vignolini, S. Guldin, M. Oyen, U. Steiner, Biomimetic layer-by-layer assembly of artificial nacre, Nat. Commun. (2012). doi:10.1038/ncomms1970.

[162] M.R. Snow, A. Pring, P. Self, D. Losic, J. Shapter, The origin of the color of pearls in iridescence from nano-composite structures of the nacre, Am. Mineral. 89 (2004) 1353–1358.

[163] J.J. Lim, Thermogravimetric analysis of human femur bone, J. Biol. Phys. 3 (1975) 111–129. doi:10.1007/BF02308895.

[164] D. Nikolayev, T. Lychagina, A. Pakhnevich, Experimental neutron pole figures of minerals composing the bivalve mollusc shells, SN Appl. Sci. 1 (2019) 1–8. doi:10.1007/s42452-019-0355-1.

[165] F.A. Miller, C.H. Wilkins, Infrared Spectra and Characteristic Frequencies of Inorganic Ions, Anal. Chem. 24 (1952) 1253–1294.

[166] V. Ramasamy, V. Ponnusamy, J. Henialatha, P. Presannalakshmi,

FTlR-characterisation and thermal analysis of natural calcite and aragonite, Indian J. Phys. 77B (2003) 443–450.

[167] M. Cusack, A.C. Fraser, T. Stachel, Magnesium and phosphorus distribution in the avian eggshell, Comp. Biochem. Physiol. Part B Biochem. Mol. Biol. 134 (2003) 63–69. doi:https://doi.org/10.1016/S1096-4959(02)00185-9.

[168] A. Ressler, M. Cvetnić, M. Antunović, I. Marijanović, M. Ivanković, H. Ivanković, Strontium substituted biomimetic calcium phosphate system derived from cuttlefish bone, J. Biomed. Mater. Res. - Part B Appl. Biomater. 108 (2020) 1697–1709. doi:10.1002/jbm.b.34515.

[169] R.. Hewitt, Analysis of aragonite from the cuttlebone of Sepia officinalis L., Mar. Geol. 18 (1975) M1–M5. doi:10.1016/0025-3227(75)90033-X.

[170] L.I. Ardanova, E.I. Get'man, S.N. Loboda, V. V Prisedsky, T. V Tkachenko, V.I. Marchenko, V.P. Antonovich, N.A. Chivireva, K.A. Chebishev, A.S. Lyashenko, Isomorphous Substitutions of Rare Earth Elements for Calcium in Synthetic Hydroxyapatites, Inorg. Chem. 49 (2010) 10687–10693. doi:10.1021/ic1015127.

[171] C.I. Sainz-Díaz, A. Villacampa, F. Otálora, Crystallographic properties of the calcium phosphate mineral, brushite, by means of First Principles calculations, Am. Mineral. 89 (2004) 307–313.

[172] A.A. Khan, J.P. Roux, W.J. James, The crystal structure of diammonium hydrogen phosphate,(NH4) 2HPO4, Acta Crystallogr. Sect. B Struct. Crystallogr. Cryst. Chem. 28 (1972) 2065–2069.

[173] A. Grunenwald, C. Keyser, A.M. Sautereau, E. Crubézy, B. Ludes, C. Drouet, Revisiting carbonate quantification in apatite (bio)minerals: a validated FTIR methodology, J. Archaeol. Sci. 49 (2014) 134–141.

doi:10.1016/J.JAS.2014.05.004.

[174] S.J. Gregg, K.S.W. Sing, Adsorption, surface area and porosity, 2nd ed., London, 1982.

[175] G.J.F. MacDonald, Experimental determination of calcite-aragonite equilibrium relations at elevated temperatures and pressures, Am. Mineral. 41 (1956) 744–756.

[176] L. Müller, E. Conforto, D. Caillard, F.A. Müller, Biomimetic apatite coatings-Carbonate substitution and preferred growth orientation, Biomol. Eng. 24 (2007) 462–466. doi:10.1016/j.bioeng.2007.07.011.

[177] C. Ortali, I. Julien, M. Vandenhende, C. Drouet, E. Champion, Consolidation of bone-like apatite bioceramics by spark plasma sintering of amorphous carbonated calcium phosphate at very low temperature, J. Eur. Ceram. Soc. 38 (2018) 2098–2109. doi:10.1016/J.JEURCERAMSOC.2017.11.051.

[178] I. Rehman, W. Bonfield, Characterization of hydroxyapatite and carbonated apatite by photo acoustic FTIR spectroscopy, J. Mater. Sci. Mater. Med. 8 (1997) 1–4. doi:10.1023/A:1018570213546.

[179] R.N. Panda, M.F. Hsieh, R.J. Chung, T.S. Chin, FTIR, XRD, SEM and solid state NMR investigations of carbonate-containing hydroxyapatite nano-particles synthesized by hydroxide-gel technique, J. Phys. Chem. Solids. 64 (2003) 193–199. doi:10.1016/S0022-3697(02)00257-3.

[180] Z.Z. Zyman, D. V. Rokhmistrov, V.I. Glushko, I.G. Ivanov, Thermal impurity reactions and structural changes in slightly carbonated hydroxyapatite, J. Mater. Sci. Mater. Med. 20 (2009) 1389–1399. doi:10.1007/s10856-009-3706-4.

[181] M. Sadat-Shojai, M.-T. Khorasani, E. Dinpanah-Khoshdargi, A.

Jamshidi, Synthesis methods for nanosized hydroxyapatite with diverse structures, Acta Biomater. 9 (2013) 7591–7621. doi:10.1016/J.ACTBIO.2013.04.012.

[182] F. Cestari, F. Agostinacchio, A. Galotta, G. Chemello, A. Motta, V.M. Sglavo, Nano-hydroxyapatite derived from biogenic and bioinspired calcium carbonates: Synthesis and in vitro bioactivity, Nanomaterials. 11 (2021) 1–14. doi:10.3390/nano11020264.

[183] M. Yashima, A. Sakai, T. Kamiyama, A. Hoshikawa, Crystal structure analysis of β-tricalcium phosphate Ca3(PO4)2 by neutron powder diffraction, J. Solid State Chem. 175 (2003) 272–277. doi:https://doi.org/10.1016/S0022-4596(03)00279-2.

[184] W.R. Busing, H.A. Levy, Neutron Diffraction Study of Calcium Hydroxide, J. Chem. Phys. 26 (1957) 563–568. doi:10.1063/1.1743345.

[185] G. Fiquet, P. Richet, G. Montagnac, High-temperature thermal expansion of lime, periclase, corundum and spinel, Phys. Chem. Miner. 27 (1999) 103–111. doi:10.1007/s002690050246.

[186] A. Bigi, F. Marchetti, A. Ripamonti, N. Roveri, E. Foresti, Magnesium and strontium interaction with carbonate-containing hydroxyapatite in aqueous medium, J. Inorg. Biochem. 15 (1981) 317–327. doi:10.1016/S0162-0134(00)80235-4.

[187] A. Bigi, E. Foresti, M. Gandolfi, M. Gazzano, N. Roveri, Isomorphous substitutions in β-tricalcium phosphate: The different effects of zinc and strontium, J. Inorg. Biochem. 66 (1997) 259–265. doi:10.1016/S0162-0134(96)00219-X.

[188] S. Kannan, S. Pina, J.M.F. Ferreira, Formation of strontium-stabilized β-tricalcium phosphate from calcium-deficient apatite, J. Am. Ceram. Soc. 89 (2006) 3277–3280. doi:10.1111/j.1551-2916.2006.01203.x.

[189] U. Batra, S. Kapoor, S. Sharma, Influence of magnesium ion substitution on structural and thermal behavior of nanodimensional hydroxyapatite, J. Mater. Eng. Perform. 22 (2013) 1798–1806. doi:10.1007/s11665-012-0462-2.

[190] W. Paul, C.P. Sharma, Effect of calcium, zinc and magnesium on the attachment and spreading of osteoblast like cells onto ceramic matrices, J. Mater. Sci. Mater. Med. 18 (2007) 699–703. doi:10.1007/s10856-006-0005-1.

[191] F. Cestari, M. Petretta, Y. Yang, A. Motta, B. Grigolo, V.M. Sglavo, 3D printing of PCL / nano-hydroxyapatite scaffolds derived from biogenic sources for bone tissue engineering, Sustain. Mater. Technol. 29 (2021) e00318. doi:10.1016/j.susmat.2021.e00318.

[192] K. Fukushima, D. Tabuani, G. Camino, Nanocomposites of PLA and PCL based on montmorillonite and sepiolite, Mater. Sci. Eng. C. 29 (2009) 1433–1441. doi:10.1016/j.msec.2008.11.005.

[193] E.C. Chen, T.M. Wu, Isothermal crystallization kinetics and thermal behavior of poly(ε-caprolactone)/multi-walled carbon nanotube composites, Polym. Degrad. Stab. 92 (2007) 1009–1015. doi:10.1016/j.polymdegradstab.2007.02.019.

[194] H. Bittiger, R.H. Marchessault, W.D. Niegisch, Crystal structure of poly-ε-caprolactone, Acta Crystallogr. Sect. B Struct. Crystallogr. Cryst. Chem. 26 (1970) 1923–1927. doi:10.1107/s0567740870005198.

[195] T. Hanemann, Influence of particle properties on the viscosity of polymer-alumina composites, Ceram. Int. 34 (2008) 2099–2105. doi:10.1016/j.ceramint.2007.08.007.

[196] V. Guarino, F. Causa, L. Ambrosio, Porosity and mechanical properties relationship in PCL porous scaffolds, J. Appl. Biomater.

Biomech. 5 (2007) 149–157. doi:10.1177/228080000700500303.

[197] L. Lu, Q. Zhang, D.M. Wootton, R. Chiou, D. Li, B. Lu, P.I. Lelkes, J. Zhou, Mechanical study of polycaprolactone-hydroxyapatite porous scaffolds created by porogen-based solid freeform fabrication method, J. Appl. Biomater. Funct. Mater. 12 (2014) 145–154. doi:10.5301/JABFM.5000163.

[198] F. Cestari, Y. Yang, J. Wilbig, J. Günster, A. Motta, V.M. Sglavo, Powder 3D Printing of Bone Scaffolds with Uniform and Gradient Pore Sizes Using Cuttlebone-Derived Calcium Phosphate and Glass-Ceramic, Materials (Basel). 15 (2022). doi:10.3390/ma15155139.

[199] C. Sun, X. Tian, L. Wang, Y. Liu, C.M. Wirth, J. Günster, D. Li, Z. Jin, Effect of particle size gradation on the performance of glass-ceramic 3D printing process, Ceram. Int. 43 (2017) 578–584. doi:10.1016/j.ceramint.2016.09.197.

[200] H.H. Hausner, Powder Characteristics and their Effect on Powder Processing, Powder Technol. 30 (1981) 3–8.

[201] Y. Ohashi, Polysynthetically-twinned structures of enstatite and wollastonite, Phys. Chem. Miner. 10 (1984) 217–229. doi:10.1007/BF00309314.

[202] J.A. Speer, G. V Gibbs, The crystal structure of synthetic titanite, CaTiOSiO4, and the domain textures of natural titanites, Am. Mineral. 61 (1976) 238–247.

[203] R.W.G. Wyckoff, IX. Die Kristallstruktur von β-Cristobalit SiO2 (bei hohen Temperaturen stabile Form), Zeitschrift Für Krist. Mater. 62 (1925) 189–200.

[204] R.M. Thompson, R.T. Downs, The crystal structure of diopside at pressure to 10 GPa, Am. Mineral. 93 (2008) 177–186.

[205] L. Obadia, M. Julien, S. Quillard, T. Rouillon, P. Pilet, J. Guicheux, B. Bujoli, J.M. Bouler, Na-doped β-tricalcium phosphate: Physico-chemical and in vitro biological properties, J. Mater. Sci. Mater. Med. 22 (2011) 593–600. doi:10.1007/s10856-010-4219-x.

[206] D.P. Mukherjee, S.K. Das, SiO2-Al2O3-CaO glass-ceramics: Effects of CaF2 on crystallization, microstructure and properties, Ceram. Int. 39 (2013) 571–578. doi:10.1016/j.ceramint.2012.06.066.

[207] R.A. Nyquist, R.O. Kagel, Infrared Spectra of Inorganic Compounds, in: Handb. Infrared Raman Spectra Inorg. Compd. Org. Salts, Academic Press, 1971: pp. 1–18. doi:10.1016/b978-0-12-523450-4.50005-5.

[208] S. Agathopoulos, D.U. Tulyaganov, J.M.G. Ventura, S. Kannan, A. Saranti, M.A. Karakassides, J.M.F. Ferreira, Structural analysis and devitrification of glasses based on the CaO-MgO-SiO2 system with B2O3, Na2O, CaF2 and P2O5 additives, J. Non. Cryst. Solids. 352 (2006) 322–328. doi:10.1016/j.jnoncrysol.2005.12.003.

[209] R. Rojaee, M. Fathi, K. Raeissi, Electrophoretic deposition of nanostructured hydroxyapatite coating on AZ91 magnesium alloy implants with different surface treatments, Appl. Surf. Sci. 285 (2013) 664–673. doi:10.1016/j.apsusc.2013.08.108.

[210] T. Kokubo, M. Shigematsu, Y. Nagashima, M. Tashiro, T. Nakamura, T. Yamamuro, S. Higashi, Apatite-and wollastonite-containg glass-ceramics for prosthetic application, Bull. Inst. Chem. Res. Kyoto Univ. 60 (1982) 260–268.

[211] S.R. Caliari, B.A.C. Harley, Structural and biochemical modification of a collagen scaffold to selectively enhance MSC tenogenic, chondrogenic, and osteogenic differentiation, Adv. Healthc. Mater. 3

(2014) 1086–1096. doi:10.1002/adhm.201300646.